

Faculty of Natural Science
Physics Department
Ben Gurion University of the Negev

**Transitions between atomic quantum
levels in room temperature ^{87}Rb vapor**

*Thesis submitted in partial fulfillment of the requirements for the
Master of Science degree*

Orr Be'er

Under the supervision of

Prof. Ron Folman

September 13, 2016

Acknowledgements

I would like to use this opportunity to express my gratitude to everyone who supported me throughout this work.

I would first like to thank my thesis advisor Prof. Ron Folman. It is a great privilege to be part of the Atom Chip group. I am very thankful to Dr. David Grosswaser. David, thank you for being available at any time and for any questions and problems I had along the way. I can't exaggerate the amount of time and patience that Dr. Menachem Givon has dedicated to my project. Meny, thank you for that. Many thanks also to Dr. Yoni Japha for your insightful comments about the theory and for building a mathematical model these were a great help.

Special thanks to Dr. Guobin Liu who worked with me on the experiment and helped to verify my results. I wish also to thank Yaniv Bar-Haim for helping me build the vapor-cell filling system and for hosting me when needed during my brief return visits to Israel for writing this thesis. You have always been so reliable as a good friend.

I also want to thank the former vapor team members, Yair Margalit and Dr. Amir Waxman, for support, teaching, and advice during my work. Dr. Mark Keil, Dr. Judy Kupferman and Dr. Daniel Rohrllich, thank you all so much for the infinite time you dedicated to editing this work.

I want to thank my dear family Itzhak, Rivka Bat-el and Amir Beer, Naama Knafo, and Yotam Yaakuba for your support along the way. And finally I wish to thank my dear spouse Shlomit Edri, Im lucky to have you around.

This accomplishment would not have been possible without all of you.

Thank you,

Abstract

Rabi oscillations are a coherent phenomenon of a two-level system separated by $\hbar\omega_0$ and a near-resonance coupling field. It is typically characterized by the Rabi oscillations' frequency and amplitude. The Rabi frequency is proportional to the amplitude of the coupling field and it increases with the detuning of this field from resonance. The oscillation amplitude decreases with the detuning. In this work I describe Rabi oscillations between Zeeman sub-levels of a single hyperfine ground state of ^{87}Rb atoms contained in a vapor cell with a buffer gas. These Rabi oscillations are coherent; the oscillation frequency is proportional to the coupling field amplitude, and the oscillation amplitude, as expected, decreases as the detuning of the coupling field from resonance increases. However, contrary to the theoretical expectation as noted above, the oscillation frequency does not increase with the detuning, and is totally independent of it. This phenomenon is termed by us Rabi "freeze." Even when the detuning is so large that the oscillations are barely noticeable, the oscillation frequency does not change.

I describe detailed studies of the Rabi "freeze" phenomenon with different buffer gases including neon at a pressure of 7.5 Torr, krypton at 60 Torr and neon at 75 Torr, and with two different methods of recording the Rabi oscillations. I perform both $5^2\text{S}_{1/2}|F=2, m_F=2\rangle \leftrightarrow 5^2\text{S}_{1/2}|F=2, m_F=1\rangle$ and $5^2\text{S}_{1/2}|F=2, m_F=-2\rangle \leftrightarrow 5^2\text{S}_{1/2}|F=2, m_F=-1\rangle$ oscillations using a ~ 18 MHz coupling field where the ^{87}Rb atoms are subjected to a DC magnetic field of ~ 26 G. In all of these cases, the Rabi oscillation frequency is completely independent of the detuning.

I compare my results to Rabi oscillations between Zeeman sub-levels residing in different hyperfine ground states, such as $5^2\text{S}_{1/2}|F=1, m_F=0\rangle \leftrightarrow 5^2\text{S}_{1/2}|F=2, m_F=0\rangle$, induced by a ~ 6.8 GHz coupling field where the ^{87}Rb atoms are subjected to a DC magnetic field of ~ 0.05 G, or $5^2\text{S}_{1/2}|F=1, m_F=-1\rangle \leftrightarrow 5^2\text{S}_{1/2}|F=2, m_F=1\rangle$ oscillations induced by two coherent fields at ~ 6.8 GHz and ~ 2 MHz with a DC magnetic field of 3.23 G. These oscillations were induced in earlier experiments in the same ^{87}Rb vapor cells used for my study of the Rabi "freeze." In all of the Rabi oscillations recorded with the coupling radiation in the range of 6.8 GHz, the Rabi oscillation frequency increases with the detuning as expected. Additional recording of Rabi oscillations was performed with a ~ 18 MHz radiation coupling of the $5^2\text{S}_{1/2}|F=2, m_F=2\rangle \leftrightarrow 5^2\text{S}_{1/2}|F=2, m_F=1\rangle$ transition of a free-falling, ultracold ^{87}Rb cloud, subjected to a DC magnetic field of ~ 26 G. Here, too there was no "freeze": the oscillation frequency increases with the detuning. It is important to note that these last recordings were done under similar conditions to those of the recordings that show Rabi "freeze," except that no buffer gas is present with the ultracold ^{87}Rb cloud.

Based on the data presented in this work we present two hypotheses: The first is that what we are observing is an artifact induced by the sensitivity of our two-level system to residual magnetic fields. Other systems noted above had no first order Zeeman (differential) sensitivity. Specifically, we present a model in which a small magnetic gradient across the vapor cell exists so that the detuning of the coupling field causes the field to simply address a different atom population inside the cell. The second hypothesis we examine is that the collisions of the ^{87}Rb atoms with the buffer gas atoms may be the cause for the Rabi "freeze." Here, one may speculate that the fact that we have not seen this phenomenon in previous experiments with the same vapor cells has to do with the fact that the other two-level systems had the same $|m_F|$ for both states and the collisions may be dependent in some way on $|m_F|$.

One may also speculate that the fact that the transition frequency in previous cases was higher than the collision rate, is somehow relevant (the collision rate is 50 M to 500 M per second). These collisions may then shift the atomic levels or effectively turn the buffer gas into an entangled environment, thus altering the simple two-level system theory.

I wish to clarify that at this point I am not able to provide any reasonable theoretical explanation for this Rabi “freeze.” As we describe in detail, the first hypothesis suffers from several difficulties when compared to the experimental parameters and data. The second hypothesis suffers from a fundamental lack of a known physical mechanism. Due to the limited time frame of an M.Sc. project, further investigation of this phenomenon we observed is beyond the scope of this thesis, and in the outlook, I suggest several possible ways to further examine these hypotheses.

As I write this thesis, my colleagues are working on both the experimental and the theoretical routes. In fact, we would appreciate it if the details of this thesis would not be widely distributed until we have a chance to verify our findings, make available a sound explanation, and publish the results in an appropriate manner.

Contents

1	Introduction	1
2	Theoretical Background	3
2.1	Rabi oscillations in a two-level system	3
2.2	The density matrix for a two-level system	5
2.3	The Bloch sphere	7
2.4	The ^{87}Rb atom	8
3	Experimental background	11
3.1	Relaxation processes	11
3.2	Optical pumping	12
3.3	Absorption of light by a rubidium vapor cell	13
4	Experiment	15
4.1	The experimental system	15
4.1.1	External cavity diode laser	15
4.1.2	Laser frequency lock	17
4.1.3	Double-pass acousto-optical modulator	18
4.1.4	Applying external fields on the vapor cell	19
4.1.5	Vapor cell measurement setup	21
4.1.6	The computer-experimental setup interface	22
4.2	Methods	23
4.2.1	Inducing radio frequency Rabi oscillations between $ 2, -2\rangle \leftrightarrow 2, -1\rangle$ Zeeman sub-levels	23
4.2.2	Hyperfine state population measurements	24
4.3	Inducing Rabi oscillations	25
4.4	Two types of Rabi measurements	27
4.4.1	Rabi “in-the-dark” measurement	28
4.4.2	Rabi “on-the-fly” measurement	29
4.4.3	Comparison between Rabi “in-the-dark” and Rabi “on-the- fly”	30
5	Results: observing the Rabi “freeze”	31
5.1	Fitting method	31
5.2	Results for vapor cell with a 75 Torr neon buffer gas	32
5.3	Results for vapor cell with a 7.5 Torr neon buffer gas	36
5.4	Results for vapor cell with a 60 Torr krypton buffer gas	40
5.5	Rabi oscillations utilizing the $ 2, 2\rangle \leftrightarrow 2, 1\rangle$ transition	42
5.6	Dependence of the Rabi frequency on the coupling field amplitude	43
6	Discussion	45
6.1	The influence of a small magnetic inhomogeneity on Rabi oscillations	45
6.2	A possible influence of collisions on the Rabi oscillations	48
7	Summary and outlook	50
Appendix A Rabi oscillations in ^{87}Rb vapor cells induced by a 6.8 GHz coupling field		53
Appendix B Rabi oscillations in the $2, 2\rangle \leftrightarrow 2, 1\rangle$ transition in ultra-cold atoms		56

Appendix C Manufacturing the rubidium vapor cells	58
Appendix D The Rabi oscillations fit parameters	61

List of Figures

2.1	Rabi oscillations	5
2.2	Coherent state transitions in two-level systems on the Bloch sphere	8
2.3	^{87}Rb level structure	9
3.1	Population decaying from the hyperfine states to equilibrium	11
3.2	Optical pumping	13
3.3	Absorption of laser beam that passes through a vapor cell	14
4.1	External cavity diode laser in the Littrow configuration	16
4.2	Polarization lock scheme	17
4.3	double pass Acousto-optic modulator scheme	19
4.4	z direction magnetic field coils apparatus	20
4.5	RF generator scheme	21
4.6	Rabi oscillations measurement setup scheme	22
4.7	Absorption profile of a near $ 2, -2\rangle \leftrightarrow 2, -1\rangle$ resonance RF scan	26
4.8	Rabi “in-the-dark” measurement	28
4.9	Rabi “on-the-fly” measurement	30
5.1	Measured Rabi oscillations “in-the-dark” in vapor cell with a 75 Torr Ne buffer gas	32
5.2	FFT of Rabi “in-the-dark” measurements	33
5.3	Rabi amplitude and generalized Rabi frequency	34
5.4	Rabi oscillations “on-the-fly” measurements in vapor cell with a 75 Torr Ne buffer gas	35
5.5	FFT of Rabi “on-the-fly” measurements	35
5.6	Rabi amplitude and generalized Rabi frequency frequency	36
5.7	Rabi “in-the-dark” measurements in vapor cell with a 7.5 Torr Ne buffer gas	37
5.8	FFT of Rabi “in-the-dark” measurements	37
5.9	Rabi amplitude and generalized Rabi frequency	38
5.10	Rabi “on-the-fly” measurement in vapor cell with a 7.5 Torr n buffer gas	39
5.11	FFT of Rabi “on-the-fly” measurement	39
5.12	Rabi amplitude and generalized Rabi frequency	40
5.13	Rabi “on-the-fly” measurements in vapor cell with a 60 Torr Kr buffer gas	41
5.14	FFT of Rabi “on-the-fly” measurements	41
5.15	Rabi amplitude and generalized Rabi frequency of the $ 2, 2\rangle \leftrightarrow 2, 1\rangle$ transition	42
5.16	Rabi oscillation with different RF amplitudes	43
6.1	Simple simulation of the Rabi “freeze”	47
A.1	Rabi oscillation with MW field	53
A.2	Two-photon transition diagram	54
A.3	Generalized Rabi frequency mapping for two-photon transition	55
B.1	BEC Rabi oscillations	56
B.2	BEC Rabi oscillations	57
C.1	Vapor-cell filling system	58
C.2	Paraffin evaporation method	59

List of Tables

3.1	Vapor cells list	12
4.1	A summary of the lasers we use in our setup	27
D.1	Rabi “on-the-fly” Ne 75 Torr fit parameters	61
D.2	Rabi “on-the-fly” Ne 75 Torr fit parameters	62

1 Introduction

Quantum phenomena in atomic vapor were extensively studied from the early 1950's. Optical pumping, a technique to optically induce order in an ensemble of atoms, developed by the 1966 Nobel Prize winner Alfred Kastler in 1950 [1], was an important step towards the research of quantum optics in vapor. Features of vapor were then studied, such as thermal relaxation of atomic states in the presence of buffer gas and in wall-coated cells [2, 3]. In addition, research on exploitation of atomic transition in vapor for magnetic sensing [4, 5], high precision frequency standards [6] and atomic clocks was initiated [7].

Early studies of atom-light interaction in vapor cells were typically conducted with alkali lamps. These light sources were Doppler broadened and not tunable. The introduction of the tunable solid state laser diode (first introduced by R. N. Hall in 1962 [8] and commercialized in the late 1980's) created a new interest in light-vapor interaction. In recent years alkali vapor cells played a role in a wide range of studies, such as: the effect of wall coating and buffer gas vapor cell on the relaxation time [9, 10]; demonstration of fundamental quantum mechanical features, such as macroscopic entanglement in cesium vapor cell [11]; high precision magnetometry with alkali metal vapor cells [12, 13]; nonlinear optic phenomena such as four-wave mixing [14] and slow and stopped light [15, 16]; collective phenomenon such as phase transition has been observed [17]; miniature vapor cells have been fabricated and used for demonstrating miniature magnetometers [18] and miniature atomic clocks [19].

Rabi oscillations, which were first formulated by the 1944 Noble Prize winner I.I. Rabi in 1937 [20], are a fundamental phenomenon of quantum mechanics. This is the periodical transition of the population of a two-level quantum system between its stationary states in the presence of an oscillatory driving field. Rabi oscillations are a well-known, well studied phenomenon and have a wide range of applications from magnetic resonance imaging to research for quantum computing. The concept of Rabi oscillations serves research of many topics in physics such as: super-conductor Josephson junctions [21, 22]; semi-conductor quantum dots and quantum wells [23, 24]; nitrogen vacancy centers in diamonds [25]; cold atoms and alkali vapor [26, 27].

The frequency of Rabi oscillations is known to depend on the detuning of the driving field from the frequency of the inter-level transition. However, in this work we describe the observation of a two-level system driven by an external oscillating field for which the Rabi oscillations' frequency is *independent* of the detuning. We demonstrate this phenomenon in a ^{87}Rb vapor cell with a buffer gas, between the $|2, -2\rangle \leftrightarrow |2, -1\rangle$ and the $|2, 2\rangle \leftrightarrow |2, 1\rangle$ Zeeman sub-levels. We named this phenomenon Rabi "freeze." The Rabi oscillation frequency is known to also be proportional to the amplitude of the electromagnetic field, and indeed in our system the dependence of the oscillation frequency on the amplitude of the electromagnetic field is as theoretically expected.

We measured Rabi oscillations for a wide range of detuning values in three different buffer gas cells. We compare our experimental results with previous experimental measurements with the same vapor cells but with different two-level systems, where Rabi "freeze" does not occur. We also measured Rabi oscillations in the same two-level system in a cloud of free falling cold ^{87}Rb atoms. No Rabi "freeze" was observed.

The theory describing the interaction of a two-level system in a ^{87}Rb atom with an oscillating electromagnetic field is derived in Ch. 2. Fundamental processes and their role in our system are discussed in Ch. 3. Details of the experimental system are described in Sec. 4.1. The methods we used to execute the experiments are detailed

in Sec. 4.2. The two different procedures used to detect the Rabi oscillations are described and compared in Sec. 4.3. The results of our measurements are presented and analyzed in Ch. 5. Chapter 6 presents two hypotheses which may explain the observed Rabi “freeze”. The first assumes an experimental artifact due to residual magnetic gradients in the cell, and the second speculates that collisions with the buffer gas play some role in modifying the simple two-level theory. Unfortunately, by the time this thesis was written, we have still not been able to substantiate any of these hypotheses. In Ch. 6 we also present for comparison previous work done on these cells but on other two-level systems. A summary of this work and an outlook, including suggestions for future experiments, are given in Ch. 7.

2 Theoretical Background

In this chapter we provide the theoretical background needed for this work and establish the notation we use throughout the thesis. Section 2.1 describes Rabi population oscillations in a two-level system; Sec. 2.2 and 2.3 introduce the density matrix and the Bloch sphere for two-level systems. In Sec. 2.4 we review the properties of the atom we use in our experimental work: the ^{87}Rb atom. The Rabi oscillations formula is derived following M.O. Scully's book [28], the density matrix for a two-level system follows Sakurai's book [29] and D. Cohen's lecture notes [30], and the rubidium atom properties are adapted from Steck's compilation [31].

2.1 Rabi oscillations in a two-level system

Rabi oscillations are coherent population oscillations between two different quantum energy states driven by an external periodic field. Following M.O. Scully's book [28], we investigate the atom-light interaction of a two-level atom interacting with a classical electromagnetic field. We denote the two states $|0\rangle$ and $|1\rangle$, with energies E_0 and E_1 , respectively. The transition frequency between these two states is $\omega_0 = (E_1 - E_0)/\hbar$. We limit our discussion to the case where ω_0 is sufficiently far from any other transition of the atom so that it couples only the $|0\rangle$ and $|1\rangle$ states. The Hamiltonian of the atom and a coupling field at a near-resonant frequency $\omega \sim \omega_0$ is:

$$H = H_0 + V, \quad [2.1.1]$$

where H_0 is the Hamiltonian of a two-level atom such that $H_0|0\rangle = E_0|0\rangle$ and $H_0|1\rangle = E_1|1\rangle$. The potential energy of the atom in the electromagnetic field (in the dipole approximation) is:

$$V = -\mathbf{d} \cdot \mathbf{E} \cos(\omega t), \quad [2.1.2]$$

where $\mathbf{d} = -e\mathbf{r}$ is the dipole moment in the direction \mathbf{r} and \mathbf{E} is the amplitude of the coupling field. We can write the state vector of the system as:

$$|\psi(t)\rangle = c_0(t)e^{-iE_0t/\hbar}|0\rangle + c_1(t)e^{-iE_1t/\hbar}|1\rangle. \quad [2.1.3]$$

From the Schrödinger equation

$$i\hbar \frac{\partial |\psi(t)\rangle}{\partial t} = H|\psi(t)\rangle, \quad [2.1.4]$$

we arrive at the coupled set of equations for the amplitudes c_0 and c_1 :

$$\begin{aligned} \dot{c}_0 &= \frac{i\mathbf{d} \cdot \mathbf{E}}{2\hbar} [e^{i(\omega - \omega_0)t} + e^{-i(\omega + \omega_0)t}] c_1 \\ \dot{c}_1 &= \frac{i\mathbf{d} \cdot \mathbf{E}}{2\hbar} [e^{i(\omega + \omega_0)t} + e^{-i(\omega - \omega_0)t}] c_0, \end{aligned} \quad [2.1.5]$$

where $\mathbf{d} \cdot \mathbf{E}$ is taken to be real. To solve Eq. 2.1.5 we use the rotating wave approximation. We assume that the frequency $\omega + \omega_0$ is much higher than the rate of any change in the system, so that we can replace the terms $e^{\pm i(\omega + \omega_0)t}$ with their average value over many cycles, which is zero. Applying this approximation we get:

$$\begin{aligned} \dot{c}_0 &= \frac{i\mathbf{d} \cdot \mathbf{E}}{2\hbar} \exp[i(\omega - \omega_0)t] c_1 \\ \dot{c}_1 &= \frac{i\mathbf{d} \cdot \mathbf{E}}{2\hbar} \exp[-i(\omega - \omega_0)t] c_0. \end{aligned} \quad [2.1.6]$$

Let us define the Rabi frequency:

$$\Omega_R = \left| \frac{\mathbf{d} \cdot \mathbf{E}}{\hbar} \right|, \quad [2.1.7]$$

and the detuning of the coupling frequency from the transition frequency:

$$\delta = \omega_0 - \omega. \quad [2.1.8]$$

Equation 2.1.6 is now:

$$\begin{aligned} \dot{c}_0 &= \frac{i\Omega_R}{2} e^{-i\delta t} c_1 \\ \dot{c}_1 &= \frac{i\Omega_R}{2} e^{i\delta t} c_0. \end{aligned} \quad [2.1.9]$$

Taking the time derivative of $\dot{c}_1(t)$ and expressing $\dot{c}_0(t)$ in the terms of $c_1(t)$ we get:

$$\ddot{c}_1 + i\delta\dot{c}_1 + \frac{\Omega_R^2}{4} c_1 = 0. \quad [2.1.10]$$

As a trial solution we set

$$c_1(t) = e^{irt}, \quad [2.1.11]$$

which leads to the two roots:

$$r_{\pm} = \frac{1}{2} \left(\delta \pm \sqrt{\delta^2 + \Omega_R^2} \right). \quad [2.1.12]$$

Thus the general solution is of the form

$$c_1(t) = A_+ e^{ir_+t} + A_- e^{ir_-t}. \quad [2.1.13]$$

For the initial conditions $c_0(0) = 1$ and $c_1(0) = 0$, the solution for $c_1(t)$ is:

$$c_1(t) = i(\Omega_R/\tilde{\Omega}) e^{-i\delta t/2} \sin(\tilde{\Omega} \cdot t/2), \quad [2.1.14]$$

where we define the generalized Rabi frequency:

$$\tilde{\Omega} = \sqrt{\Omega_R^2 + \delta^2}. \quad [2.1.15]$$

The probability of finding the system in the $|1\rangle$ state is therefore:

$$p_1(t) = \frac{1}{2} \frac{\Omega_R^2}{\Omega_R^2 + \delta^2} \left[1 - \cos(\tilde{\Omega} \cdot t) \right] = A_R \left[1 - \cos(\tilde{\Omega} \cdot t) \right], \quad [2.1.16]$$

which is the Rabi formula [20] that was originally derived for a magnetic moment $J = \frac{1}{2}$ rotating in a magnetic field and A_R is the Rabi amplitude. This derivation can easily be adapted to our system.

The quantity $\tilde{\Omega} \cdot t$ is typically referred to as the ‘‘pulse area’’. For the case of resonance ($\delta = 0$) we can define a π pulse, which is a pulse whose area is equal to π . A π pulse drives the population that was prepared, for example, in the state $|\psi\rangle = |0\rangle$ to $|\psi\rangle = |1\rangle$ and vice versa. A $\pi/2$ pulse drives the population that was prepared in the state $|\psi\rangle = |0\rangle$ to a coherent superposition state $|\psi\rangle = \frac{1}{\sqrt{2}}(|0\rangle + |1\rangle)$.

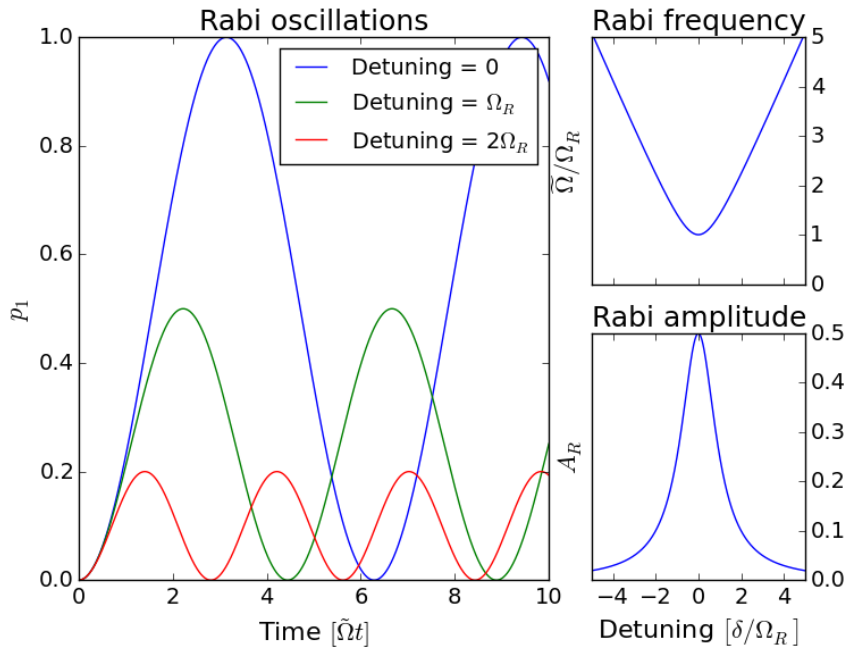


Figure 2.1: Rabi oscillations. (a) Plot of P_1 probability oscillations for different detuning values (see Eq. 2.1.16). The time (horizontal) axis is expressed in dimensionless units of pulse area, while the population (vertical) axis is the probability of finding a two-level atom in the state $|1\rangle$. At zero detuning the population oscillates synchronously between the two states and therefore state $|1\rangle$ is fully occupied after half a period (a π pulse). As the detuning increases the probability for each atom of the ensemble to change its state decreases and the frequency of the population oscillations increases. (b) The dependence of the generalized Rabi frequency on the detuning (see Eq. 2.1.15). (c) The dependence of the Rabi amplitude on the detuning (see Eq. 2.1.16).

In this section we describe Rabi population oscillations, where the dominant term in the interaction of the coupling field with the atom is the electric dipole. In cases where the dominant interaction term is the magnetic dipole, we get similar results by replacing $\mathbf{d} \cdot \mathbf{E}$ with $\boldsymbol{\mu} \cdot \mathbf{B}$.

2.2 The density matrix for a two-level system

The oscillations between two states that were discussed in Sec. 2.1 describe the interaction between light and a single atom. To observe such behavior one needs to measure the statistical properties of such a system, *i.e.*, an ensemble of two-level atoms must be measured. A fundamental tool for dealing with ensembles of quantum systems is the density matrix.

The density operator, pioneered by J. von Neumann in 1927, describes a general (mixed and pure states) ensemble, which characterizes most physical states. The density operator is defined by [29]:

$$\rho = \sum_i W_i |\alpha^{(i)}\rangle \langle \alpha^{(i)}|, \quad [2.2.1]$$

where $|\alpha^{(i)}\rangle$ is a complete set of wave-functions and W_i is the relative weight of each of the wave-functions in the ensemble. The normalization condition of the weights is $\sum_i W_i = 1$. Suppose that we want to measure the expectation value of some

observable A in a mixed ensemble. The expectation value of such a measurement is:

$$\langle A \rangle = \sum_i W_i \langle \alpha^{(i)} | A | \alpha^{(i)} \rangle. \quad [2.2.2]$$

By inserting a unity operator $\sum_{b'} |b'\rangle\langle b'|$ in some arbitrary basis $\{b'\}$ to the left of the operator A and another unity operator $\sum_{b''} |b''\rangle\langle b''|$ in some other arbitrary basis $\{b''\}$ to the right of the operator A , we obtain the expression for the expectation value of A represented in the basis $\{b\}$

$$\langle A \rangle = \sum_i W_i \sum_{b'} \sum_{b''} \langle \alpha^{(i)} | b' \rangle \langle b' | A | b'' \rangle \langle b'' | \alpha^{(i)} \rangle. \quad [2.2.3]$$

Re-arranging the terms in Eq. 2.2.3 we get:

$$\langle A \rangle = \sum_{b'} \sum_{b''} \langle b'' | \left[\sum_i W_i | \alpha^{(i)} \rangle \langle \alpha^{(i)} | \right] | b' \rangle \langle b' | A | b'' \rangle. \quad [2.2.4]$$

The term in the square brackets is the density operator ρ , so that:

$$\langle A \rangle = \sum_{b'} \sum_{b''} \langle b'' | \rho | b' \rangle \langle b' | A | b'' \rangle = \text{Tr}(\rho A). \quad [2.2.5]$$

In order to find the time dependence we shall consider the density operator at some arbitrary time $t = 0$ as:

$$\rho(0) = \sum_i W_i | \alpha^{(i)}(0) \rangle \langle \alpha^{(i)}(0) |. \quad [2.2.6]$$

If we let the density operator evolve without perturbation, the fractional population W_i will not change. The time dependence of the density operator is governed solely by the time evolution of $| \alpha^{(i)} \rangle$, which satisfies the Schrödinger Eq. 2.1.4

$$i\hbar \frac{\partial \rho}{\partial t} = \sum_i W_i [H | \alpha^{(i)}(t) \rangle \langle \alpha^{(i)}(t) | - | \alpha^{(i)}(t) \rangle \langle \alpha^{(i)}(t) | H], \quad [2.2.7]$$

which leads to the density operator equation of motion, the Liouville - von Neumann equation

$$i\hbar \frac{\partial \rho}{\partial t} = -[\rho, H]. \quad [2.2.8]$$

For a two-level system the density operator has the matrix form

$$\rho = \begin{pmatrix} \rho_{00} & \rho_{01} \\ \rho_{10} & \rho_{11} \end{pmatrix}. \quad [2.2.9]$$

Each of the diagonal matrix elements represents the population for each state, and fulfills the normalization condition $\rho_{00} + \rho_{11} = 1$. The off-diagonal matrix elements represent the coherence between the two states, where in this case $\rho_{01} = \rho_{10}^*$.

A diagonal form of the density matrix

$$\rho = \begin{pmatrix} p_0 & 0 \\ 0 & p_1 \end{pmatrix} \quad [2.2.10]$$

can be either a mixture of $|0\rangle$ and $|1\rangle$ with the weights p_0 and p_1 or a pure state when either p_0 or p_1 equals 0 and the other one equals 1. Another example of a pure state is:

$$\rho = \begin{pmatrix} 1/2 & i/2 \\ -i/2 & 1/2 \end{pmatrix}, \quad [2.2.11]$$

which represents a case of an equally distributed superposition of the two basis states. In general if $\text{Tr}(\rho^2) = 1$ then ρ is a density matrix of a pure state. Otherwise, ρ is a density matrix of a mixed state.

2.3 The Bloch sphere

As mentioned in Sec. 2.1, the normalized two-level system state can be described fully by Eq. 2.1.3, $|\psi(t)\rangle = c_0(t)|0\rangle + c_1(t)|1\rangle$, where $|c_0|^2 + |c_1|^2 = 1$. Since c_0 and c_1 are complex numbers and if we can ignore the global phase, Eq. 2.1.3 can be represented in the complex plane as:

$$|\psi\rangle = \cos \frac{\theta}{2} |0\rangle + e^{i\phi} \sin \frac{\theta}{2} |1\rangle, \quad [2.3.1]$$

where

$$\begin{aligned} c_0 &= \cos \frac{\theta}{2} \\ c_1 &= e^{i\phi} \sin \frac{\theta}{2}. \end{aligned} \quad [2.3.2]$$

This representation was originally developed by Felix Bloch [32] as a model for the precession of the nuclear magnetic moment induced by an RF field in a constant magnetic field, and was adopted as a geometrical representation of the Schrödinger equation of a perturbed two-level system by Feynman, Vernon and Hellwarth [33]. The latter equation represents a unit vector on a sphere and is denoted as the Bloch vector, that can be described as a unit vector by Cartesian coordinates

$$\mathbf{v}^{\mathbf{B}} = (v_x^B, v_y^B, v_z^B), \quad [2.3.3]$$

when $|\mathbf{v}^{\mathbf{B}}| = 1$, or in spherical coordinates

$$\begin{aligned} v_x^B &= \sin\theta \cos\phi \\ v_y^B &= \sin\theta \sin\phi \\ v_z^B &= \cos\theta. \end{aligned} \quad [2.3.4]$$

From Eq. 2.3.1 and Eq. 2.3.4 we obtain the relation between Bloch vector components and the probability amplitudes of the two-state wave-function

$$\begin{aligned} v_x^B &= 2 \cdot \Re[c_0 \cdot c_1] \\ v_y^B &= 2 \cdot \Im[c_0 \cdot c_1] \\ v_z^B &= |c_0|^2 - |c_1|^2. \end{aligned} \quad [2.3.5]$$

The south (bottom) and the north (top) poles of the Bloch sphere represent $|1\rangle$ and $|0\rangle$ states respectively. The ground state of the two states $|\psi\rangle = |0\rangle$ corresponds to $(0, 0, 1)$ in Cartesian coordinates with $\theta = 0$. In the same sense, the excited state $|\psi\rangle = |1\rangle$ corresponds to $(0, 0, -1)$ with $\theta = \pi$. The density operator can be represented by the Bloch vector and the Pauli matrices as follows [30]:

$$\rho = \frac{1}{2}(I + \mathbf{v}^{\mathbf{B}} \cdot \hat{\sigma}), \quad [2.3.6]$$

where I is the unit matrix and $\hat{\sigma}$ is the vector of the Pauli matrices $(\sigma_1, \sigma_2, \sigma_3)$. In order to examine the dynamics of such a system we use the Liouville Eq. 2.2.8 to get

$$i\hbar \frac{\partial}{\partial t} \mathbf{v}^{\mathbf{B}} = \frac{1}{2} \text{Tr}[\hat{\sigma}[H, (I + \mathbf{v}^{\mathbf{B}} \cdot \hat{\sigma})]]. \quad [2.3.7]$$

So far the Bloch representation was applied to pure states where the magnitude of the Bloch vector $|\mathbf{v}^{\mathbf{B}}|$ is conserved. We can adapt the Bloch picture to a

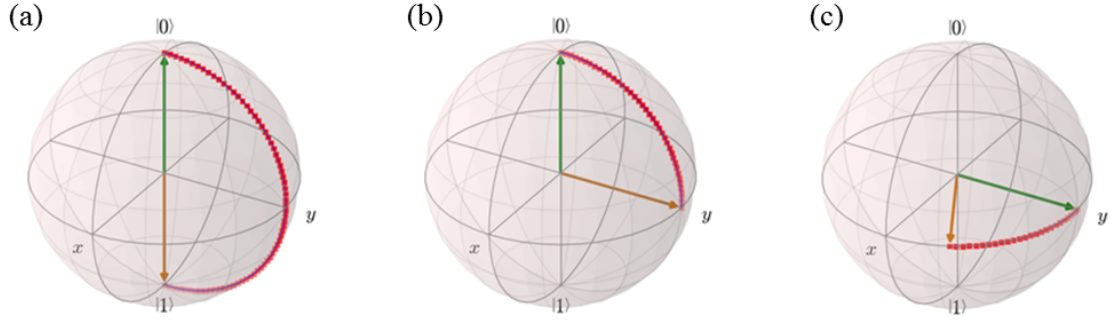


Figure 2.2: Coherent state transitions in two-level systems on the Bloch sphere. The green arrows represent the initial states, the orange arrows represent the final states and the red dots represent the trajectories. (a) π pulse applied to the $|0\rangle$ state; the final state is $|1\rangle$. (b) $\pi/2$ pulse applied to the $|0\rangle$ state; the final state is a coherent superposition of the two states $|0\rangle$ and $|1\rangle$ with zero relative phase between them. (c) Free propagation in time for the superposition of the two states $|0\rangle$ and $|1\rangle$; the two states accumulate a relative phase ϕ (in the x - y plane) as the system evolves.

simple dissipative model by adding time decaying constants for the Bloch vector components

$$\begin{aligned}
 v_x^B(t) &= v_x^B(0)e^{-\frac{t}{T_2}} \\
 v_y^B(t) &= v_y^B(0)e^{-\frac{t}{T_2}} \\
 v_z^B(t) &= [v_z^B(0) - v_z^0]e^{-\frac{t}{T_1}} + v_z^0.
 \end{aligned}
 \tag{2.3.8}$$

Starting at $t = 0$ the Bloch vector touches a point on the surface of the sphere representing a pure state. During time propagation the projection of the Bloch vector on the x - y plane shrinks with the time constant T_2 , which we call the longitudinal decay time and which represents dephasing processes. The z component of the Bloch vector decays toward the value v_z^0 with the time constant T_1 , which we call the transverse decay time and which represents thermal and spontaneous emission processes.

From this model of a two-level atom we can describe the conditions that enable measuring of the relative population of the two states, thereby leading to the observation of Rabi oscillations.

- We need an ensemble. Such an ensemble can be realized using atomic vapor in a vacuum cell, which we will call the vapor cell.
- The initial state of the ensemble has to be an almost pure state, otherwise the relative phases between the atoms will destroy the ability to observe Rabi oscillations. The ensemble can be prepared in a pure state by optical pumping.
- The oscillation period should be much smaller than the two relaxation times T_1 and T_2 . The oscillation frequency can be controlled by the coupling field intensity.

2.4 The ^{87}Rb atom

Alkali atoms are ideal systems for precision measurements. Their electronic structure is rather convenient for calculations of the atomic spectrum and transitions, due to the single electron in the outer shell. In addition, their ground states split into two sub-levels with ultra-narrow natural widths. The energy difference between these

two sub-levels, referred to as hyperfine splitting, corresponds to frequencies in the microwave range. Since the natural width of these sub-levels is very narrow, the hyperfine transition frequencies can be used as highly accurate frequency standards.

The rubidium atom has an atomic number of 37 and electronic structure $[\text{Kr}]5s^1$. The outer-shell electron is unpaired, so the total spin is $S = \frac{1}{2}$, the nuclear spin $I = \frac{3}{2}$ for the ^{87}Rb isotope, and the orbital term \mathbf{L} is an integer. The fine structure is a result of the coupling between \mathbf{L} and \mathbf{S} forming the total electronic angular momentum \mathbf{J}

$$\mathbf{J} = \mathbf{S} + \mathbf{L}, \quad [2.4.1]$$

where

$$|S + L| \geq J \geq |S - L|. \quad [2.4.2]$$

Similarly, the hyperfine splitting is a result of the coupling between the total electronic angular momentum and the nuclear spin, forming the total angular momentum \mathbf{F} :

$$\mathbf{F} = \mathbf{J} + \mathbf{I}, \quad [2.4.3]$$

where

$$|I + J| \geq F \geq |I - J|. \quad [2.4.4]$$

The ground state of the ^{87}Rb atom (electronic spin $S = 1/2$, orbital angular momentum $L = 0$, and nuclear magnetic moment $I = 3/2$) forms two hyperfine states $F = 1$ and $F = 2$. The D_1 transition is from the ground state to $L = 1$, $J = 1/2$ forming an excited state with $J = 1/2$ total angular momentum and $F' = 1$ and $F' = 2$ excited states. The D_2 transition is from the ground state ($S = 1/2$, $L = 0$ and $I = 3/2$) to $L = 1$, $J = 3/2$, and therefore the excited level has four $F' = 0, 1, 2, 3$ states. Each of

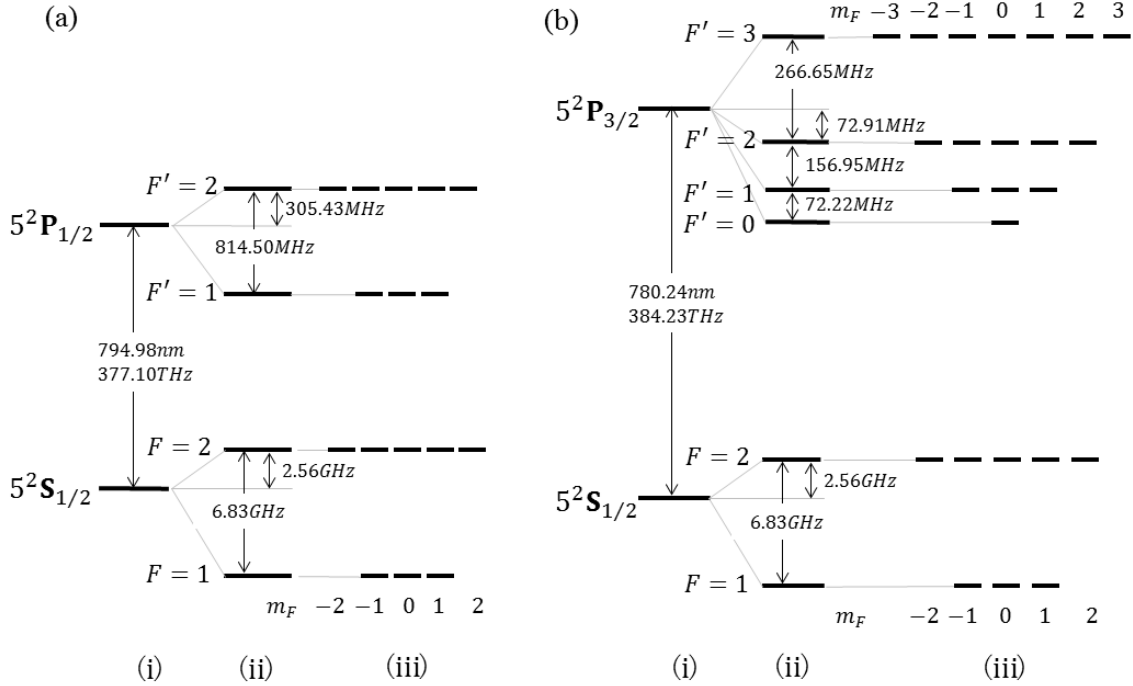


Figure 2.3: The ^{87}Rb level structure. (a) is the D_1 line and (b) is the D_2 line. (i) is the fine structure (ii) and (iii) are the hyperfine structure and the Zeeman splitting respectively.

the hyperfine states contains $2F + 1$ Zeeman, or magnetic sub-levels that determine

the angular distribution of the outer electron wave-function. In the absence of an external magnetic field, these magnetic sub-levels are degenerate. This degeneracy is removed in the presence of a magnetic field. Following [31], the interaction part of the Hamiltonian (written here in units of frequency) in the presence of a magnetic field is:

$$H_B = \frac{\mu_B}{\hbar} (g_S \mathbf{S} + g_L \mathbf{L} + g_I \mathbf{I}) \cdot \mathbf{B}, \quad [2.4.5]$$

where μ_B is the Bohr magneton, g_S , g_L and g_I are the electron spin, the electron orbital, and the nuclear “ g -factors” and \mathbf{B} is the external magnetic field. Let us consider the magnetic field along the quantization axis z which leads to:

$$H_B = \frac{\mu_B}{\hbar} (g_S S_z + g_L L_z + g_I I_z) \cdot B_z. \quad [2.4.6]$$

For small magnetic fields, so that the magnetic energy shift is small compared to the hyperfine splitting, F is a good quantum number. Then the interaction Hamiltonian becomes

$$H_B = \mu_B g_F F_z \frac{B_z}{\hbar}. \quad [2.4.7]$$

Therefore, in a first-order approximation, the eigenstates are split linearly according to:

$$\Delta E_{|F, m_F\rangle} = \mu_B g_F m_F B_z. \quad [2.4.8]$$

For much higher magnetic field, the magnetic energy shift is much larger than the hyperfine structure and J becomes a good quantum number. The interaction Hamiltonian becomes:

$$H_B = \frac{\mu_B}{\hbar} (g_J J_z + g_I I_z) B_z. \quad [2.4.9]$$

The hyperfine Hamiltonian perturbs the eigenstates $|J, m_J; I, m_I\rangle$. For high magnetic fields there is an approximation formula to calculate the energies [31].

For intermediate fields the energy shifts are difficult to calculate analytically for the general case, and the Hamiltonian $H_{\text{hfs}} + H_B$ must be diagonalized numerically. A useful exception is the Breit-Rabi formula, which applies to the ground state of the D -line transitions of ^{87}Rb atoms:

$$E_{|J=1/2, m_J; I, m_I\rangle} = -\frac{\Delta E_{\text{hfs}}}{2(2I+1)} + g_I \mu_B m_I B \pm \frac{\Delta E_{\text{hfs}}}{2} \left(1 + \frac{4m_I x}{2I+1} + x^2 \right)^{1/2}, \quad [2.4.10]$$

where ΔE_{hfs} is the hyperfine splitting, $m = m_I \pm m_J$ and

$$x = \frac{(g_J - g_I) \mu_B B}{\Delta E_{\text{hfs}}}. \quad [2.4.11]$$

In this work I address the hyperfine ground states as $F = 1$ and $F = 2$. The magnetic sub-levels of the ground state are noted as $|i, j\rangle$ where $F = i$ and $m_F = j$. An excited hyperfine state, or a transition that involves an excited hyperfine state, is noted with the electronic configuration and F' , the excited-state total angular momentum. As an example, the transition from $F = 2$ to $F' = 2$ in the D_2 manifold will be written as $5^2\text{S}_{1/2}|F = 2\rangle \leftrightarrow 5^2\text{P}_{3/2}|F' = 2\rangle$, while the excited state itself is noted as $5^2\text{P}_{3/2}|F' = 2\rangle$.

3 Experimental background

In this chapter we cover some background topics relevant to our experimental work. Section 3.1 contains a short review of relaxation processes; in Sec. 3.2 we present some examples of optical pumping and in Sec. 3.3 we deal with the absorption of light by a ^{87}Rb vapor.

3.1 Relaxation processes

In ^{87}Rb vapor, the thermal energy at room temperature is much higher than the hyperfine splitting. A temperature of 300 K is equivalent to 6.24 THz, whereas the hyperfine splitting is 6.83 GHz. Therefore, in an ensemble of ^{87}Rb in equilibrium at room temperature, the atomic population is equally distributed between the 8 Zeeman sub-levels of the ground state, which means that the population distribution between the hyperfine states is $\frac{5}{8}$ in the $F = 2$ state (which contains 5 Zeeman sub-levels) and $\frac{3}{8}$ in the $F = 1$ state (which contains 3 Zeeman sub-levels).

When we prepare an ensemble of rubidium atoms in a pure state, it will eventually relax to a mixture in a thermal equilibrium. The relaxation processes are traditionally characterized by two time constants T_1 and T_2 . T_1 relates to the tendency of an ensemble to decay to the low energy state. In room temperature rubidium vapor, T_1 relates to the time in which a coherent state decays to thermal equilibrium, a mixture of equally populated sub-levels.

T_1 can be evaluated by preparing an atomic vapor ensemble in a pure state, and then letting it evolve freely for different time intervals followed by probing the population for each of the time intervals (see Fig. 3.1). Fitting the resulting population data to an exponentially decaying function enables the extraction of the relaxation time.

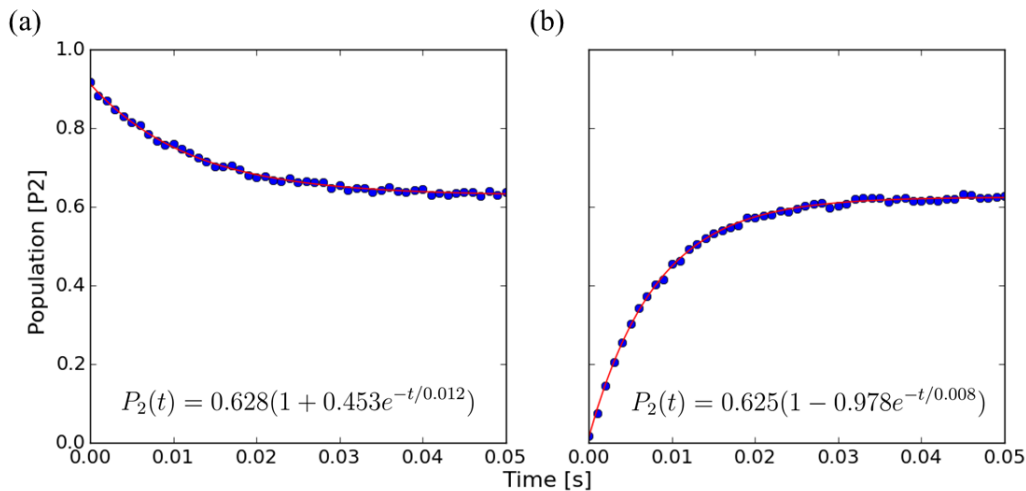


Figure 3.1: Relaxation. Experimental results showing relaxation processes in a ^{87}Rb vapor in a cell with a 7.5 Torr neon buffer gas. Data points are marked in blue, and the red line is a fit to a function of the type $P_2(t) = a(1 - be^{-t/T_1})^1$, where P_2 is the relative population in $F = 2$ and T_1 is the time that characterizes the relaxation of population from a prepared hyperfine ground state to an equilibrium. (a) The ensemble is initially pumped to the $F = 2$, $m_F = -2$ Zeeman sub-level (using two circular polarized laser beams tuned to the $F = 1 \rightarrow F' = 2$ transition in the D_2 manifold and to the $F = 2 \rightarrow F' = 2$ transition in the D_1 manifold), and then allowed to evolve freely. (b) The ensemble is pumped to the $F = 1$ hyperfine state by linearly polarized light tuned to $F = 2 \rightarrow F' = 2$, D_2 transition.

Buffer gas	pressure [Torr]	$F = 2$ relaxation time T_1 [ms]
neon	75	30
neon	7.5	8-12
krypton	60	3.2

Table 3.1: Rubidium vapor cells that have been used in this work. The cells have a cylindrical shape with a diameter of 25 mm and a 40 mm length, into which a droplet of ^{87}Rb is inserted.

The decay process related to T_2 is termed dephasing. From a density matrix perspective T_2 is the time that takes the off-diagonal density matrix elements of a pure superposition state to decay to zero.

The relaxation of the rubidium ground state is related to collisions. Elastic collisions, such as Rb-buffer gas collisions preserve coherence. Inelastic collisions, such as Rb-Rb or Rb-cell wall, will destroy coherence in a single collision. In vapor cells, the relaxation rate can be reduced by filling the cell with buffer gas and by applying coating on the cell wall.

Coating the cell wall with paraffin reduces the probability for an inelastic collision between the atom and the cell wall. Tetracontane $\text{C}_{40}\text{H}_{82}$ is a straight chain molecule with a high melting point and low vapor pressure. Tetracontane coated walls reduce the probability for an inelastic collision by four orders of magnitude [3].

Collisions of buffer gas atoms with rubidium atoms preserve coherence at up to $\sim 10^8$ collisions [2]. In addition the buffer gas environment confines the Rb atom motion to diffusion rather than ballistic-like motion, which reduces the mean free path from the order of the vapor cell dimension (without the cell confinement the mean free path of a rubidium atom at room temperature is on the order of 100 m) to 3×10^{-2} mm (for 10 Torr Ne buffer gas in room temperature) [36].

This diffusion-like motion has two advantages in a vapor cell system. It confines the probed/laser interacting atoms to the probing/interaction volume (*i.e.*, the laser beam path inside the vapor cell) for a longer time, and reduces the Rb-Rb and Rb-wall collision rate.

3.2 Optical pumping

Optical pumping is a method for polarizing a macroscopic substance by electromagnetic radiation. In vapor media, optical pumping allows us to control the distribution of the population among the quantum states of an atomic ensemble. In a vapor sample, optical pumping is typically done by optically coupling a populated (stable/ground) state with an excited (unstable/short lifetime) state. The combined effect of this coupling and of the spontaneous emission may lead to accumulation of the vapor population in a pre-selected sub-level of the ground state.

Optical pumping induces order in a system that normally is in thermal equilibrium. The relaxation and decoherence processes described in Sec. 3.1 tend to drive the system back to thermal equilibrium. Thus, we have two competing processes, each characterized by a specific rate, and the final steady state of the system is a function of these rates.

Our rubidium vapor cells are convenient systems for optical pumping. The F' excited states have a very short lifetime (~ 27 ns) leading to a high rate of spontaneous emission (which enables high optical pumping rates). The hyperfine ground state

¹This model describes the dominant behavior of relaxation processes, which is sufficient for the scope of this work (Detailed studies of these relaxation processes are available in [34],[35]).

typically has long thermal relaxation times on the order of 10-50 ms (see Tab. 3.1). Under suitable conditions, the relaxation time in rubidium vapor cells can be as high as a full minute [10, 37].

We can use the optical pumping process to modify macroscopic properties of a vapor ensemble. Modifying the hyperfine states' population strongly affects the optical density of a vapor sample. Modifying the distribution of the population among the Zeeman sub-levels changes the macroscopic magnetic moment of the vapor media. (See [38] for a comprehensive review of optical pumping).

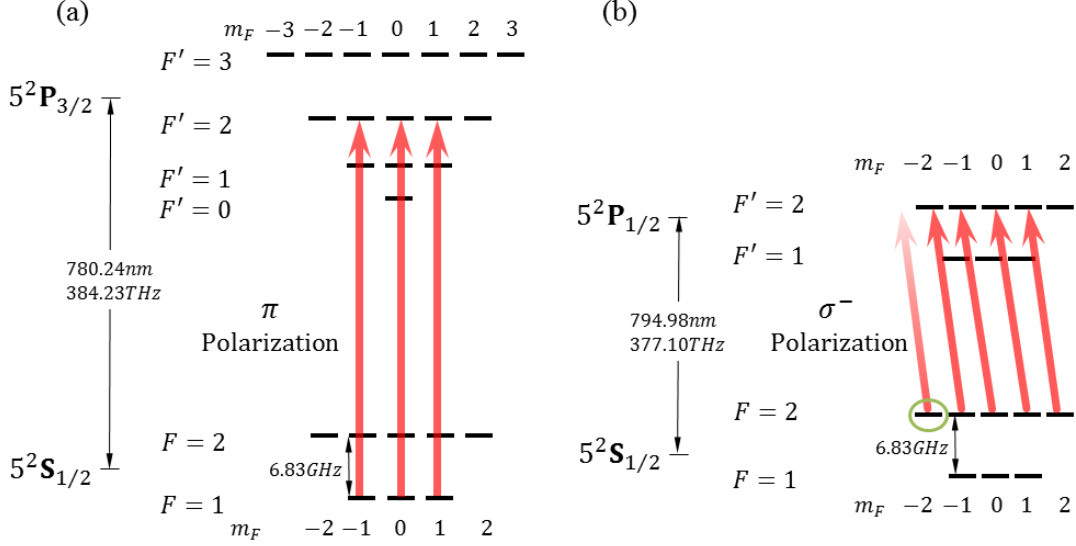


Figure 3.2: Optical pumping of the ^{87}Rb atom. (a) Optical pumping of the population to the $F = 2$ hyperfine ground state. The combined effect of a linearly polarized light tuned to the $5^2\text{S}_{1/2}|F = 1\rangle \leftrightarrow 5^2\text{P}_{3/2}|F' = 2\rangle$ transition in the D_2 manifold and spontaneous emission leads to accumulation of the population in the $F = 2$ hyperfine ground state. (b) Optical pumping of a large part of the population to the $|2, -2\rangle$ ground state Zeeman sub-level. The light is tuned to the $5^2\text{S}_{1/2}|F = 2\rangle \leftrightarrow 5^2\text{P}_{1/2}|F' = 2\rangle$ transition in the D_1 manifold, and is σ^- polarized. This beam cannot excite atoms in the $|2, -2\rangle$ ground state sub-level (marked with a green circle) which is therefore referred to as a “dark state”. Combining (a) and (b) can drive more than 99% of the population to $|2, -2\rangle$ [39].

3.3 Absorption of light by a rubidium vapor cell

When a near resonant light beam passes through a rubidium vapor cell (Fig. 3.3) some of the light is absorbed by the rubidium atoms. In steady state, this absorption is described by the Beer-Lambert law:

$$I = I_0 e^{-OD} = I_0 e^{-\sigma \cdot l \cdot n \cdot p_i}, \quad [3.3.1]$$

where I_0 is the intensity of the incident beam, I is the intensity of the beam as it emerges from the vapor cell, OD is the optical density, σ is the (frequency dependent) absorption cross section, l is the vapor cell length, n is the density of the vapor atoms, and p_i is the relative population of the atoms in the hyperfine ground state $|F = i\rangle$ that can interact with the light.

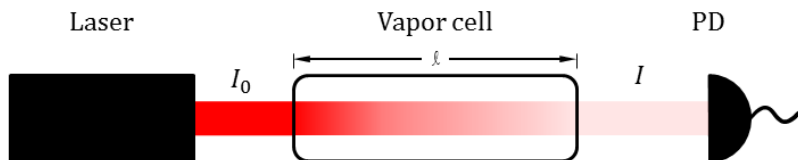


Figure 3.3: Absorption of a laser beam by a vapor cell. A laser beam with the intensity I_0 propagates through a vapor cell with length l . The intensity I of the beam as it emerges from the vapor cell is $I = I_0 e^{-OD}$, where OD is the optical density of the vapor cell (see Eq. 3.3.1).

In our system we use a strong light beam (the probe beam in Fig. 4.6) tuned near the $5^2S_{1/2}|F = 2\rangle \leftrightarrow 5^2P_{3/2}|F' = 2\rangle$ transition. The Beer-Lambert law applies to our case only if:

- The value of p_2 is uniform along the cell.
- The cross section σ is the same for atoms in different Zeeman sub-levels of the $5^2S_{1/2}|F = 2\rangle$ hyperfine state.

Our probe beam optically pumps the ^{87}Rb atoms from $5^2S_{1/2}|F = 2\rangle$ to $5^2S_{1/2}|F = 1\rangle$. The pumping rate varies with the beam intensity, which goes down along the cell, so that in general p_2 is not constant along the cell. However, there are two instances when p_2 is a constant: at the onset of the beam (allowing us to measure the value of I) and after all the population is pumped to the $5^2S_{1/2}|F = 1\rangle$ hyperfine state, and there is almost no absorption of the probe beam (letting us measure I_0). (see § 4 in [40].)

In general, the cross section σ is different for atoms in different Zeeman sub-levels of the $5^2S_{1/2}|F = 2\rangle$ hyperfine state. Thus the optical density [$OD = -\ln(I/I_0)$] is dependent not only on p_2 but also on the distribution of the population between the Zeeman sub-levels. There is just one case when the optical density is the same for atoms in different sub-levels of the $5^2S_{1/2}|F = 2\rangle$ hyperfine state: when the beam is tuned to a specific frequency, the magic frequency [27, 40]. Only then is the optical density at the onset of the probe beam proportional to the population p_2 . When the probe beam is tuned away from this magic frequency (located about 120 MHz above the $5^2S_{1/2}|F = 2\rangle \leftrightarrow 5^2P_{3/2}|F' = 2\rangle$ transition frequency) the optical density at the onset of the probe beam is sensitive to changes in the distribution of the population among the different Zeeman sub-levels of the $5^2S_{1/2}|F = 2\rangle$ state. In particular it varies by up to 4% when the population is moved from the sub-level $5^2S_{1/2}|2, -2\rangle$ to the sub-level $5^2S_{1/2}|2, -1\rangle$.

4 Experiment

In this work we study the Rabi oscillations between the Zeeman sub-levels of the ground state of ^{87}Rb atoms contained in vapor cells with a variety of buffer gases. In this chapter we describe the experimental system used for this study (Sec. 4.1) and the measuring methods we apply (Sec. 4.2). Section 4.3 is devoted to a detailed description of two ways to measure the frequency and the amplitude of these Rabi oscillations.

4.1 The experimental system

The experimental system is designed to execute versatile experimental operations on a ^{87}Rb vapor by applying external electromagnetic and magnetic fields. Three external cavity diode lasers (Sec. 4.1.1) are used to provide two pump beams and a probe beam. Each of the laser's frequencies is stabilized by a Doppler free polarization lock setup (Sec. 4.1.2). Fast switching is provided by two double-pass acousto-optical modulators (AOM) (Sec. 4.1.3). We use this system to optically pump (Sec. 3.2) the atomic population to either one of the hyperfine ground states or to the $|2, -2\rangle$ Zeeman sub-level; to measure the hyperfine ground state population (Sec. 4.2.2) and to indirectly measure the relative population of the $|2, -2\rangle$ Zeeman sub-level. A set of magnetic coils along the cell axis and radio-frequency loops (Sec. 4.1.4) are used to induce controllable Zeeman shifts and drive Rabi oscillations between the $|2, -2\rangle$ and $|2, -1\rangle$ Zeeman sub-levels. A computer controlled current source and fast current shutters are used to supply current to the magnetic coils.

4.1.1 External cavity diode laser

Diode lasers provide high intensities and long coherence-length light beams with controlled frequency. However, a diode laser frequency linewidth is much larger than the atomic transitions we wish to investigate in this work. An external cavity diode laser (ECDL) is a simple setup that reduces the laser's free spectral range and reduces the laser frequency linewidth by more than an order of magnitude. In addition, the ECDL setup lets us tune the laser frequency with a resolution better than the atomic hyperfine splitting [41].

A laser is composed of an active material (a material that allows an amplification of the light by way of stimulated emission) confined in a mirror cavity where one of the cavity's mirrors is partially transparent. In our setup we use a commercial laser diode where the active material is a P-N junction. In these types of lasers the cavity and the active material are realized in an encapsulated, mounted chip with electronic input. The volume of such a packaged diode laser is typically less than 1 cm^3 .

The cavity supports light with a wavelength λ that equals the cavity length divided by some integer. Light that makes round trips in a cavity with the length L_1 , accumulates a phase so that [42]: $2\pi m = 2\pi\nu \cdot \frac{2nL_1}{c}$, where n is the refractive index of the cavity, m is some integer, c is the speed of light in vacuum, and the frequency is $\nu = c/\lambda$. The cavity resonance frequencies are:

$$\nu_m = \frac{mc}{2nL_1}, \quad m = 1, 2, 3, \dots \quad [4.1.1]$$

The separation between two neighboring frequencies is:

$$\nu_{m+1} - \nu_m = \frac{c}{2nL_1}, \quad [4.1.2]$$

which is called the free spectral range (FSR). For the diode lasers we use in our experiment the FSR is approximately 150 GHz and the bandwidth of the modes is around tens of MHz.

The ECDL is composed of a diode laser and a tunable grating in a Littrow configuration. The system is arranged as described in Fig. 4.1. The grating reflects the first order of the diffracted laser beam back to the diode laser while the zero order is the output beam. An external cavity is formed between the back facet of the diode laser and the grating. An external cavity with a length of 3 cm reduces the FSR from 150 GHz to 5 GHz, whereas the bandwidth of the modes is reduced from around 30 MHz to less than 1 MHz. A detailed description of the ECDL and its properties is presented in [43].

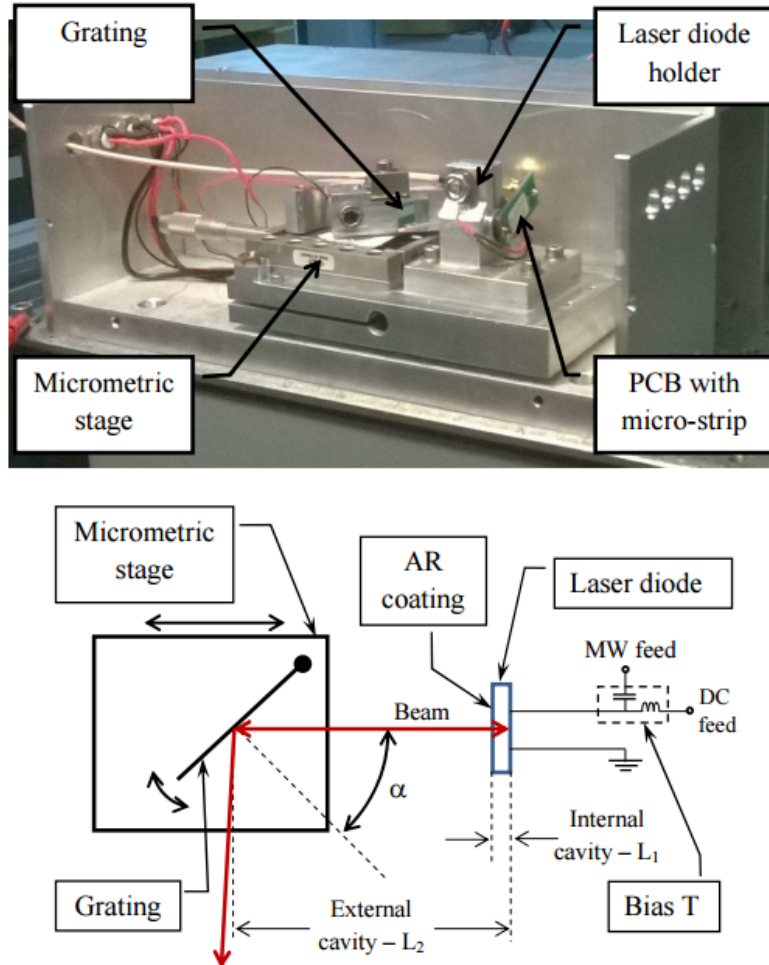


Figure 4.1: External cavity diode laser in the Littrow configuration. A diode laser emitting light on a translatable grating in a Littrow configuration. The first diffraction order is refracted back into the diode laser. An external cavity is formed by the rear facet of the diode laser and the grating, enhancing the tunable laser modes that depend on the piezoelectric controlled cavity length L_2 . The zeroth diffraction order is reflected to the experiment. Top: picture of the laser setup. Bottom: schematic diagram of the main components [40].

Fine tuning of the laser frequency is done by applying a voltage on the piezoelectric (PZT) element located behind the grating. The PZT expands under the applied voltage, changes the external cavity length and thus changes the laser frequency. By scanning the voltage on the PZT the laser frequency is scanned. The mode-hop free scanning range of our ECDL is ~ 8 GHz. (Mode hop is a result of transition between two grating modes.)

4.1.2 Laser frequency lock

The laser that we are using is exposed to frequency fluctuations and drifts that are much larger than the atomic hyperfine transition linewidth. To keep the laser frequency stable and the laser frequency linewidth narrower than that of the relevant transition it is necessary to lock the laser to a suitable frequency reference [44].

Naturally, we use a rubidium vapor cell as a frequency reference. However, Doppler broadening at room temperature hinders the narrow spectral features of the hyperfine transitions. Therefore, in order to unmask these features, we apply a polarization spectroscopy Doppler-free configuration. This configuration is a simple modulation-free technique to stabilize a laser frequency to a specific atomic transition [45].

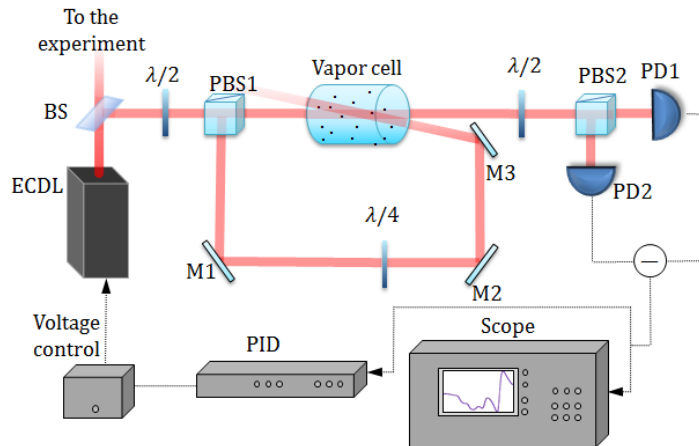


Figure 4.2: Schematic diagram of a Doppler free polarization spectroscopy setup. BS, beam sampler (piece of glass); PBS, polarized beam-splitter; M, mirror; PD, photodiode. PBS1 splits the beam to a strong pump and a weak probe. The ratio between the intensities of the two beams is set by the left hand side half-wave plate ($\lambda/2$). The quarter-wave plate ($\lambda/4$) changes the polarization of the pump beam from linear to circular. The circular polarized pump beam counter-propagates through the cell and optically pumps the rubidium vapor. The pumping process produces a non-uniform population in the Zeeman sub-levels, creating an anisotropic sample for the linearly polarized probe. This only happens when both the pump and the probe interact with the same atomic population, and due to the counter propagating nature of the setup and the Doppler shifts, this occurs when the laser is on resonance with the zero velocity population, and hence the Doppler broadening is eliminated. The linear probe beam may be decomposed into two circularly polarized beams. As the sample is now anisotropic (*i.e.* birefringent), a relative phase develops between the two probe beams. Adding these two beams after the cell amounts to a single linearly polarized probe beam which has been rotated relative to the original beam. Beam-splitter PBS2 splits this rotated probe beam to two polarization components that are measured by PD1 and PD2. The difference between the two components, which now measured the amount of rotation of the probe beam, forms an error signal that corresponds to the atomic frequencies, which the PID can lock on (see details in the text).

The setup of the Doppler free polarization spectroscopy is detailed in Fig. 4.2. Two beams counter-propagate through a ^{87}Rb vapor cell (that does not contain buffer gas): a circularly polarized beam that pumps the vapor to an anisotropic macroscopic state (pumping with a circularly polarized light populates the high magnetic moment Zeeman sub-levels) and a linearly polarized probe that measures

the vapor state. The probe beam that emerges from the vapor cell is analyzed by a polarimeter [composed of a polarizing beam-splitter (PBS) and two photodiodes]. The output of the polarimeter is the difference between the signals of the two photodiodes. The signal is composed of a series of “error-like” signals from each of the hyperfine transitions. A signal from one of the hyperfine transitions can be fed into a servo-system that locks the laser frequency to that transition.

The signals from the photo-diodes are subtracted by a home-made differential amplifier. The signal from this amplifier is entered into a home-made Proportional-Integral-Derivative (PID) controller regulator. The output of the PID regulator is applied to the high-voltage driver of the PZT crystal that determines the laser frequency.

4.1.3 Double-pass acousto-optical modulator

An acousto-optical modulator (AOM) is a device that modulates the frequency of a laser beam (temporal modulation) and deflects it (spatial modulation). The AOM is a transparent crystal with a strain transducer attached. By applying an RF signal with a frequency f to the transducer, an acoustic wave (propagating at the speed of sound in the crystal ν_s) is formed in the crystal. The refractive index is therefore modulated with a wavelength of a $\Lambda = \nu_s/f$, and the crystal acts like a diffraction grating. This behavior of the crystal is limited to the case that the acoustic wave is describable by a plane wave and all phonons have the same wave vector, and can be analyzed in terms of interaction between light photons and acoustic phonons.

A scattering process between photons and phonons results in the absorption or emission of acoustic phonons. A first-order scattering process between a photon and a single phonon is described by the energy-momentum relations [46]

$$\begin{aligned}\omega_d &= \omega_i \pm f \\ \mathbf{k}_d &= \mathbf{k}_i \pm \boldsymbol{\kappa}.\end{aligned}\tag{4.1.3}$$

The acoustic and optical fields are described as particles with momentum $\boldsymbol{\kappa}$ and \mathbf{k} , where $\boldsymbol{\kappa}$ (\mathbf{k}) is the phonon (photon) wave vector of the acoustic (optical) field. $|\mathbf{k}| = \omega/\nu_L$ where ν_L is the speed of light in the crystal, similarly $|\boldsymbol{\kappa}| = f/\nu_s$. The subscripts i and d designate whether the corresponding photon is incident or diffracted. The sign depends on whether the phonon is absorbed or emitted, which depends on the relative orientations of the incident photon and phonon wave vectors.

When the AOM is on the m th diffraction order angle relative to the incident beam we have [47]

$$\theta_m \cong \pm \frac{m\lambda}{n\Lambda},\tag{4.1.4}$$

where λ is the light wavelength and n is the refractive index. The diffracted angle depends on the light wavelength which raises an alignment problem when the laser frequency is tunable.

The scheme of the double-pass AOM we use is presented in Fig. 4.3. We align the incident beam into the AOM at an angle that maximizes the refracted order that we need, and locate the iris so that it blocks all other orders. By reflecting the chosen diffraction order back to the AOM and focusing it at the center of the AOM as described in the caption of Fig. 4.3, we get a setup that is insensitive to changes in the wavelength and allows modulation of the frequency and the power of a laser beam.

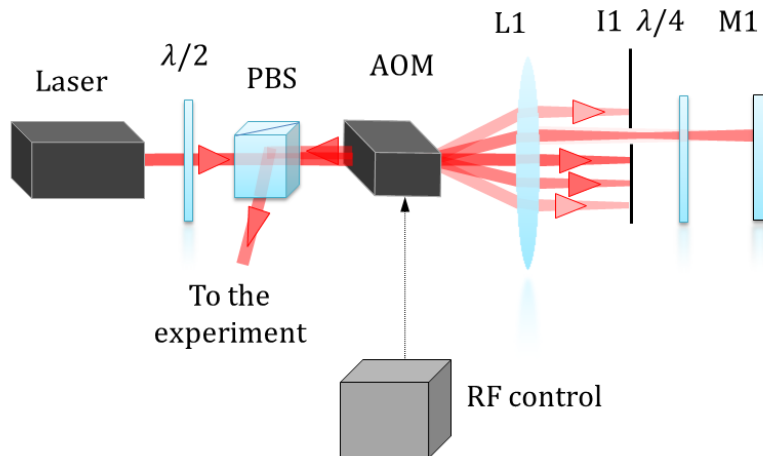


Figure 4.3: Schematic diagram of a double pass AOM. The red line that comes out of the laser (marked with a right arrow) indicates a linearly polarized beam. The direction of the incident beam polarization is set by the half-wave plate ($\lambda/2$), so that the incident beam fully passes through the PBS. When the frequency generator is off, the beam passes through the AOM without deflection and is blocked by the iris (I1). When an RF signal at a frequency f is applied to the AOM, diffraction occurs and splits the incident beam into several diffracted beams. The frequency of each diffracted beam is shifted by $m \cdot f$, where m is the diffraction order of that beam. The iris (I1) is set so that only the desired diffracted beam will pass through it and then through the quarter-wave plate ($\lambda/4$) to the mirror (M1). As the AOM is in the focal point of a lens (L1), all diffracted beams at any diffraction angle are perpendicular to the mirror surface and are reflected upon themselves. The quarter-wave plate changes the polarization of the beam from a linear polarization to a circular polarization, while the mirror reflects and rotates the circular polarization by π (when a σ^+ polarized beam reflects from a mirror, in the lab frame, the reflected beam polarization is σ^- and vice versa). The quarter-wave plate changes the polarization of the reflected beam to linear with a polarization direction perpendicular to the incident beam polarization direction, so that after passing again through the AOM and gaining an additional $m \cdot f$ frequency shift, the reflected beam is fully deflected by the PBS with its frequency shifted by $2m \cdot f$.

In this work we used two kinds of AOMs with the suitable drivers to modulate the pump and the probe beams:

- AOM 1: modulating the probe laser. AOM type 3110-140, with 1110AF-DEFO 1.5W AOM driver, both made by Crystal Technology Inc. The frequency range is 110 ± 25 MHz. One experimental control analog output controls the driver's frequency, and another controls the driver's power. This second output is also used to switch the AOM driver on and off.
- AOM 2: modulating the pump lasers. AOM type 3080-125, with 1080AF-AIFO 1.0 W AOM driver, both made by Crystal Technology Inc. This AOM operates at a fixed frequency of 80 MHz. Only one analog output is needed to control both the AOM power and to switch it on and off.

4.1.4 Applying external fields on the vapor cell

The vapor cell is located inside a system of solenoids that is composed from a main z coil; auxiliary z and y coils; 3 sets of Helmholtz coils and RF loops (see Fig. 4.4,

4.5 and 4.6). The main and auxiliary z coils can produce a magnetic field of up to 30 G parallel to the cell's axis and in the direction of the laser beams propagation (see Fig. 4.4). The z coils allow us to control the Zeeman splitting magnitude. The z coils and the auxiliary y coil can be switched off by fast current shutters with a controllable (few microseconds to several milliseconds) shutting time. Three pairs of square Helmholtz coils are positioned around the vapor cell and can generate a magnetic field of up to ± 1.5 G along each of the axes of the cell. Each of the Helmholtz coil pairs is supplied by a different current source. The Helmholtz coils are set to cancel the earth's magnetic field in the volume of the cell. A fourth Helmholtz coil pair, the auxiliary y coil, is set in the y direction and can deliver a controlled magnetic field of ± 1 G.

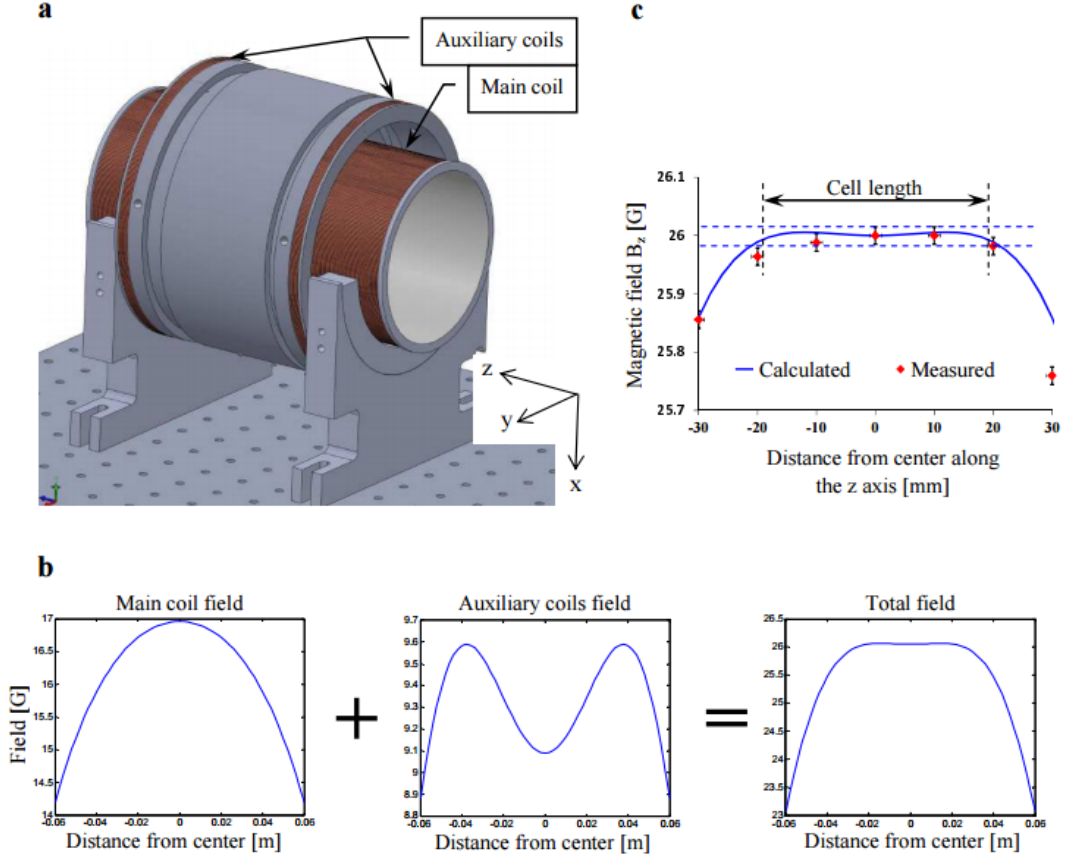


Figure 4.4: z direction magnetic field coils apparatus. The main magnetic DC coil (inside) and the auxiliary coil (outside). The vapor cell (not shown) is located at the center of the main coil. b. Calculation of the combined magnetic field of the coils (current 2.6 A in all three coils). The distance between the auxiliary coils is adjusted so that the total field is uniform along the length of the cell (38 mm). Comparison between the calculated and the measured magnetic fields. The dashed blue lines indicate a 0.015% tolerance for the field magnitude along the length of the cell (z axis), and the vertical error bars represent the 15 mG repeatability of the Gauss-meter [40].

The RF loop arrangement (presented in Fig. 4.5) is located inside the main z coil. The RF coil is driven by a frequency generator that can deliver frequencies up to 20 MHz and is controlled by the experimental system's computer.

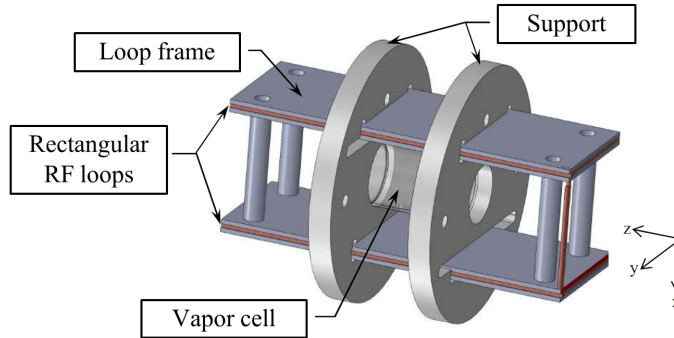


Figure 4.5: The RF loop arrangement. The RF field is created by two rectangular loops, held in place by the loop frame. The supports hold the RF loop coils and the vapor cell together. The whole RF loop arrangement is inserted into the axial coil arrangement (see Fig. 4.4). Note that the RF magnetic field oscillates along the x direction, while the DC magnetic field is along the z axis [40].

4.1.5 Vapor cell measurement setup

A schematic plot of the full experimental setup is shown in Fig. 4.6. The setup plot is overlaid with the optical path of the laser beams, the coils that apply the external fields and the setup control scheme. Each of the laser beams splits to low and high intensity beams by beam-splitters. Each of the low intensity beams is fed into a polarization frequency lock (Sec. 4.1.2) to determine and stabilize the frequency. The pump lasers are combined and fed into a single double-pass AOM (Sec. 4.1.3), while the probe laser is controlled with a second double-pass AOM. The combined pump lasers' polarization is changed by a 795 nm quarter wave-plate ($\lambda/4$) so that the 795 nm laser is fully circularly polarized whereas the 780 nm pump laser is partially circularly polarized. The two pump beams and the probe beam that emerge from the AOMs are combined by a non-polarizing beam-splitter cube. The 3 combined beams' diameter is set to 12 mm by a two-lens telescope and an iris. The 3 beams propagate from the iris through the vapor cell. An additional lens is positioned after the cell to focus the laser beams onto the photodiode PD (Fig. 4.6). The photodiode signal is recorded on a scope which can be triggered either by the signal generator or by the system's computer. The scope data are downloaded to the computer for storage and analysis.

The z coils and two RF loops provide a magnetic field and an electromagnetic RF field to the vapor cell (see Sec. 4.1.4).

The experimental system is controlled by a desktop computer equipped with a National Instruments NI PCI 6733 high-speed analog output card. The control system operates the laser switching by the double-pass AOMs, the fast switching of the external z and y DC magnetic field coils and the RF loop. The control system can establish 2-way communication (via GPIB) with the current drivers of the z and y coils and with the scope (see Sec. 4.1.6).

We can utilize the experimental system to pump the vapor population either to the $F = 1$ or $F = 2$ hyperfine ground states; to pump the vapor to the $|2, -2\rangle$ or $|2, 2\rangle$ Zeeman sub-levels (Sec. 3.2); measure the relative population of the $F = 2$ hyperfine ground state (Sec. 4.2.2); perform an RF radiation frequency scan to find the transition frequency between the Zeeman sub-levels (Sec. 4.3) and induce and record Rabi oscillations (Sec. 4.4).

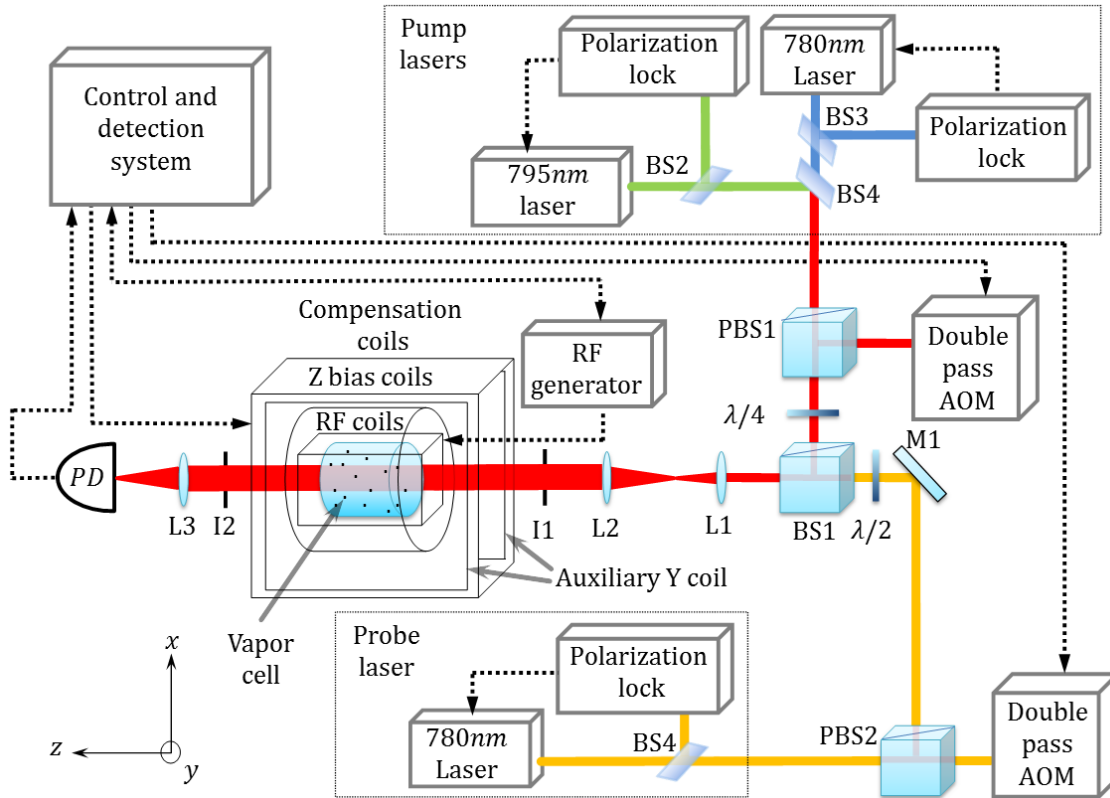


Figure 4.6: Scheme of the Rabi oscillations measurement setup. BS1, BS2, BS3, BS4, beam-splitters; PBS1, PBS2, polarized beam-splitters; L1, L2, L3 lenses; I1, I2, iris; M1 mirror, PD photo diode. Dashed lines indicate data and control lines. The double pass AOM can turn the laser beams on and off within $1 \mu\text{s}$. The lenses L1 and L2 and the iris control the diameter and the intensity profile of the beam. The compensation coils cancel the earth's magnetic field, the z bias coils produce a $26.09 \pm 0.01\text{G}$ DC magnetic field parallel to the axis of the vapor cell and the auxiliary y coils produce a 1G magnetic field in y direction. The z and y magnetic fields are controlled by fast current shutters that can switch the magnetic field off in less than 1ms . The RF coils produce an AC magnetic field perpendicular to the vapor cell axis. The pump lasers are tuned to the $F = 1 \leftrightarrow F' = 2$ transition in the D_2 manifold (marked in blue) and to the $F = 2 \leftrightarrow F' = 2$ transition in the D_1 (marked in green). BS4 combines the two pump lasers, and the quarter-wave plate changes the polarization of the beams from linear to circular. The combined circularly polarized beams drive a uniformly distributed ground state population to the $F = 2, m_F = -2$ sub-level (which is a dark state for both of the beams). The probe laser is tuned to a frequency near the $F = 2 \leftrightarrow F' = 2$ transition in the D_2 manifold (marked in yellow) and a half-wave plate, $\lambda/2$, is set to fix the probe beam polarization in the y direction. The probe beam is combined with the pump beam by BS1. The beams pass through the vapor cell and the intensity of the beams is recorded as a function of time. The control system allows the creation of a variety of sequences combining beams, magnetic fields and RF radiation.

4.1.6 The computer-experimental setup interface

The experimental system is controlled by a desktop computer equipped with a National Instruments NI PCI 6733 high-speed analog output card. A control program for the experiment system was developed on the LabView 2010 graphic platform. The PCI 6733 card enables “real time” operation (in a time resolution of $1 \mu\text{s}$) of some parts of the experimental system. The control program coordinates and se-

quences the operation of all devices and controls the transfer of digital data from some of these devices via digital communication provided by the general-purpose interface bus (GPIB).

The PCI 6733 card's analog outputs control the following elements:

- AOM type 3110-140, with 1110 AF-DEFO 1.5 W AOM driver (this AOM is part of the double pass AOM that controls the probe laser).
- AOM type 3080-125, with 1080 AF-AIFO 1.0 W AOM driver (this AOM is part of the double pass AOM that controls the pump laser).
- Current shutters that are capable of switching off an inductively-loaded current within $\sim 2 \mu\text{s}$.

The following devices are primarily controlled via digital communication provided by the GPIB:

- Agilent 66312 A 20 V, 2 A DC current source: This current source supplies current (via a current shutter) to the additional y axis Helmholtz coils (see Fig. 4.6).
- HP 6632 A 20 V, 5 A DC power supply. This power supply drives current (via a current shutter) to the z coil (Sec. 4.1.4).
- Agilent 33220 A 20 MHz arbitrary waveform generator: The computer program sets the frequency and amplitude of the signal, turns it on and off, and selects modes of operation (CW, pulsed, frequency sweep etc.). The digital output of the PCI 6733 card provides accurate triggering of pulses and frequency sweeps.
- Tectronix TDS 1002 60 MHz 2-channel 8-bit digital oscilloscope: This scope reads the current of the photodiode (marked PD, see Fig. 4.6). The computer program sets the modes of operation and downloads waveform data from the scope, via the GPIB digital communication. A digital output of the PCI 6733 card is connected to the external trigger port of the scope, providing accurate triggering.

4.2 Methods

In this section we describe the experimental methods we use. Section 4.2.1 is dedicated to describing the atomic transition we used for Rabi oscillations and arguing that such a system can serve for a Rabi oscillations experiment. Section 4.2.2 is dedicated to explaining the hyperfine state population measurement and to discussing the calibration considerations.

4.2.1 Inducing radio frequency Rabi oscillations between $|2, -2\rangle \leftrightarrow |2, -1\rangle$ Zeeman sub-levels

There are several ways to define a two-level system in ^{87}Rb vapor. In our work we focus on the $|2, -2\rangle$ and the $|2, -1\rangle$ ground state Zeeman sub-levels under a DC magnetic field in the range of 26 G as a two-level system. This system has several properties that make it a good approximation of a two-level system:

- The frequency of the transition is set by the external magnetic field according to Breit-Rabi Eq. 2.4.10.

- Second order magnetic Zeeman shifts allow a sufficient energetic separation between neighboring transitions. For example, when the magnetic field is large enough, the frequency of the $|2, -2\rangle \leftrightarrow |2, -1\rangle$ transition is far enough from the $|2, -1\rangle \leftrightarrow |2, 0\rangle$ transition, so that the RF radiation that induces the $|2, -2\rangle \leftrightarrow |2, -1\rangle$ transition will not induce the $|2, -1\rangle \leftrightarrow |2, 0\rangle$ transition. Hence, the population will not leak to the $|2, 0\rangle$ sub-level so that we can regard the $|2, -2\rangle$ and the $|2, -1\rangle$ ground state Zeeman sub-levels as a two-level system:
- The system can be prepared so that a significant part of the population populates one of these sub-levels. We can optically pump the population to the $|2, 2\rangle$ or $|2, -2\rangle$ Zeeman sub-levels with two laser beams as describe in Sec. 3.2.

When a large fraction of the population is pumped to the $|2, -2\rangle$ sub-level, radiation with a frequency near the $|2, -2\rangle \leftrightarrow |2, -1\rangle$ transition frequency with its magnetic component perpendicular to DC magnetic field will drive the population between the $|2, -2\rangle$ and $|2, -1\rangle$ sub-levels. [The choice of the direction of the fields can be explained from the two degenerate state system Hamiltonian. The constant magnetic field in the z direction removes the degeneracy (Sec. 2.4) and the oscillating field in the x direction, the RF, drives the population between the two sub-levels (Sec. 2.1) as it is able to flip the spins.]

4.2.2 Hyperfine state population measurements

Hyperfine state population measurement is an important tool for this work. It is a method to measure the population distribution among the hyperfine ground states [40, 48]. We use this tool to estimate the atomic ensemble’s relaxations time (Sec. 3.1) and to measure Rabi oscillations “in-the-dark” (Sec. 4.4.1).

The setup for hyperfine state population measurement is part of the system detailed in Fig. 4.6. The RF radiation, the pump lasers and the bias DC magnetic field are off; the compensation coils and the auxiliary y coils produce a 1 G magnetic field along the y axis; the probe beam is linearly polarized in the y direction so that the beam is π polarized.

Let us define the time we want to measure the population as t_0 . Prior to t_0 , we tune the probe laser to the magic frequency [27] (about 120 MHz above the $5^2S_{1/2}|F = 2\rangle \leftrightarrow 5^2P_{3/2}|F' = 2\rangle$ transition. The exact value of the magic frequency depends on the type and pressure of the buffer gas). At time t_0 the probe laser is turned on and the scope is triggered. The scope records (via the photodiode PD, Fig. 4.6) the intensity of the light transmitted through the vapor cell. The probe laser intensity is high enough to optically pump all the population to the $F = 1$ hyperfine state, and consequentially the cell becomes transparent as the atoms in this state do not interact with the light due to the 6.8 GHz detuning.

At the time that the probe laser is turned on (t_0) the intensity of the beam (see Eq. 3.3.1) is:

$$I(t_0) = I_0 e^{-[\sigma \cdot l \cdot n \cdot p_2(t_0)]}, \quad [4.2.1]$$

where I_0 is the intensity of the incident beam, I is the intensity of the beam as it emerges from the vapor cell and measured by the photodiode PD (see Fig. 4.6), σ is the absorption cross section, l is the vapor cell length, n is the density of the ^{87}Rb atoms in the vapor cell, and p_2 is the relative population of the atoms in the hyperfine ground state $|F = 2\rangle$.

At time t_f the population is concentrated in the $F = 1$ hyperfine state, so that at time t_f the population of the $F = 2$ hyperfine state is $p_2 \simeq 0$. Hence we have:

$$I(t_f) = I_0 e^{-[\sigma \cdot l \cdot n \cdot p_2(t_f)]} \simeq I_0. \quad [4.2.2]$$

From Eq. 4.2.1 and 4.2.2 we get:

$$\ln \frac{I(t_0)}{I(t_f)} \simeq \ln \left(\frac{I_0 e^{-[\sigma \cdot l \cdot n \cdot p_2(t_0)]}}{I_0} \right) = -\sigma \cdot l \cdot n \cdot p_2(t_0). \quad [4.2.3]$$

We can estimate $\sigma \cdot l \cdot n$ since all of the variables are measurable physical properties. However, it is rather challenging to do this with sufficient accuracy. We can avoid these estimations by a calibration measurement.

Since the thermal energy at room temperature is much higher than the ground state hyperfine splitting and obviously the Zeeman splitting (as mentioned in Sec. 3.1), it is safe to assume that in room-temperature thermal equilibrium the population is equally distributed among the Zeeman sub-levels. Thus, in equilibrium the $F = 2$ hyperfine ground state is populated by 5/8 of the population and the $F = 1$ hyperfine ground state is populated by 3/8 of the population. Accordingly, in room temperature equilibrium $p_2(t_0) = 5/8$ so:

$$\ln \frac{I(t_0)}{I(t_f)} = -\sigma \cdot l \cdot n \cdot 5/8. \quad [4.2.4]$$

Let us define a calibration factor k :

$$k = \frac{1}{5/8} \ln \left(\frac{I_0 e^{-[\sigma \cdot l \cdot n \cdot 5/8]}}{I_0} \right) = -\sigma \cdot l \cdot n. \quad [4.2.5]$$

thus, prior to a set of hyperfine state population measurements we need to perform a calibration measurement at room temperature equilibrium and measure k . Then,

$$p_2 = \frac{1}{k} \ln \frac{I(t_0)}{I(t_f)}. \quad [4.2.6]$$

Measuring $I(t_0)$ and $I(t_f)$ is a destructive measurement. If we wish to acquire an evolution profile of the p_2 population from an initial state under specific conditions we need to prepare that initial state, let it evolve under the specified conditions for a time t , measure the p_2 population and repeat this process for different time intervals t .

4.3 Inducing Rabi oscillations

In the next section we introduce two ways developed in our lab to measure Rabi oscillations between the Zeeman sub-levels of ^{87}Rb vapor. Both methods require the same preliminary stages: tuning of the lasers and the external fields before we induce and measure the Rabi oscillations of the ^{87}Rb atoms in the vapor cell.

Tuning the pump lasers: two pump lasers (Figs. 3.2 and 4.6) are used to optically pump most of the ^{87}Rb population to the $|2, -2\rangle$ Zeeman sub-level (see Fig. 2.3). Thus the frequency of the 780 nm laser should be near the $5^2\text{S}_{1/2}|F = 1\rangle \leftrightarrow 5^2\text{P}_{3/2}|F' = 2\rangle$ transition frequency. Taking into account that the double pass AOM adds 160 MHz (see Sec. 4.1.3) to the beam's frequency, we use the polarization spectroscopy locking method (Sec. 4.1.2) to lock this laser to the "cross-over" error signal located midway between the error signals of the $5^2\text{P}_{3/2}|F' = 1\rangle$ and $5^2\text{P}_{3/2}|F' = 2\rangle$ states.

The 795 nm laser is circularly polarized (σ^-) and tuned to the $5^2\text{S}_{1/2}|F = 2\rangle \leftrightarrow 5^2\text{P}_{1/2}|F' = 2\rangle$ transition frequency error signal by another polarization spectroscopy system. After the frequency locking, the 795 nm beam is combined with the 780 nm beam so it also gains a 160 MHz via the same double-pass AOM. The 160 MHz detuning of this laser from the $5^2\text{S}_{1/2}|F = 2\rangle \leftrightarrow 5^2\text{P}_{1/2}|F' = 2\rangle$

transition reduces the pump efficiency. However, while the Doppler broadening of the $5^2P_{1/2}$ states (around 500 MHz) is much larger than the detuning, it is still smaller than the spacing between the $5^2P_{1/2}|F' = 2\rangle$ and $5^2P_{1/2}|F' = 1\rangle$ excited hyperfine states, so the population is mostly excited from $5^2S_{1/2}|F = 2\rangle$ hyperfine state to the $5^2P_{1/2}|F' = 2\rangle$ hyperfine state and not to the $5^2P_{1/2}|F' = 1\rangle$ hyperfine state.

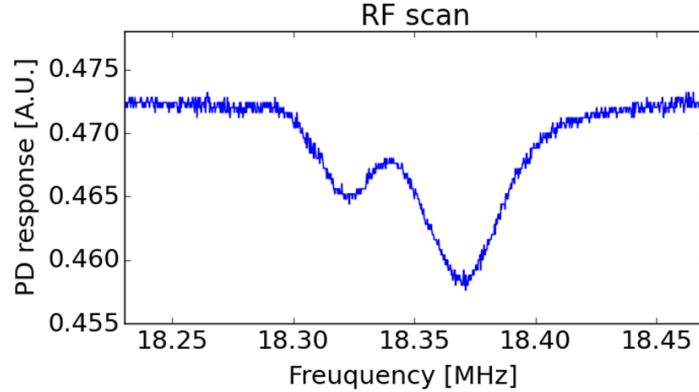


Figure 4.7: Absorption profile for a near $|2, -2\rangle \leftrightarrow |2, -1\rangle$ resonance RF scan. Absorption profile (in blue) of the pumping light passing through a rubidium vapor cell during a sweep of the RF frequency. The optical power, recorded by the PD (see Fig. 4.6), is plotted versus the RF frequency. During the RF sweep, the magnetic field is 26 G along the cell’s axis, and the light from both pump lasers passes through the cell. A bandpass filter located after the cell blocks the 780 nm light, so that only the 795 nm light is recorded by the PD. When RF frequency is far detuned from the $|2, -2\rangle \leftrightarrow |2, -1\rangle$ transition, all the rubidium atoms are in $|2, -2\rangle$ and the vapor cell is transparent to the pumping light. When the RF frequency approaches the transition frequency, the population of state $|2, -1\rangle$ builds up, causing higher absorption of the 795 nm light. The secondary dip in the cell’s transmission is due to a two-photon transition from the $|2, -2\rangle$ to $|2, 0\rangle$ Zeeman sub-levels. The secondary dip center is at the average of the $|2, -2\rangle \leftrightarrow |2, -1\rangle$ and $|2, -1\rangle \leftrightarrow |2, 0\rangle$ transition frequencies.

The 780 nm probe laser frequency is also controlled by a polarization frequency lock and it is switched by a double pass AOM that adds 220 MHz to the light frequency. It is important to note that for a Rabi oscillation measurement between the Zeeman sub-levels we have to avoid the magic frequency. Probing the population in the magic frequency with a π polarized light is insensitive to the distribution of the population among the Zeeman sub-levels. Hence, even if the population is oscillating between two different Zeeman sub-levels the outcome of a measurement in the magic frequency is the population of the hyperfine state regardless of the distribution of the population between the sub-levels. The magic frequency is a result of a unique cancellation of the difference between the coupling coefficients (Clebsch-Gordan coefficients) of the Zeeman sub-levels to the excited states in a specific detuning value - the magic frequency [27]. For ^{87}Rb the magic frequency is located 120 MHz above the $5^2S_{1/2}|F = 2\rangle \leftrightarrow 5^2P_{3/2}|F' = 2\rangle$ transition frequency. Thus, locking the probe laser on the $5^2S_{1/2}|F = 2\rangle \leftrightarrow 5^2P_{3/2}|F' = 2\rangle$ transition error signal together with the 220 MHz that is added by the double pass AOM, enables the detection of Rabi oscillations between the Zeeman sub-levels.

Calibrating the probe beam measurement: we ran a calibration process to correlate between the absorption profile of the probe and the population of the $F = 2$ hyperfine state (Sec. 4.2.2).

A good way to validate that the optical pumping to the $|2, -2\rangle$ Zeeman sub-level is sufficient and that the detection system is calibrated is to run a relaxation measurement (Sec. 3.1). Acquiring a relaxation profile with an initial population of $F = 2, p_2$ in the range of $0.9 < p_2(t = 0) < 1$ indicates that the pumping is sufficient and an asymptotic (after a long time) value of $p_2 = 0.625$ indicates that the system is calibrated.

The next stage is to locate exactly the $|2, -2\rangle \leftrightarrow |2, -1\rangle$ transition frequency at the ~ 26 G DC magnetic field applied to the vapor cell. This magnetic field is produced by the combined operation of the Helmholtz coils and the z coils (Sec. 4.1.4). It was measured by dismounting the vapor cell and measuring with a Gauss-meter the DC magnetic field in the cell's location. We use the Breit-Rabi formula (Eq. 2.4.10) to calculate the $|2, -2\rangle \leftrightarrow |2, -1\rangle$ transition frequency. However, the magnetic field measurement is not accurate enough.

To pinpoint the $|2, -2\rangle \leftrightarrow |2, -1\rangle$ transition frequency, we turn on the DC magnetic fields and the two pump beams so that the ^{87}Rb population is optically pumped to the $|2, -2\rangle$ sub-level (see Sec. 3.2). In the path of the light that emerges from the vapor cell, we use a band-pass filter to block the 780 nm beam, while the 795 nm light goes through and its intensity is measured by the photodiode PD (Fig. 4.6).

When most of the population is pumped to the $|2, -2\rangle$ sub-level the vapor is transparent to the 795 nm laser beam. We then apply RF radiation to the vapor cell via the RF loops (Fig. 4.5) while sweeping the RF frequency across the calculated transition frequency. We simultaneously record the intensity of the 795 nm beam as measured by the photodiode PD. When the RF radiation frequency approaches the frequency of the $|2, -2\rangle \leftrightarrow |2, -1\rangle$ Zeeman sub-level transition, the RF radiation induces transitions from the $|2, -2\rangle$ to the $|2, -1\rangle$ Zeeman sub-level, which can interact with the 795 nm pump beam. As a result, its intensity (measured by the photodiode PD) decreases, creating an intensity dip in the intensity profile as shown in Fig. 4.7. The RF frequency corresponding to the center of this dip is the exact $|2, -2\rangle \leftrightarrow |2, -1\rangle$ transition frequency.

4.4 Two types of Rabi measurements

We employ two methods to record the $|2, -2\rangle \leftrightarrow |2, -1\rangle$ Rabi oscillations. Before we describe the two methods, we summarize in Tab. 4.1 the frequencies and polarizations of the three lasers.

Laser	Polarization	Tuning
795 nm pump	σ^-	160 MHz blue detuned from the $5^2\text{S}_{1/2} F = 2\rangle \leftrightarrow 5^2\text{P}_{1/2} F' = 2\rangle$ transition
780 nm pump	σ^-	160 MHz blue detuned from the $5^2\text{S}_{1/2} F = 1\rangle \leftrightarrow 5^2\text{P}_{3/2} F' = 2\rangle$ transition
780 nm probe	π	220 MHz blue detuned from the $5^2\text{S}_{1/2} F = 2\rangle \leftrightarrow 5^2\text{P}_{3/2} F' = 2\rangle$ transition

Table 4.1: A summary of the lasers that we used in our setup. The lasers are locked to an atomic transition and pass through a double-pass AOM which increases the frequency of each of the lasers. The magic frequency which should be avoided is 120 MHz above the $5^2\text{S}_{1/2}|F = 2\rangle \leftrightarrow 5^2\text{P}_{3/2}|F' = 2\rangle$ transition (relevant only to the probe laser).

Both methods start in the same way: we turn on the ~ 26 G DC magnetic field and the two pump beams (Fig. 4.6). We wait (a few milliseconds) until about 90% of the ^{87}Rb population in the vapor cell is pumped to the $|2, -2\rangle$ sub-level, and then proceed according to the chosen method: either Rabi “in-the-dark” (Sec. 4.4.1) or Rabi “on-the-fly” (Sec. 4.4.2).

4.4.1 Rabi “in-the-dark” measurement

We initiate our Rabi “in-the-dark” measurement when a large part of the population is pumped to the $|2, -2\rangle$ Zeeman sub-level and a 26 G magnetic field in the z direction is applied to the cell.

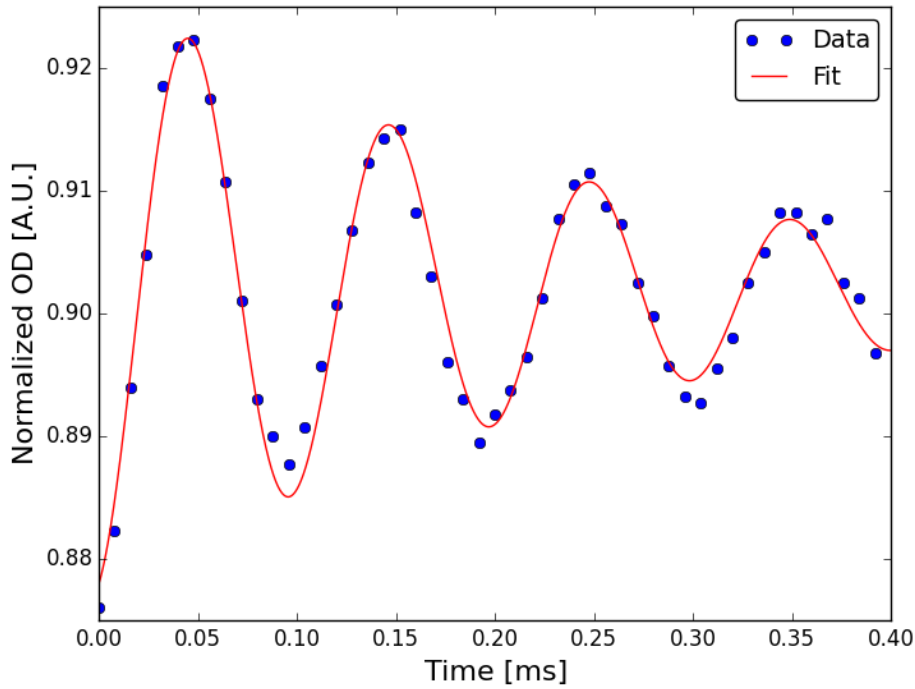


Figure 4.8: Measurement of Rabi oscillations “in-the-dark” in a ^{87}Rb vapor cell with a 75 Torr neon buffer gas. The data points (blue dots) are the optical densities of the vapor (Eq. 3.3.1) measured by a population measurement method (see Sec. 4.2.2 for further details) in different time intervals. The data points are fitted to an oscillating function of the form of Eq. 5.1.1 (red line). The experimental system used for Rabi “in-the-dark” measurements, is shown in Fig. 4.6. The Rabi “in-the-dark” sequence is performed as follows: a 26 G DC magnetic field is applied along the cell in the beam propagation direction z ; the atomic population is pumped by the two pump beams (795 and 780 nm circularly polarized light) to the $|2, -2\rangle$ sub-level; an RF field is applied on the vapor causing $|2, -2\rangle \leftrightarrow |2, -1\rangle$ Rabi oscillations of the population for a time t . Subsequently after time t the RF field is turned off and the DC magnetic field is reduced adiabatically to 1 G polarization direction of the linearly polarized probe, *i.e.* y . After the magnetic field sets to 1 G in the y direction a “population measurement” sequence is performed, measuring the optical density of the vapor. This sequence is performed for 50 different times t , along 0.4 ms. The oscillations of the optical density reflect the $|2, -2\rangle \leftrightarrow |2, -1\rangle$ Rabi oscillations.

When the $|2, -2\rangle$ Zeeman sub-level is sufficiently populated we turn the pump beams off and apply with the RF loops (Fig. 4.5 and 4.6) RF radiation at a frequency which equals to the sum of the $|2, -2\rangle \leftrightarrow |2, -1\rangle$ transition frequency and some

detuning δ . This radiation induces $|2, -2\rangle \leftrightarrow |2, -1\rangle$ Rabi oscillations. After a time t we turn off the RF radiation, the magnetic field from the z coils and the auxiliary y coils. The coils' current shutters take about 1 millisecond to shut off the currents. As a result, the magnetic field changes adiabatically from ~ 26 G in the z direction to ~ 1 G in the y direction, the direction of the probe beam polarization. We can regard the change of the magnetic field as adiabatic since the change rate of the magnetic field is much lower than the Larmor frequency. Thus this change does not disturb the state of the ^{87}Rb atoms.

The next step is to apply a hyperfine state population measurement (Sec. 4.2.2). The population measurement result (normalized OD , see Sec. 3.3) is a “calibrated” absorbance of the vapor (absorbance divided by the calibration constant k of Eq. 4.2.5). We then modify the RF radiation duration t and repeat the sequence described above for 50 different values of t , from 0 to 0.4 ms. In Fig. 4.8 we present such a plot of the normalized OD as a function of t . The measuring beam is detuned by -125 MHz from the magic frequency.

In order to get a dependance of the OD on the population of the Zeeman sub-levels we need to verify that the probe beam frequency is sufficiently far from the magic frequency [27, 40, 48]. As the double pass AOM merely serves as a switch, the probe beam frequency is fixed by the laser frequency lock (Sec. 4.1.2).

We repeat the measurement and average our results as follows: each set is an average of 4 to 6 runs, where each run consists of 50 normalized OD points taken at different Rabi oscillations evolution times. Each normalized OD point is an average of 10 measurements (this averaging is done by the scope).

4.4.2 Rabi “on-the-fly” measurement

The setup we use for Rabi “on-the-fly” is presented in Fig. 4.6; the probe does not take a part in this measurement. In addition, as the pump beams emerge from the vapor cell, the 780 nm beam is filtered out by a band-pass filter whereas the intensity of the 795 nm beam is constantly recorded by the photodiode PD on the scope. This measurement which, contrary to the previous method, utilizes constant monitoring by a light beam, makes available the Rabi oscillations graph in a single run. While this is an obvious advantage, this method suffers from the fact that as long as the laser light is on, the two-level system may be seen as not completely isolated.

We start the Rabi “on-the-fly” measurement when the 26 G magnetic field and the two pump beams are on and most of the population is already pumped to the $|2, -2\rangle$ Zeeman sub-level. Under these conditions the intensity of the 795 nm pump on the photodiode is maximal as the ^{87}Rb vapor is in a dark state (see Sec. 3.2). We then turn on the RF field (see Sec. 4.1.4) which induces $|2, -2\rangle$ to $|2, -1\rangle$ Rabi oscillations. The absorption of the 795 nm pump beam by the ^{87}Rb vapor depends on the population in the $|2, -1\rangle$ Zeeman sub-level. (The absorption of the 795 nm σ^- polarized beam is independent of the population in the dark state $|2, -2\rangle$, but depends on the population in each of the other Zeeman sub-levels due to different absorption rates of each of these sub-levels [27]). Thus, the $|2, -2\rangle$ to $|2, -1\rangle$ population oscillations are imprinted on the intensity profile recorded by the photodiode, and produce a plot as shown in Fig. 4.9.

We note the quite sharp decay of the amplitude of the oscillations. This is due, in part, to the thermal relaxation processes, and also to the scattering of the population to other sub-levels due to spontaneous emission from the excited $5^2\text{P}_{1/2}$ hyperfine state.

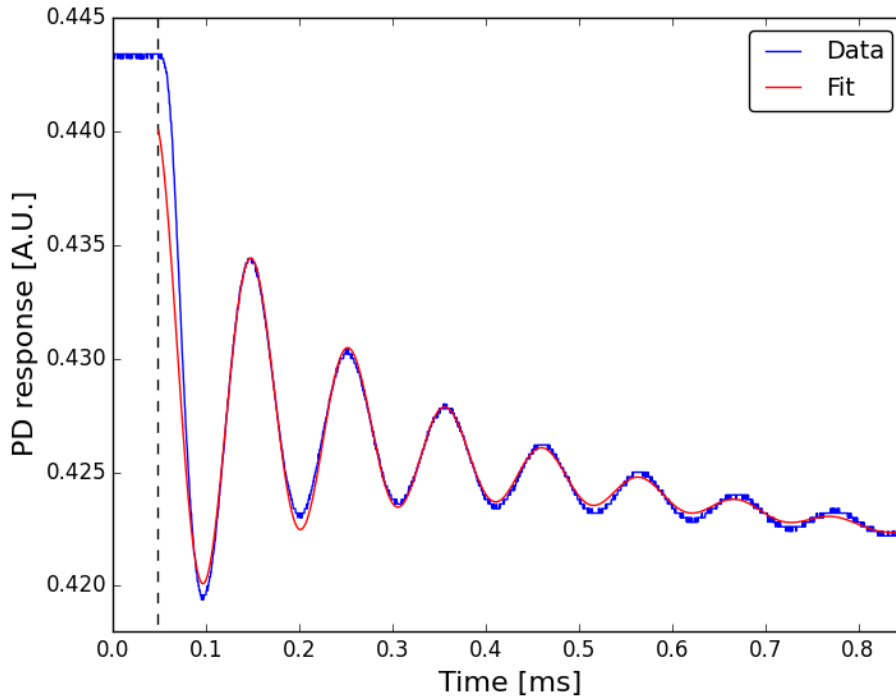


Figure 4.9: Measurement of Rabi oscillations “on-the-fly” in a ^{87}Rb vapor cell with a 75 Torr neon buffer gas. The blue line is the light intensity measured by the photodiode (PD, in Fig. 4.6) over time and the red line is the fit for the measured data of the form of Eq. 5.1.1. The experimental setup is shown in Fig. 4.6. The measurement is done as follows: a ~ 26 G DC magnetic field in the z direction is applied to the cell; 795 nm and 780 nm σ^- polarized beams pass through the vapor cell optically pumping the rubidium to the $|2, -2\rangle$ sub-level. A bandpass filter blocks the 780 nm beam, whereas the 795 nm beam propagates through the bandpass filter to the photodiode; RF radiation (with a magnetic field in the x direction) is applied to the cell, causing oscillations between the $|2, -2\rangle$ and the $|2, -1\rangle$ sub-levels. The difference between the absorption of the rubidium vapor sample in the two sub-levels, produces oscillations in the measured optical intensity of the 795 nm beam. The black dashed line indicates the time the RF is applied. Before the onset of the RF radiation most of the rubidium population is in the $|2, -2\rangle$ sub-level, which is a “dark state” for the 795 nm beam, and the vapor is transparent to that beam.

Data acquisition is done by triggering the scope at the onset of the RF pulse. Acquiring a full data set of Rabi oscillations “in one go” has some benefit: Rabi “on-the-fly” is less sensitive to drift of the lasers’ frequency and the signal can be averaged easily utilizing the averaging features of the scope.

4.4.3 Comparison between Rabi “in-the-dark” and Rabi “on-the-fly”

The Rabi “on-the-fly” measurement is faster, easier to perform, and less sensitive to a long time drift in the lasers’ frequencies. However, the main difference between these methods is that in the Rabi “in-the-dark” procedure the Rabi oscillations are induced in the presence of a single exciting field - the RF field, while in the Rabi “on-the-fly” three fields are present: the RF field and the two laser beams. Thus, only the Rabi “in-the-dark” method can be referred to as valid measurement of the $|2, -2\rangle$ to $|2, -1\rangle$ Rabi oscillations, and we need to validate the results of the Rabi “on-the-fly” method by a comparison with the results of the Rabi “in-the-dark” method.

5 Results: observing the Rabi “freeze”

Rabi oscillations (see Sec. 2.1) are a coherent phenomenon of a two-level system separated by $\hbar\omega_0$ and a near-resonance coupling field at a frequency $\omega \approx \omega_0$. It is typically characterized by the Rabi oscillations’ frequency and amplitude. The Rabi frequency is proportional to the amplitude of the coupling field and it goes up with the detuning $\delta = \omega - \omega_0$ of this field from resonance. On the other hand, the oscillations’ amplitude goes down with the detuning.

In this chapter we present Rabi oscillations between Zeeman sub-levels of a single hyperfine ground state of ^{87}Rb atoms contained in a vapor cell with a buffer gas. These Rabi oscillations are coherent; the oscillation frequency is proportional to the coupling field amplitude and the oscillation amplitude, as expected, decreases as the detuning of the coupling field from resonance increases. However, contrary to the theoretical expectations as noted above, the oscillation frequency does not increase with the detuning, and is totally independent of it. This is the Rabi “freeze”.

Our two-level system is realized by two neighboring Zeeman sublevels of the ^{87}Rb atom, $5^2\text{S}_{1/2}|2, -2\rangle$ (named hereafter $|2, -2\rangle$) and $5^2\text{S}_{1/2}|2, -1\rangle$ (named hereafter $|2, -1\rangle$) subjected to a ~ 26 G DC magnetic field. At this magnetic field the required frequency of the coupling RF field is $\omega/2\pi \sim 18.4$ MHz. We note that under these conditions we have an almost pure two-level system (see Sec. 4.2.1). The exact $|2, -2\rangle \leftrightarrow |2, -1\rangle$ transition frequency is measured by the scanning method presented in Sec. 4.3.

In Sec. 5.1 we review the fitting method we use to extract the Rabi frequency and amplitude from data sets such as those presented in Figs. 4.8 and 4.9. We then proceed to demonstrate this Rabi “freeze” in Sec. 5.2, 5.3 and 5.4 using ^{87}Rb vapor cells with a 75 Torr neon buffer gas, 7.5 Torr neon buffer gas and 60 Torr krypton buffer gas, respectively. In Sec. 5.5 we present results utilizing the $|2, 2\rangle \leftrightarrow |2, 1\rangle$, and in Sec. 5.6 we review the dependence of the Rabi frequency on the amplitude of the coupling field.

5.1 Fitting method

We characterize our experimental results of the Rabi population oscillations with the aid of an oscillating function that includes terms that account also for thermalization and decoherence. At the start of the oscillations ($t = 0$), all (or almost all) the population is in the $|2, -2\rangle$ Zeeman sub-level. Then several processes occur at once: the $|2, -2\rangle \leftrightarrow |2, -1\rangle$ Rabi oscillations start, and simultaneously we have thermal relaxation of the population from these two Zeeman sub-levels to the other 6 sub-levels. In addition, the amplitude of the oscillations decays due to dephasing of the coherence of the system (see Sec. 3.1).

The experimental results are fitted to:

$$f(t) = y_0 + ae^{-bt} + ce^{-dt}\sin(\tilde{\Omega}t + \phi), \quad [5.1.1]$$

where $t = 0$ is the onset of the RF field, $f(0) \approx y_0 + a$ is the initial relative population at $|2, -2\rangle$, b characterizes the thermal relaxation rate of the initial state $|2, -2\rangle$, c characterizes the oscillation amplitude (Eq. 2.1.16), d characterizes the dephasing rate, $\tilde{\Omega}$ is the generalized Rabi frequency (Eq. 2.1.15) and ϕ is the phase of the oscillations.

5.2 Results for vapor cell with a 75 Torr neon buffer gas

We conduct Rabi oscillations “in-the-dark” (Sec. 4.4.1) and “on-the-fly” (Sec. 4.4.2) on a ^{87}Rb vapor cell with a 75 Torr neon buffer gas. The ^{87}Rb vapor in this cell has a relaxation time of 30 ms (Tab. 3.1).

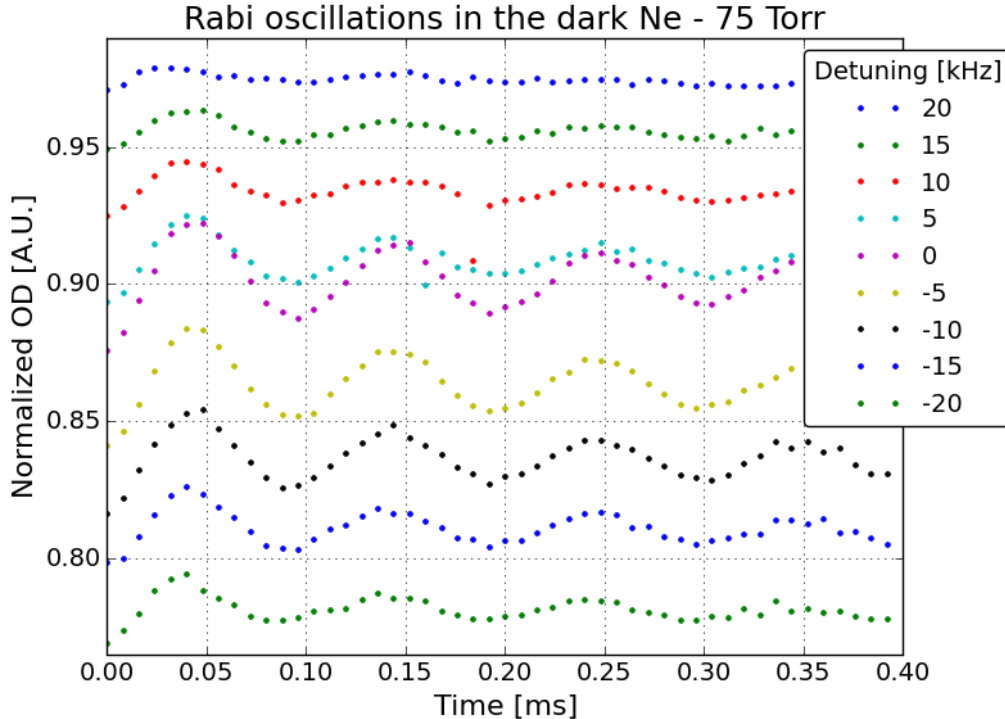


Figure 5.1: Experimental results of Rabi “in-the-dark” in a ^{87}Rb vapor cell with a 75 Torr neon buffer gas. Each set of dots in the same color represents a Rabi “in-the-dark” experiment (detailed in Sec. 4.4.1) with a different detuning value. An arbitrary shift is added to the optical density of every set to separate the sets from each other. The detuning values span from -20 kHz to 20 kHz, at 5 kHz intervals. Each of the data sets is fitted to a function of the form of Eq. 5.1.1. The generalized Rabi frequencies (see Eq. 2.1.15) and the Rabi amplitudes (see Eq. 2.1.16) of each of the Rabi “in-the-dark” data sets were extracted from the fits to the Rabi “in-the-dark” data. These data are presented in Fig. 5.3. The generalized Rabi frequency (extracted from the oscillations in the plot) for zero detuning is 9.9 ± 0.1 kHz. At a detuning of 20 kHz (twice the Rabi frequency) the generalized Rabi frequency of the oscillations should have been more than twice the Rabi frequency (~ 22 kHz, see Eq. 2.1.15). Clearly this is not the case: the oscillations frequency does not go up with the detuning. We name this phenomenon Rabi “freeze.”

The experimental results of Rabi oscillations “in-the-dark” in a ^{87}Rb vapor cell with a 75 Torr neon buffer gas at different detuning values are presented in Fig. 5.1 (the experimental procedure is described in Sec. 4.4.1). The sets of time resolved optical densities (Sec. 3.3) in different detuning values of the driving RF field are marked with different colors and are separated by adding some arbitrary OD shift to each set.

The first data set we present is taken with an RF frequency on resonance with the $|2, -2\rangle \leftrightarrow |2, -1\rangle$ transition. Then we modify the detuning at ± 5 kHz intervals until we cannot observe the oscillations. The results of the Rabi “in-the-dark” measurements in a ^{87}Rb vapor cell with a 75 Torr neon buffer gas are limited to a maximal detuning of ± 20 kHz. With higher detuning frequencies the oscillations are not visible.

To gain more information about the frequencies of the Rabi “in-the-dark” in a ^{87}Rb vapor cell with a 75 Torr neon buffer gas we perform a discrete Fourier transform (DFT). We apply a fast Fourier transform (FFT) algorithm [49] to each of the data sets. The results of the FFTs are shown in Fig. 5.2. An arbitrary value is added to the FFT amplitude of each of the data sets to separate them from each other. We clearly observe that the FFT of each of the data sets peaks at the same frequency.

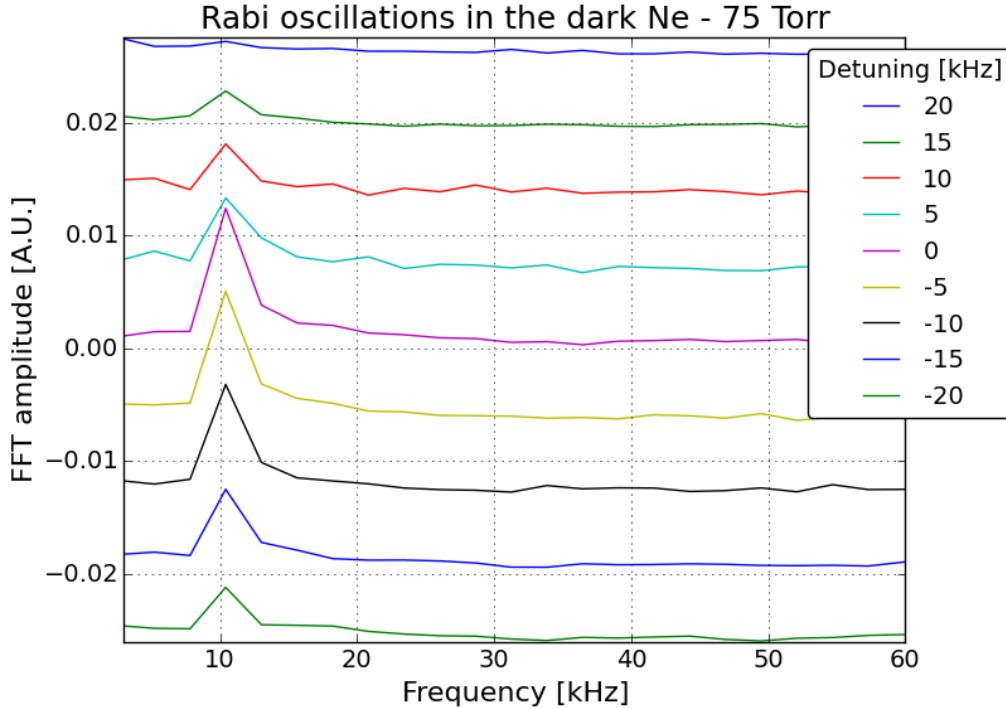


Figure 5.2: Fast Fourier transform (FFT) of the data obtained in the Rabi “in-the-dark” measurements (see Fig. 5.1). The data are measured in a ^{87}Rb vapor cell with a 75 Torr neon buffer gas with different detuning values that span from -20 kHz to 20 kHz, at 5 kHz intervals. An arbitrary shift is added to the FFT amplitude of every set to separate the sets from each other. The purpose of the FFT analysis is to extract the frequency profile of the Rabi oscillations for each detuning. Because of the relatively small amount of measured data points, the Fourier analysis is subject to large errors. However, the expected error is smaller than the expected peak shift (Eq. 2.1.15) for detunings above 10 kHz (see Fig. 5.3).

By comparing the data sets that are shown in Fig. 5.1 to the theoretical behavior of Rabi oscillations (see Fig. 2.1), we see that the oscillation frequency, the generalized Rabi frequency, does not change with the detuning as expected (Eq. 2.1.15). On the other hand, other parameters such as the oscillations amplitude (Eq. 2.1.16) and the relation between the coupling field amplitude and the Rabi frequency (discussed in Sec. 5.6) qualitatively behave as predicted by the theory.

Each of the data sets is fitted to a function of the form of Eq. 5.1.1. The frequency and the amplitude of each of the data sets are extracted from the fit and presented versus the detuning in Fig. 5.3. The frequencies (Eq. 2.1.15) and amplitudes (Eq. 2.1.16) are compared to the theoretical prediction. The oscillation frequency did not change with the detuning. The oscillation frequency was 9.9 kHz with a standard deviation of 0.1 kHz for all measured detuning values.

The results of the Rabi “on-the-fly” experiments of the ^{87}Rb vapor cell with a 75 Torr neon buffer gas are presented in Fig. 5.4. The experimental setup and sequence are described in Sec. 4.4.2.

The first data set of the Rabi “on-the-fly” measurements is taken with the RF frequency on resonance with the $|2, -2\rangle \leftrightarrow |2, -1\rangle$ transition. For the next step the detuning is changed at ± 5 kHz intervals until we cannot observe oscillations.

The Rabi “on-the-fly” measurement is less sensitive to fluctuations in the lasers’ frequency due to the short time that it takes to acquire the Rabi oscillations “on-the-fly” data. Hence, we can observe oscillation in a detuning value that reaches 25 kHz.

We apply a FFT on each of the Rabi “on-the-fly” data sets. The results of the FFTs are shown in Fig. 5.5. The FFT curves are smoother than in Fig. 5.2, due to 50 times more data points in the Rabi “on-the-fly” measurement. The frequency peaks are at the same place for all of the Rabi “on-the-fly” data sets; we have thus seen that the Rabi “freeze” occurs in the atomic transition $|2, -2\rangle \leftrightarrow |2, -1\rangle$ in two different Rabi oscillations measurements.

We fit each of the data sets that are presented in Fig. 5.6 to a function of the form of Eq. 5.1.1. The extracted generalized Rabi frequency and the Rabi amplitude are presented in Fig. 5.6. The corresponding error bars for the generalized Rabi frequencies and the Rabi amplitude have been omitted since they are very small due to the smoothness and large number of data points in the Rabi “on-the-fly” measurement.

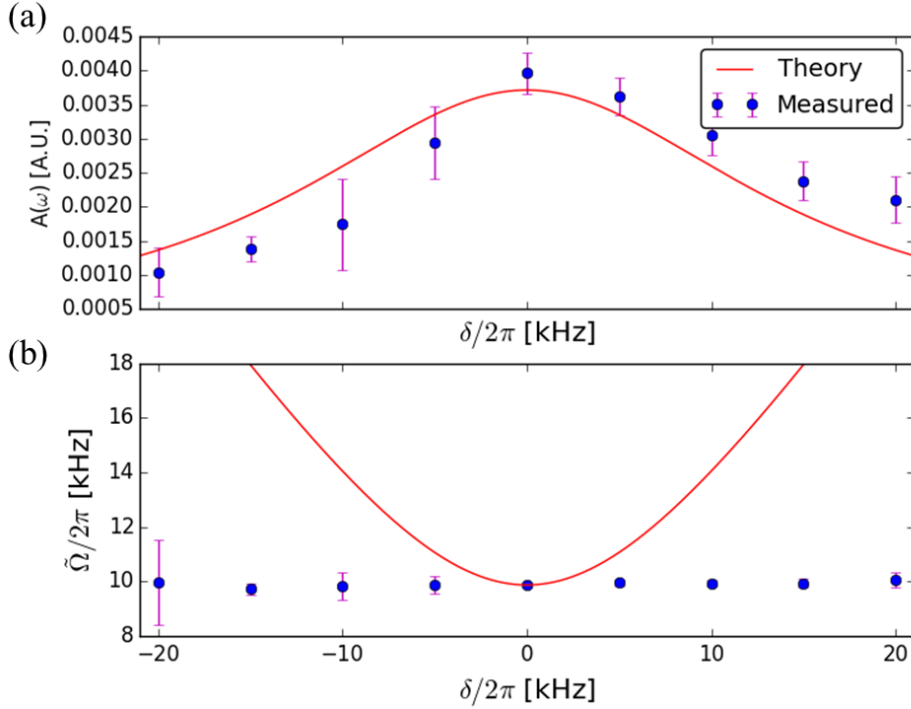


Figure 5.3: Rabi amplitude and generalized Rabi frequency. (a) Rabi amplitude versus detuning. The blue dots are the evaluation of the Rabi amplitude based on the Rabi “in-the-dark” measurements in a ^{87}Rb vapor cell with a 75 Torr neon buffer gas, (Fig. 5.1). The evaluation of the amplitude is done by fitting the measured data to a function of the form of Eq. 5.1.1. The parameter c of the fitted equation is the evaluated amplitude value. The red line is the calculated theoretical value of the Rabi amplitude as a function of the detuning, Eq. 2.1.16. (b) generalized Rabi frequency versus detuning. The blue dots are the evaluated oscillations frequencies $\tilde{\Omega}$ of the same data. The red line is the calculated generalized Rabi frequency as a function of the detuning (Eq. 2.1.15) for a given Rabi frequency, Eq. 2.1.7. The average of the measured generalized Rabi frequency is 9.9 kHz with a standard deviation of 0.1 kHz.

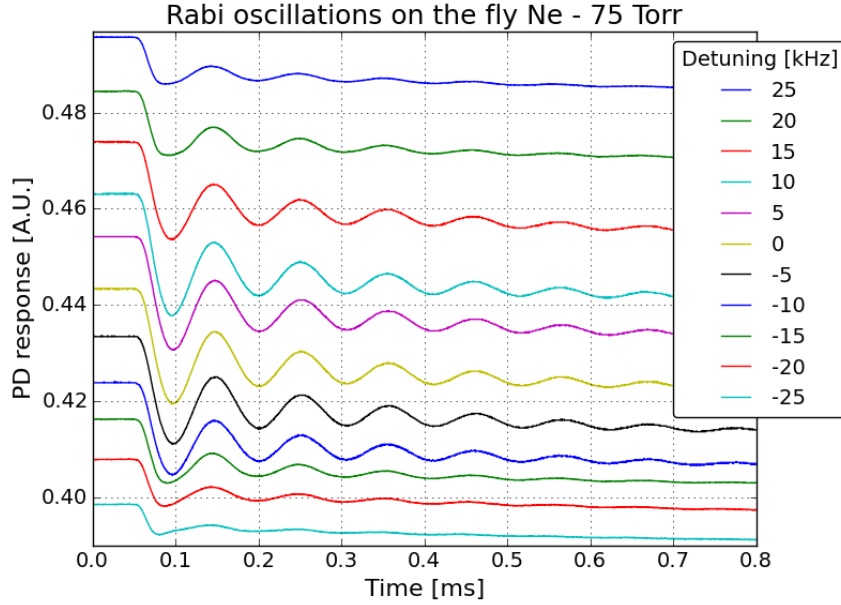


Figure 5.4: Experimental results of Rabi “on-the-fly” in a ^{87}Rb vapor cell with a 75 Torr neon buffer gas. Each line represents a Rabi “on-the-fly” experiment (detailed in Sec. 4.4.2) for different detuning values. An arbitrary shift is added to the PD response of every set to separate the sets from each other. The detuning spans from -25 kHz to 25 kHz, at 5 kHz intervals. Each of the measured data sets was fitted to the function of the form of Eq. 5.1.1. The generalized Rabi frequency (see Eq. 2.1.15) and the Rabi amplitude (see Eq. 2.1.16) of each of the Rabi “on-the-fly” plots, were extracted from the fits to the Rabi “on-the-fly” data, and are presented in Fig. 5.6.

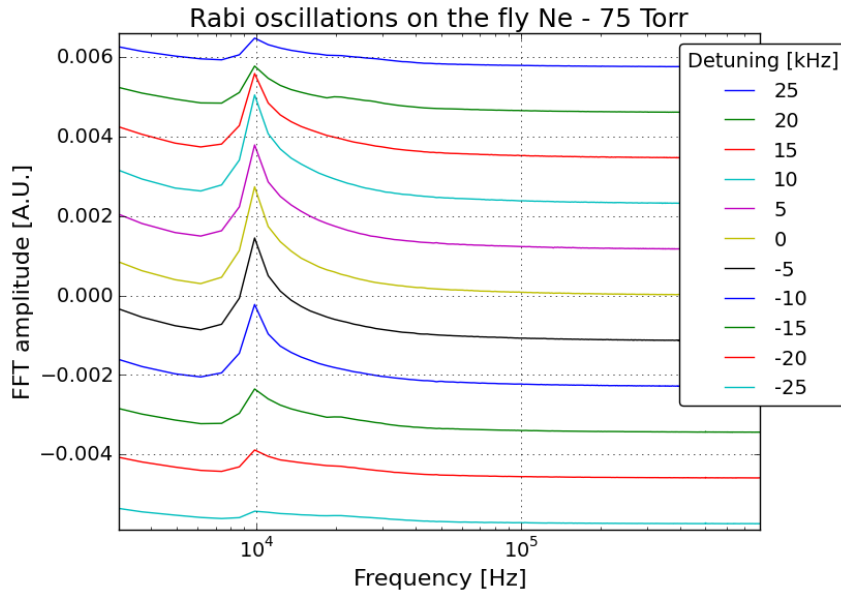


Figure 5.5: Fast Fourier transform (FFT) of the data obtained in Rabi “on-the-fly” measurements (see Fig. 5.4). The data are measured in a ^{87}Rb vapor cell with a 75 Torr neon buffer gas with various detuning values. An arbitrary shift is added to the FFT amplitude of every set to separate the sets from each other. Each line is an FFT of a Rabi “on-the-fly” measurement with a different detuning value that span from -25 kHz to 25 kHz, at 5 kHz intervals.

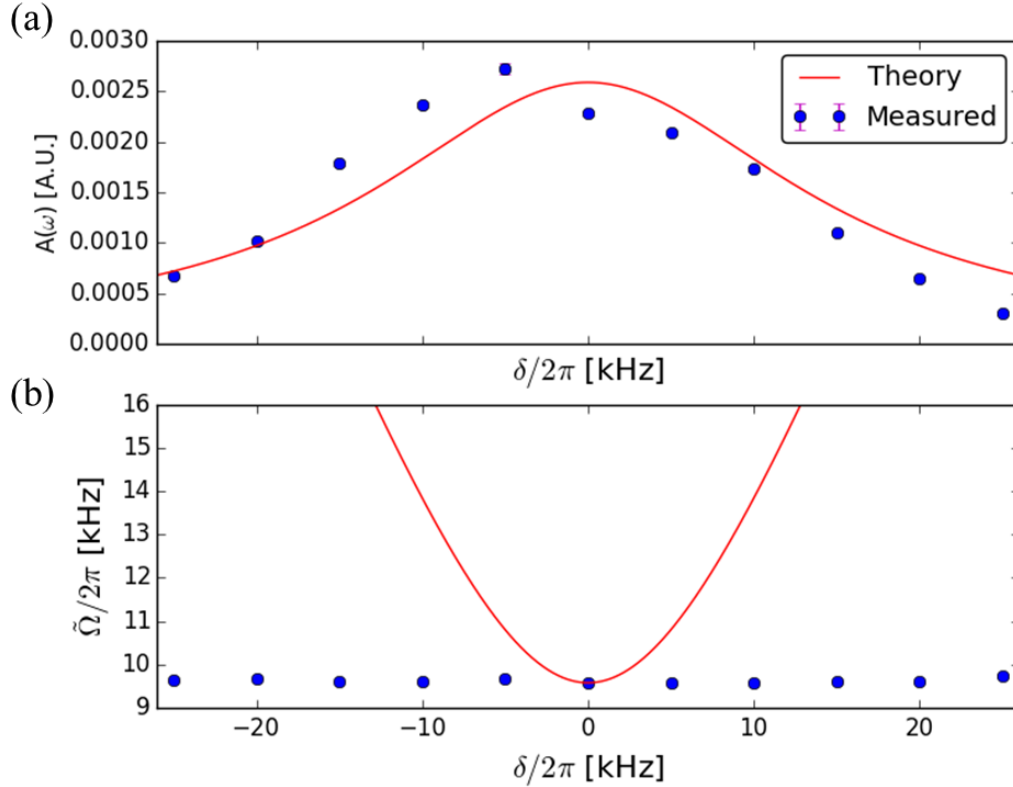


Figure 5.6: Rabi amplitude and generalized Rabi frequency. (a) Rabi amplitude versus detuning. The blue dots are the evaluation of Rabi amplitude based on Rabi “on-the-fly” measurements in ^{87}Rb vapor cell with a 75 Torr neon buffer gas (Fig. 5.4). The evaluation of the amplitude is done by fitting the measured data to a function of the form of Eq. 5.1.1. The parameter c of the fitted equation is the evaluated amplitude value. The red line is the calculated theoretical value of the Rabi amplitude for given detuning values, Eq. 2.1.16. (b) Generalized Rabi frequency versus detuning. The blue dots are the evaluated oscillation frequencies $\tilde{\Omega}$ of the same data. The red line is the calculated generalized Rabi frequency as a function of the detuning (Eq. 2.1.15) for given Rabi frequency, Eq. 2.1.7. The average of the measured generalized Rabi frequency is 9.6 kHz with a standard deviation of 0.05 kHz.

5.3 Results for vapor cell with a 7.5 Torr neon buffer gas

We repeat the experiments that are presented in Sec. 5.2 using a ^{87}Rb vapor cell with a 7.5 Torr neon buffer gas. Rabi “in-the-dark” (Sec. 4.4.1) experimental results are presented in Fig. 5.7

The results of the Rabi “in-the-dark” of the ^{87}Rb vapor cell with 7.5 Torr neon buffer gas are very similar to the results of the Rabi “in-the-dark” of the ^{87}Rb vapor cell with 75 Torr buffer gas. In the ± 20 kHz detuning range the oscillations in the 75 Torr neon buffer are more significant. This is due to a longer relaxation time of the 75 Torr cell (Tab 3.1) which gives rise to a smaller oscillation damping rate for the 75 Torr cell.

Fast Fourier transform is applied to the data from the 7.5 Torr neon buffer gas cell measurements.

The FFT of the Rabi “in-the-dark” data that are measured in a ^{87}Rb vapor cell with 7.5 Torr neon buffer gas (Fig. 5.8) is very similar to the FFT of the Rabi “in-the-dark” measurements in a cell with a 75 Torr neon buffer gas (Fig. 5.2).

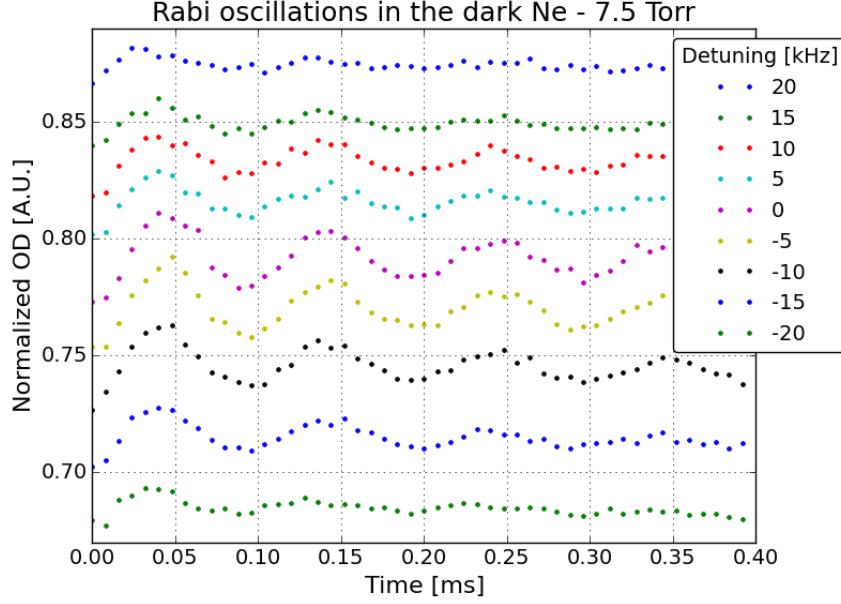


Figure 5.7: Experimental results of Rabi “in-the-dark” in a ^{87}Rb vapor cell with a 7.5 Torr neon buffer gas. Each set of dots in the same color represents a Rabi “in-the-dark” experiment (detailed in Sec. 4.4.1) with a different detuning value. An arbitrary shift is added to the optical density of every set to separate the sets from each other. The detuning values span from -20 kHz to 20 kHz, at 5 kHz intervals. Each of the data sets is fitted to a function of the form of Eq. 5.1.1. The generalized Rabi frequencies (see Eq. 2.1.15) and the Rabi amplitudes (see Eq. 2.1.16) of each of the Rabi “in-the-dark” data sets were extracted from the fits. These data are presented in Fig. 5.9. The generalized Rabi frequency (extracted from the oscillations in the plot) for zero detuning is 10.2 ± 0.1 kHz.

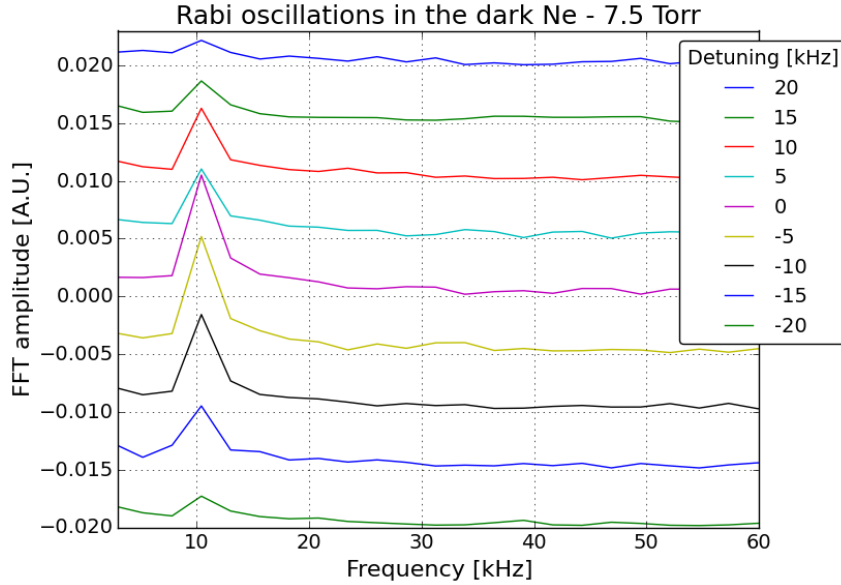


Figure 5.8: Fast Fourier transform (FFT) of the data obtained in the Rabi “in-the-dark” measurements (see Fig. 5.7). The data are measured in a ^{87}Rb vapor cell with a 7.5 Torr neon buffer gas with different detuning values that span from -20 kHz to 20 kHz, at 5 kHz intervals. An arbitrary shift is added to the FFT amplitude of every set to separate the sets from each other. The purpose of the FFT analysis is to extract the frequency profile of the Rabi oscillations for each detuning.

The generalized Rabi frequency and the Rabi amplitude of the Rabi “in-the-

dark” measurements in the ^{87}Rb vapor cell with 7.5 Torr neon buffer gas are shown in Fig. 5.9.

Rabi “on-the-fly” experimental results that are measured in the same ^{87}Rb 7.5 Torr neon vapor cell are presented in Fig. 5.10. (This experiment is conducted in the same way that is discussed in Sec. 4.4.2 and presented in Sec. 5.2).

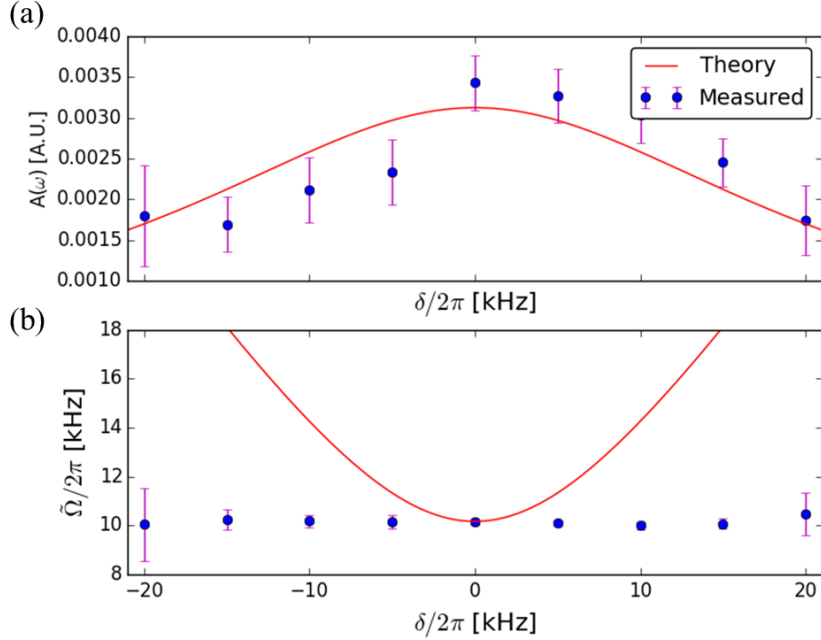


Figure 5.9: Rabi amplitude and generalized Rabi frequency. (a) Rabi amplitude versus detuning. The blue dots are the evaluation of the Rabi amplitude based on the Rabi “in-the-dark” measurements in a ^{87}Rb vapor cell with a 7.5 Torr neon buffer gas, (Fig. 5.7). The evaluation of the amplitude is done by fitting the measured data to a function of the form of Eq. 5.1.1. The parameter c of the fitted equation is the evaluated amplitude value. The red line is the calculated theoretical value of the Rabi amplitude as a function of detuning, Eq. 2.1.16. (b) generalized Rabi frequency versus detuning. The blue dots are the evaluated oscillations frequencies $\tilde{\Omega}$ of the same data. The red line is the calculated generalized Rabi frequency as a function of the detuning (Eq. 2.1.15) for a given Rabi frequency, Eq. 2.1.7. The average of the measured generalized Rabi frequency is 10.2 kHz with a standard deviation of 0.1 kHz.

We did not observe oscillations in the experimental results of Rabi “on-the-fly” in a ^{87}Rb vapor cell with a 7.5 Torr neon buffer gas for detuning values above ± 20 kHz, contrary to the Rabi “on-the-fly” results of the 75 Torr neon vapor cell (Fig. 5.4). This is due to a shorter relaxation time of the vapor hyperfine ground states (Sec. 3.1) in the 7.5 Torr neon vapor cell.

We applied a FFT to the Rabi “on-the-fly” data sets. The results of the FFT are shown in Fig. 5.11.

The generalized Rabi frequency and the Rabi amplitude of the ^{87}Rb 7.5 Torr neon vapor cell Rabi “on-the-fly” measurements that are shown in Fig. 5.12 are extracted from the fit to the Rabi “on-the-fly” experimental results (Fig. 5.10).

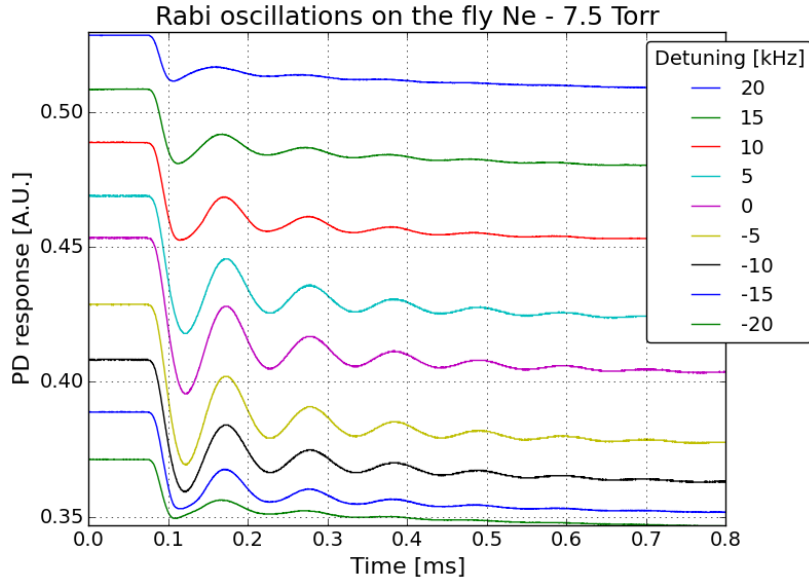


Figure 5.10: Experimental results of Rabi “on-the-fly” in a ^{87}Rb vapor cell with a 7.5 Torr neon buffer gas. Each line represents a Rabi “on-the-fly” experiment (detailed in Sec. 4.4.2) for different detuning values. An arbitrary shift is added to the PD response of every set to separate the sets from each other. The detuning spans from -20 kHz to 20 kHz, at 5 kHz intervals. Each of the measured data sets was fitted to a function of the form of Eq. 5.1.1. The generalized Rabi frequency (see Eq. 2.1.15) and the Rabi amplitude (see Eq. 2.1.16) of each of the Rabi “on-the-fly” plots, were extracted from the fits to the Rabi “on-the-fly” data, and are presented in Fig. 5.12. The oscillations are suppressed more rapidly compared to Rabi oscillations “on-the-fly” in the cell with a 75 Torr neon (Fig. 5.4). The high damping rate is due to a lower buffer gas pressure which gives rise to a relaxation time ~ 3 times shorter.

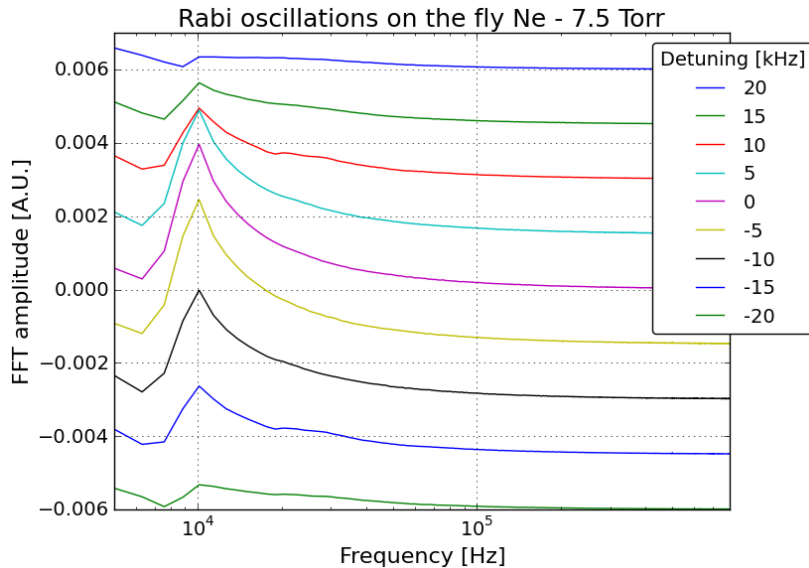


Figure 5.11: Fast Fourier transform (FFT) of the data obtained in Rabi “on-the-fly” measurements (see Fig. 5.10). The data are measured in a ^{87}Rb vapor cell with a 7.5 Torr neon buffer gas at various detuning values. An arbitrary shift is added to the FFT amplitude of every set to separate the sets from each other. Each line is an FFT of a Rabi “on-the-fly” measurement with a different detuning value that spans from -20 kHz to 20 kHz, at 5 kHz intervals.

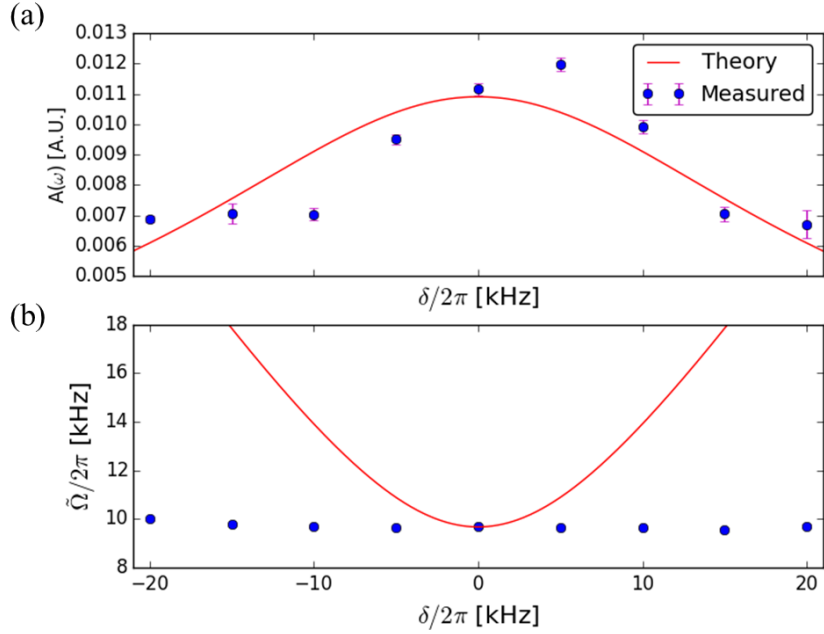


Figure 5.12: Rabi amplitude and generalized Rabi frequency. (a) Rabi amplitude versus detuning. The blue dots are the evaluation of the Rabi amplitude based on Rabi “on-the-fly” measurements in ^{87}Rb vapor cell with a 7.5 Torr neon buffer gas (Fig. 5.10). The evaluation of the amplitude is done by fitting the measured data to a function of the form of Eq. 5.1.1. The parameter c of the fitted equation is the evaluated amplitude value. The red line is the calculated theoretical value of the Rabi amplitude for given detuning values, Eq. 2.1.16. (b) generalized Rabi frequency versus detuning. The blue dots are the evaluated oscillations frequencies $\tilde{\Omega}$ of the same data. The red line is the calculated generalized Rabi frequency as a function of the detuning (Eq. 2.1.15) for a given Rabi frequency, Eq. 2.1.7. The average of the measured generalized Rabi frequency is 9.7 kHz with a standard deviation of 0.1 kHz.

The deviation of the Rabi amplitude from the theoretical curve is more significant in the measurements of the cell with 7.5 Torr neon (Fig. 5.12) than the deviation of the measurements of the cell with 75 Torr neon (Fig. 5.6). This is due to a longer relaxation time of the 75 Torr cell, which gives rise to a lower oscillation damping rate and higher oscillation amplitude for the 75 Torr cell.

5.4 Results for vapor cell with a 60 Torr krypton buffer gas

We repeat the experiments presented in Sec. 5.2 with a ^{87}Rb vapor cell with a 60 Torr krypton buffer gas.

The ^{87}Rb vapor cell with a 60 Torr krypton buffer gas has a significantly shorter relaxation time than the other two cells that we used in this work (Tab. 3.1). The short relaxation time gives rise to a low Rabi contrast, high oscillation damping rate, and overall a noisy and low quality Rabi oscillations measurement. Because of the high damping rate we cannot observe oscillations using the Rabi “in-the-dark” method for that cell. Rabi oscillations “on-the-fly” in a ^{87}Rb vapor cell with 60 Torr krypton buffer gas are shown in Fig. 5.13.

In the ^{87}Rb vapor cell with 60 Torr krypton buffer gas we, cannot observe oscillation for detuning values larger than ± 15 kHz. An FFT is applied to the data that are presented in Fig. 5.13. The FFT results are presented in Fig. 5.14.

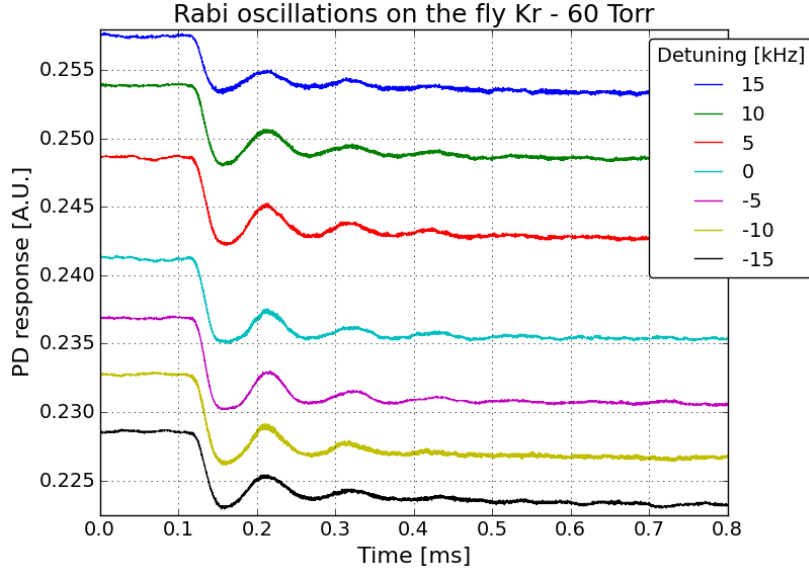


Figure 5.13: Experimental results of Rabi “on-the-fly” in a ^{87}Rb vapor cell with a 60 Torr krypton buffer gas. Each line represents a Rabi “on-the-fly” experiment (detailed in Sec. 4.4.2) for different detuning values. An arbitrary shift is added to the PD response of every set to separate the sets from each other. The detuning spans from -15 kHz to 15 kHz, at 5 kHz intervals. The short relaxation time (see Sec. 3.1) of a ^{87}Rb vapor cell with a 60 Torr krypton buffer gas (see Tab. 3.1) causes a high damping rate for the Rabi oscillations and a low Rabi contrast.

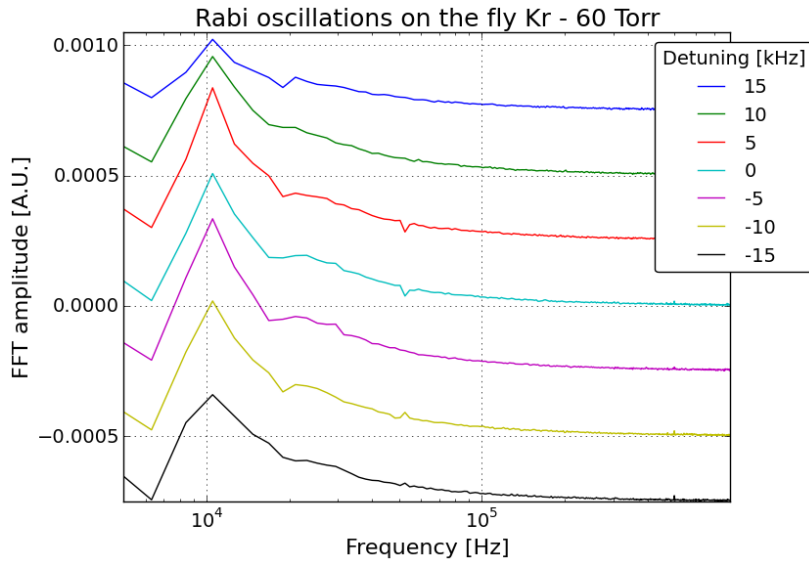


Figure 5.14: Fast Fourier transform (FFT) of the data obtained in Rabi “on-the-fly” measurements (see Fig. 5.13). The data are measured in a ^{87}Rb vapor cell with a 60 Torr krypton buffer gas with various detuning values. An arbitrary shift is added to the FFT amplitude of every set to separate the sets from each other. Each line is an FFT of a Rabi “on-the-fly” measurement with a different detuning value that spans from -15 kHz to 15 kHz, at 5 kHz intervals. The broadening in the frequency peak is due to the high rate of relaxation processes. Although the measurements are relatively noisy, the “freeze” of the generalized Rabi frequency is clearly observed.

Even though the Rabi oscillations in a ^{87}Rb vapor cell with a 60 Torr krypton buffer gas are characterized by low quality, the Rabi “freeze” appears from both the data (Fig. 5.13) and the FFTs of the data (Fig. 5.14).

5.5 Rabi oscillations utilizing the $|2, 2\rangle \leftrightarrow |2, 1\rangle$ transition

An additional straightforward experiment is to see if the Rabi “freeze” appears when we induce Rabi oscillations using the $|2, 2\rangle \leftrightarrow |2, 1\rangle$ transition. To adapt our system to the $|2, 2\rangle \leftrightarrow |2, 1\rangle$ transition, we need to either rotate the quarter-wave plate of the pump beams ($\lambda/4$ in Fig. 4.6) by $\pi/2$, or to reverse the direction of the ~ 26 G DC magnetic field. Each of these actions converts the pump beam’s polarization from σ^- to σ^+ . A summary of the results of this experiment is presented in Fig. 5.15. We conclude that the frequency “freeze” is observed in the same way for both the $|2, -2\rangle \leftrightarrow |2, -1\rangle$ and $|2, 2\rangle \leftrightarrow |2, 1\rangle$ transitions. It is worth noting that there is a difference in the transition frequencies due to the second order Zeeman shifts (due to the different values of m in Eq. 2.4.10 for each Zeeman sub-level). The frequency of the $|2, -2\rangle \leftrightarrow |2, -1\rangle$ transition for 26 G is 18.34 kHz and the frequency of the $|2, 2\rangle \leftrightarrow |2, 1\rangle$ transition is 18.04 kHz. The frequency difference between the $|2, \pm 2\rangle \leftrightarrow |2, \pm 1\rangle$ and the $|2, \pm 1\rangle \leftrightarrow |2, 0\rangle$ transitions is more than 95 kHz for both cases.

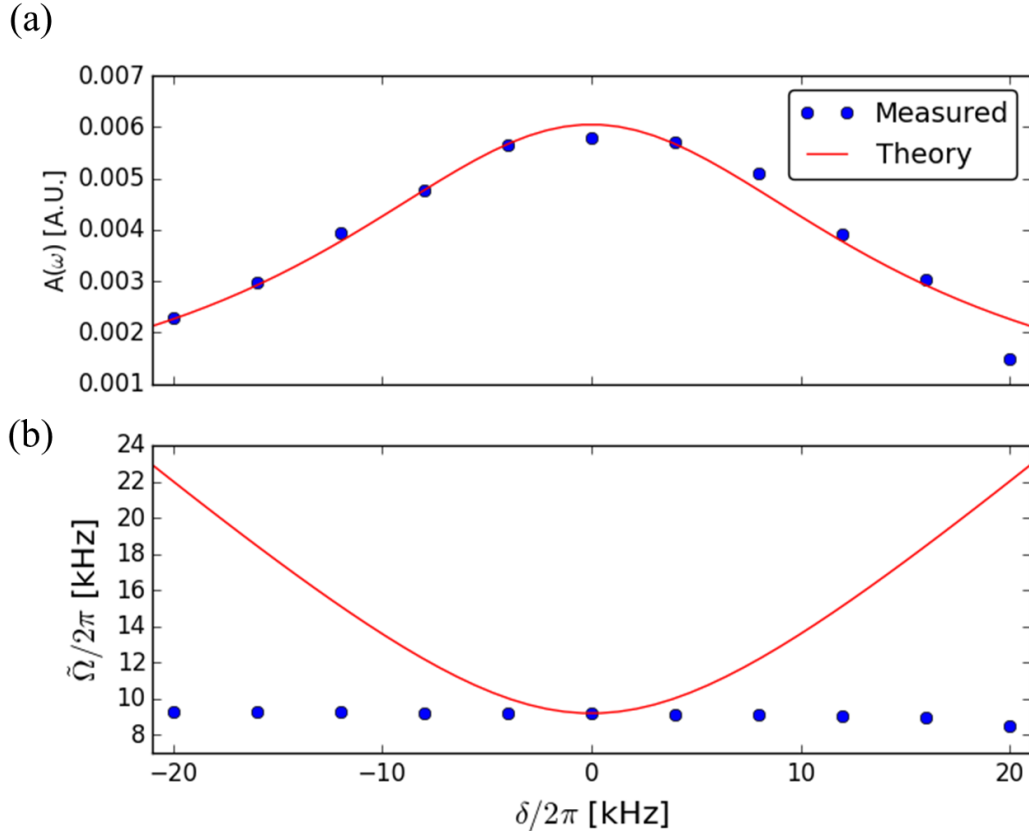


Figure 5.15: Rabi amplitude and generalized Rabi frequency of the $|2, 2\rangle \leftrightarrow |2, 1\rangle$ transition. The data are experimental results of Rabi “on-the-fly” in a ^{87}Rb vapor cell with a 75 Torr neon buffer gas. The detuning spans from -20 kHz to 20 kHz with 4 kHz intervals. The data are fitted to a function of the form of Eq. 5.1.1. (a) Rabi amplitude versus detuning. Each dot represents the Rabi amplitude from a Rabi “on-the-fly” experiment at a different detuning. The red line is the calculated Rabi amplitude (Eq. 2.1.16). (b) Generalized Rabi frequency versus detuning. Each dot represents the generalized Rabi frequency from a Rabi “on-the-fly” experiment at a different detuning. The red line is the calculated generalized Rabi frequency from Eq. 2.1.15. This experiment has been done to validate that the generalized Rabi frequency freeze is not a unique phenomenon of the $|2, -2\rangle \leftrightarrow |2, -1\rangle$ transition.

5.6 Dependence of the Rabi frequency on the coupling field amplitude

We have seen that the generalized Rabi frequency is independent of the detuning. It is interesting to check whether the Rabi frequency at zero detuning, Ω_R , is proportional to the amplitude of the coupling field as indicated by Eq. 2.1.7.

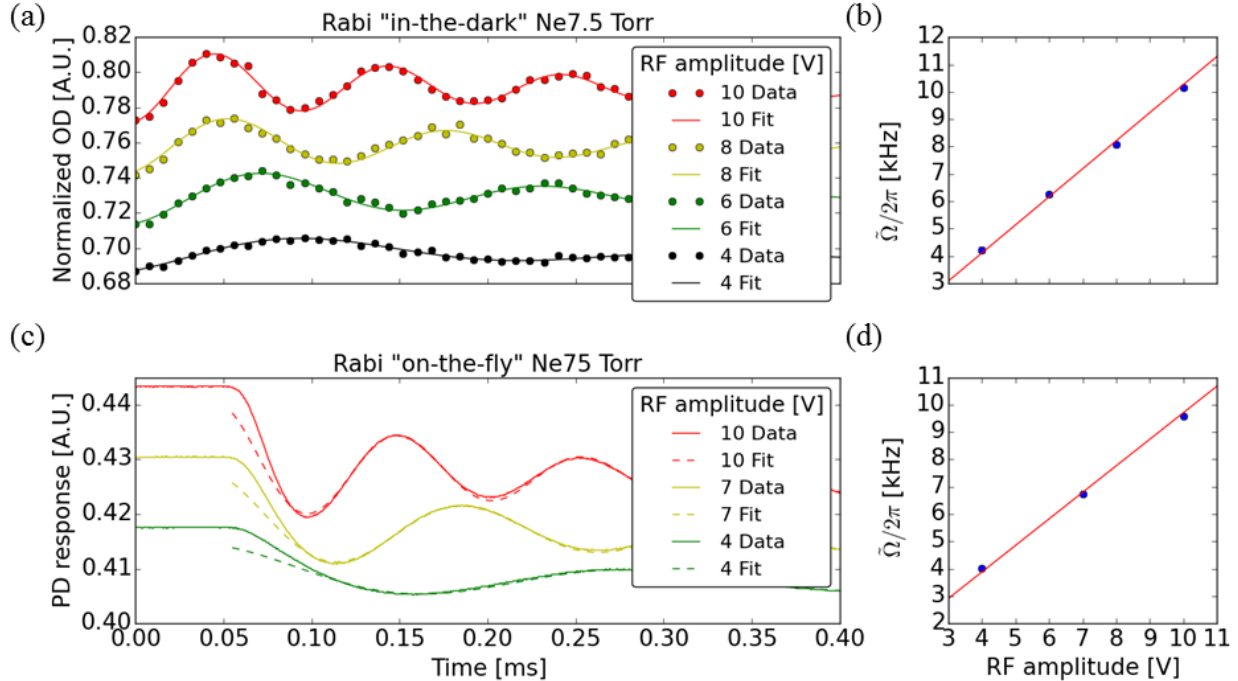


Figure 5.16: The generalized Rabi frequency of the $|2, -2\rangle \leftrightarrow |2, -1\rangle$ oscillations as a function of the amplitude of the driving RF field at the $|2, -2\rangle \leftrightarrow |2, -1\rangle$ transition resonance (zero detuning). (a) Rabi oscillations measured by the Rabi “in-the-dark” method (see Sec. 4.4.1) in a ^{87}Rb vapor cell with a 7.5 Torr neon buffer gas at several intensities of the driving RF field. Data are marked with circles, and are fitted to a function of the form of Eq. 5.1.1. The RF intensity (marked by colors) is indicated by the peak-to-peak voltage amplitude ($V_{\text{p-p}}$) setting of the RF signal generator. (Note: At a given frequency, the intensity of the RF field is proportional to the square of this amplitude). An arbitrary shift is added to the optical density of every set (color) to separate the sets from each other. (b) The blue dots indicate the generalized Rabi frequency [extracted from the data in (a), see Sec. 5.1] as a function of the amplitude of the RF signal generator; the red line is a linear fit. (c) Rabi oscillations measured by the Rabi “on-the-fly” method (see Sec. 4.4.2) in a ^{87}Rb vapor cell with a 75 Torr neon buffer gas at several intensities of the driving RF field. Data are marked with circles, and are fitted to a function of the form of Eq. 5.1.1. The RF intensity (marked by colors) is indicated by the peak-to-peak voltage amplitude ($V_{\text{p-p}}$) setting of the RF signal generator. An arbitrary shift is added to the PD response of every set from each other. (d) The blue dots indicate the generalized Rabi frequency [extracted from the data that shown in (b), see Sec. 5.1] as a function of the amplitude of the RF signal generator; the red line is a linear fit.

To this end, we recorded Rabi oscillations with both Rabi “in-the-dark” and Rabi “on-the-fly” methods as described in Sec. 4.4.1 and 4.4.2, using different amplitudes of the coupling RF field (at zero detuning) to drive the $|2, -2\rangle \leftrightarrow |2, -1\rangle$ transition. The RF generator provides an option to control directly the amplitude

of the generated output. The experimental results for both Rabi “on-the-fly” and Rabi “in-the-dark” (shown in Fig. 5.16) have a good fit with the theory. There is no frequency “freeze” related to the intensity of the coupling field.

6 Discussion

In the previous chapters we presented several results that indicate the existence of a coherent phenomenon of a two-level system - the Rabi “freeze”. To the best of our knowledge, such a “freeze” was not reported in the literature. Naturally, when we observed this new phenomenon, the first thought that came to mind was that there is some artifact in the experimental system that causes it.

If we wish to show that this phenomenon is not a result of an experimental artifact, our first task is to support the assumption that under a DC magnetic field of ~ 26 G the $|2, -2\rangle$ and $|2, -1\rangle$ (or the $|2, 2\rangle$ and $|2, 1\rangle$) Zeeman sub-levels of ^{87}Rb can be classified as a two-level system, and we can ignore transitions to other levels for at least $500 \mu\text{s}$ (a few Rabi cycles). To this end we have induced $|2, -2\rangle \leftrightarrow |2, -1\rangle$ Rabi oscillations in a cloud of ultracold ^{87}Rb atoms under similar conditions (see App. B). We show that for this system there is no “freeze”, which indicates that in the presence of a DC magnetic field of ~ 26 G the $|2, -2\rangle$ and $|2, -1\rangle$ Zeeman sub-levels of isolated atoms exhibit the normal behavior of a two-level system.

We also note that if the “freeze” was related to a significant transfer of atoms into other Zeeman sub-levels through the $|2, -1\rangle \leftrightarrow |2, 0\rangle$ transition (located 100 kHz below the $|2, -2\rangle \leftrightarrow |2, -1\rangle$ transition), or even through the two-photon $|2, -2\rangle \leftrightarrow |2, 0\rangle$ transition (50 kHz detuned photons, see Fig. 4.7), then there should have been a difference between red and blue detuning of the coupling radiation: red detuning of 20 kHz increases the coupling to the $|2, 0\rangle$ sub-level considerably, whereas blue detuning decreases that coupling. However, we do not observe any change of the “frozen” Rabi frequency with the detuning, either red or blue.

Very recently we started to check another possible experimental artifact. We are analyzing (Sec. 6.1) the influence of slight inhomogeneities of the DC magnetic field on the resulting Rabi oscillations. In parallel (Sec. 6.2) we try to investigate whether the high frequency collisions of the ^{87}Rb with the buffer gas atoms may be the physical origin of the “freeze”. Unfortunately, due to the limited time available for an M.Sc. project, a complete analyses of these two routes is beyond the scope of the work. However, in Ch. 7 we define further lines of both experimental and theoretical research into this interesting phenomenon.

6.1 The influence of a small magnetic inhomogeneity on Rabi oscillations

Let us assume that the value of the DC magnetic field in the cell is given by $B_z(\mathbf{r}) = B_z^{(0)} + \delta B_z(\mathbf{r})$, where $B_z^{(0)}$ is the value of the DC magnetic field in the center of the cell and $\delta B_z(\mathbf{r})$ represents the inhomogeneity of the magnitude of the field. (See axes definition in Fig. 4.4, 4.5, and 4.6). In the Rabi “on-the-fly” method (see Sec. 4.4.2) the measured signal is the absorption by atoms in the Zeeman sub-level $|2, -1\rangle$ integrated over the volume probed by the laser beam. Let us denote the density of atoms in $|2, -1\rangle$ by $n_{-1}(\mathbf{r})$. The absorption signal is given by

$$S = \int dx dy I(x, y) [1 - e^{-OD(x, y)}] \approx \sigma_0 \int d^3r n_{-1}(\mathbf{r}) I(\mathbf{r}), \quad [6.1.1]$$

where $I(\mathbf{r}) = I(x, y)$ is the intensity profile of the probe beam, $OD(x, y) = \sigma_0 \int dz n_{-1}(\mathbf{r})$ is the optical density and σ_0 is the scattering cross-section of the atom-light interaction. The non-uniform profile of the beam gives more weight in the signal to atoms near the center of the beam relative to atoms near the edge of the beam, where its intensity is smaller.

At a given position in the cell the number of atoms in the sub-level $|2, -1\rangle$ after a time t is expected to be

$$n_{-1}(\mathbf{r}) = n(\mathbf{r}) \frac{\Omega_R^2}{\tilde{\Omega}(\mathbf{r})^2} \sin^2[\tilde{\Omega}(\mathbf{r})t/2], \quad [6.1.2]$$

where $n(\mathbf{r})$ is the total density of atoms that was pumped initially into the sub-level $|2, -2\rangle$ before applying the RF pulse, and the generalized Rabi frequency is redefined (see Eq. 2.1.15) as:

$$\tilde{\Omega}(\mathbf{r}) = \sqrt{\Omega_R^2 + \delta(\mathbf{r})^2}, \quad [6.1.3]$$

with Ω_R being the Rabi frequency determined by the RF radiation (assumed here to be uniform over the cell) and $\delta(\mathbf{r}) = \omega_{\text{RF}} - |E_{-1}(\mathbf{r}) - E_{-2}(\mathbf{r})|/\hbar$ the position-dependent detuning, which is determined by the local value of the DC magnetic field.

The normalized signal can then be written as

$$P_1(t) = \int d\delta P(\delta) \frac{\Omega_R^2}{\tilde{\Omega}(\delta)^2} \sin^2[\tilde{\Omega}(\delta)t/2], \quad [6.1.4]$$

where

$$P(\delta) = \frac{\int d^3r n(\mathbf{r}) I(\mathbf{r}) \delta_D[\Delta - g_F \mu_B \delta B_z(\mathbf{r})/\hbar - \delta]}{\int d^3r n(\mathbf{r}) I(\mathbf{r})} \quad [6.1.5]$$

is the relative contribution of atoms with RF detuning δ to the signal. Here δ_D is the Dirac delta function [$\int d\delta \delta_D(\delta) = 1$], restricting the integral only to atoms at positions where $\Delta - g_F \mu_B \delta B_z(\mathbf{r}) = \delta$, and Δ is the RF detuning for an atom at a position where $B_z = B_z^{(0)}$ ($\delta B_z = 0$). For a specific RF radiation frequency, the contribution to the signal is quantified by a sum over all the atoms in a specific value of the magnetic field fluctuations $\delta B_z = (\Delta - \delta)\hbar/g_F \mu_B$, weighted by the local probe intensity which determines the contribution of an $|2, -1\rangle$ atom at this location to the absorption signal.

The relative contribution $P(\delta)$ therefore depends on three factors: the distribution of the magnetic field values in the cell, the profile of the probe beam and the density of atoms pumped initially to the Zeeman sub-level $|2, -2\rangle$. If we assume that $n(\mathbf{r})$ is constant we may imagine different configurations that would give rise to different distributions $P(\delta)$. For example, in the case of a small linear gradient along the cell $P(\delta)$ will not depend on the profile of the beam and will be limited by the values of the DC field at the edges of the cell with a constant probability for the values inside the cell. On the other hand, a gradient across the width of the cell or a non-linear gradient along the length of the cell would give rise to a smoothly varying distribution $P(\delta)$ which is not constant over the permitted values of the detuning.

As we don't really know the exact form of the magnetic field gradient in the cell, we can use a simple model for the relative contribution $P(\delta)$. Let us take a Gaussian profile with frequency width σ :

$$P(\delta) = \frac{1}{\sqrt{\pi}\sigma} \exp\left[-\frac{(\delta - \Delta)^2}{\sigma^2}\right]. \quad [6.1.6]$$

Once an atom is in the level $|2, -1\rangle$ it has the highest contribution to the signal when it is in the middle of the cell, where the local magnetic field is $B_z(\mathbf{r}) = B_z^{(0)}$ and the local RF detuning for a given RF frequency is $\delta(\mathbf{r}) = \Delta$, while its contribution drops when it is in the edge of the probe beam where the deviations δB_z of the field may be non-zero and hence $\delta(\mathbf{r}) \neq \Delta$. In addition, if the gradient of the

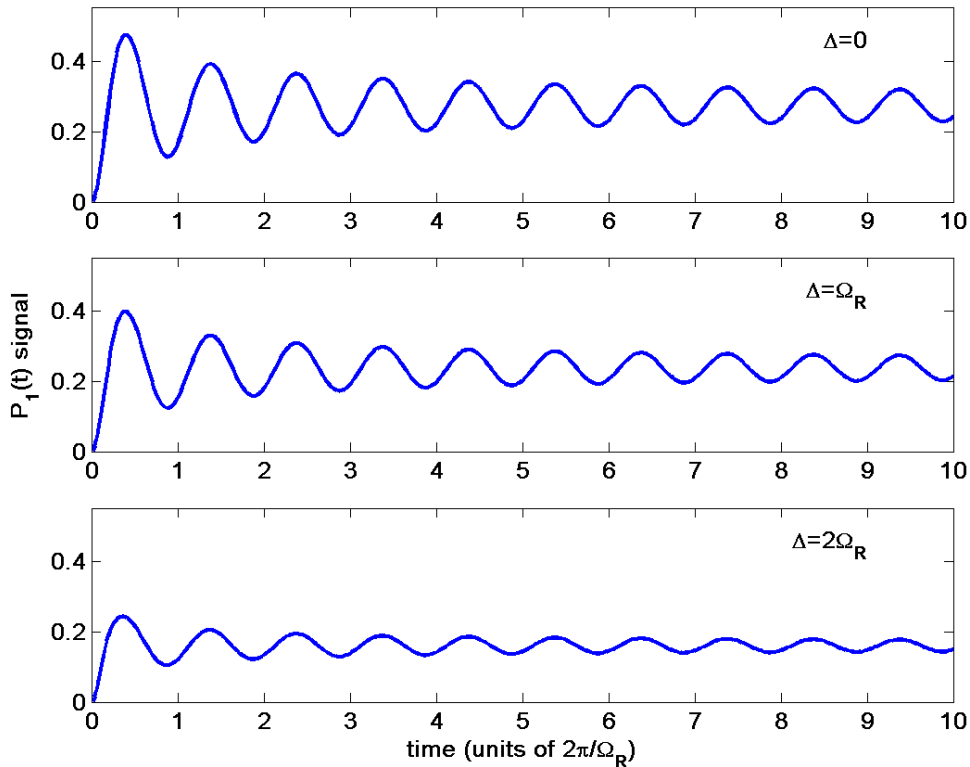


Figure 6.1: Simple simulation of the Rabi “freeze”. The population in the $|2, -1\rangle$ Zeeman sub-level $[P_1(t)]$ is presented as a function of time for three values of the detuning: $\Delta = 0, \Omega_R$ and $2\Omega_R$. It is seen that when the detuning Δ is increased (top to bottom) the amplitude of the oscillations reduces while the frequency of the oscillations remains almost constant.

magnetic field over the cell is not constant, then it is likely that there are more atoms in the central part of the cell where the magnetic field is close to $B^{(0)}$ and atoms that experience stronger deviations δB_z are a minority in the edges of the cell and therefore have a smaller contribution to the signal (once they are in $|2, -1\rangle$).

The Gaussian shape of $P(\delta)$ in Eq. 6.1.6, which is largest at $\delta = \Delta$ represents a combination of these two possible effects. The signal in Eq. 6.1.4 is an integral over the product of the probability for an atom to be in the state $|2, -1\rangle$ at time t and the contribution $P(\delta)$ of such a $|2, -1\rangle$ atom to the signal as modeled in Eq. 6.1.6.

In Fig. 6.1 we show an example of a calculation based on this simple model, where Eq. 6.1.4 was used to calculate the measured population of the $|2, -1\rangle$ sub-level as a function of time. Here $P(\delta)$ has the form of Eq. 6.1.6 with $\sigma = 2\Omega_R$. It is seen that when the detuning Δ is increased (top to bottom) the amplitude of the oscillations reduces while the frequency of the oscillations remains almost constant. Qualitatively, we see that small variations of the DC magnetic field across the cell, in combination with variation of the intensity profile of the measuring light, can produce a “freeze” of the oscillations’ frequency while the amplitude decreases as the detuning increases.

In App A we present data on $|1, 0\rangle \leftrightarrow |2, 0\rangle$ and $|1, -1\rangle \leftrightarrow |2, 1\rangle$ Rabi oscillations induced in ^{87}Rb vapor by a 6.8 GHz MW radiation (single photon) and by a coherent combination of 6.8 GHz and ~ 2 MHz radiation (two-photon transition). No Rabi “freeze” is observed in any of those experiments. A possible explanation may be related to the fact that all the Rabi oscillations described there were induced between pairs of levels that their transition frequency is independent (to the first order) of

the magnetic field. For example, inhomogeneity 0.01 G produces a shift of ~ 7 kHz in the $|2, -2\rangle \leftrightarrow |2, -1\rangle$ transition frequency, while it only shifts the $|1, 0\rangle \leftrightarrow |2, 0\rangle$ transition frequency by 0.01 Hz. Thus minor inhomogeneity of the magnetic field does not cause a change in the Rabi frequency of the type described above and does not produce a “freeze”.

However, we note here that the Rabi “freeze” was observed in three different vapor cells with different lengths (38 mm of the Ne 7.5 Torr, 40 mm of the Ne 75 Torr and 45 mm of the Kr 60 Torr). The oscillations were measured by two different methods: one method (Rabi “on-the-fly”, Sec. 4.4.2) uses a σ polarized light tuned to the $5^2S_{1/2}|F = 2\rangle \leftrightarrow 5^2P_{1/2}|F' = 2\rangle$ D_1 transition, at a DC magnetic field of ~ 26 G parallel to the beam’s propagation direction. The other (Rabi “in-the-dark” Sec. 4.4.1) uses a π polarized light tuned near the $5^2S_{1/2}|F = 2\rangle \leftrightarrow 5^2P_{3/2}|F' = 3\rangle$ D_2 transition and the DC magnetic field is now 1 G perpendicular to the beam’s propagation direction. The beams are expanded by a telescope to a diameter of about 25 mm, and then reduced by an iris to a diameter of 12 mm. The resulting spacial profile of the beams is somewhere between a flattop and a Gaussian, with some additional fluctuations. We also note that the set of coils producing the DC magnetic fields were reassembled and re-calibrated several times during the measurement of the Rabi oscillations in the different cells, so that the inhomogeneity of the magnetic field changes from time to time.

To verify that the Rabi “freeze” is caused only by the combined effect of the inhomogeneity of the DC magnetic field and of the intensity profile of the laser beams and possibly also variation in the intensity of the inducing RF radiation, one needs to show that we get both a complete “freeze” of the oscillations’ frequency and an almost Lorentzian variation of the amplitude for almost any type of inhomogeneity that is consistent with the measured experimental parameters. Due to the limited time we had, this has not been done yet.

6.2 A possible influence of collisions on the Rabi oscillations

Another possible idea that might explain the Rabi “freeze” comes from a comparison of the current results with previous experiments. The system that we use to induce (the $|2, 2\rangle \leftrightarrow |2, 1\rangle$ and the $|2, -2\rangle \leftrightarrow |2, -1\rangle$) Rabi oscillations with an ~ 18 MHz RF radiation was used in the past to induce both $|1, 0\rangle \leftrightarrow |2, 0\rangle$ and $|2, -1\rangle \leftrightarrow |2, 1\rangle$ Rabi oscillations with either a single 6.8 GHz (single photon transition) field or with a coherent combination of 6.8 GHz and ~ 2 MHz fields (two-photon transition). Details of these experiments are presented in App. A. No Rabi “freeze” was observed in these experiments. Although these experiments were performed several years ago, the Rabi oscillations were induced in the same cells we use now, and most of the experimental system has not been changed since that time.

Let us now summarize both current and previous data:

- When we induce Rabi oscillations in a ^{87}Rb vapor cell with a buffer gas where the frequency of the coupling field is ~ 18 MHz, we observe the Rabi “freeze” consistently using three different vapor cells, two different transitions ($|2, 2\rangle \leftrightarrow |2, 1\rangle$ and $|2, -2\rangle \leftrightarrow |2, -1\rangle$), various RF power levels and both measuring methods.
- When we induce Rabi oscillations in an ultracold ^{87}Rb cloud, under the same magnetic field and with the coupling field at the same frequency as those used on the ^{87}Rb vapor cell, we do not observe any Rabi “freeze” (see App. A).
- When we induce Rabi oscillations in a ^{87}Rb vapor cell with buffer gas where

the frequency of the coupling field is ~ 6.8 GHz, we do not observe any Rabi “freeze”.

When we combine these results with the information we have on the ^{87}Rb – vapor gas collision rate in our cells (between 50 M and 500 M collision per second, depending on the vapor gas type and pressure; see equation 4.15 in [50]), it seems reasonable to assume that the Rabi “freeze” may be related to these collisions: when the coupling field frequency is lower than the collision rate (*e.g.* ~ 18 MHz), Rabi “freeze” is observed; when the coupling field frequency is higher than the collision rate (*e.g.* ~ 6.8 GHz), there will be no freeze and the Rabi oscillations frequency will go up with the detuning as expected.

These collisions may be related to the appearance of the “freeze”, but up to now we were not able to suggest how this happens. However, we can suggest an experimental test for this “collision” hypothesis: The ^{87}Rb – vapor gas collision rate for the 7.5 Torr neon vapor cell is ~ 50 M/sec. Using a higher DC magnetic field (and thus higher $|2, -2\rangle \leftrightarrow |2, -1\rangle$ transition frequency), we can induce in this cell Rabi oscillations with a higher frequency RF field. Initial calculations show that with several modification to the system (a new solenoid and a new RF antenna) we can induce Rabi oscillation with an RF frequency as high as 150 MHz. This is three times higher than the collision rate. If indeed the “freeze” disappears at some frequency near the collision rate (~ 50 MHz), then we will have some experimental evidence to the “collision” hypothesis. Due to limited time I had for this project, I have not been able to modify the system and perform the suggested test, but my colleagues are doing that now.

Finally we wish to address the role that may be played by the value of $|m_F|$. All the Rabi oscillations described in App. A were induced between pairs of levels for which the transition frequency is independent (to first order) of the magnetic field (*i.e.* identical $|m_F|$ for the two states). Thus, minor inhomogeneities of the magnetic field would not cause a change in the Rabi frequency of the type described in Sec. 6.1 and would not produce a “freeze”. Hence, the results presented in App. A may also fit the hypothesis presented in Sec. 6.1. The value of $|m_F|$ may also give rise to a completely different speculation in the context of collisions. One may hypothesize that collisions give rise to the “freeze” only when the two states have a different $|m_F|$ such that the collisions may be able to “resolve” in which state the system is in. Such a speculation, if true, would then explain the absence of a “freeze” in the results presented in App. A.

7 Summary and outlook

In this work we experimentally study an unexpected observation of a “freeze” of the Rabi frequency: the frequency of Rabi oscillations induced between the Zeeman sub-levels of ^{87}Rb vapor does not increase with the detuning of the coupling field as theoretically expected. We show that we can prepare a two-level system, coupled with near-resonance ~ 18 MHz RF radiation, utilizing the ^{87}Rb $|2, -2\rangle \leftrightarrow |2, -1\rangle$ and the $|2, 2\rangle \leftrightarrow |2, 1\rangle$ transitions subjected to a DC magnetic field of ~ 26 G. We detail the experimental process of inducing Rabi oscillations utilizing two methods, Rabi “on-the-fly” and Rabi “in-the-dark”, and three different vapor cells: ^{87}Rb with neon at 7.5 Torr, ^{87}Rb with krypton at 60 Torr and ^{87}Rb with neon at 75 Torr. In all these experiments, we clearly observed Rabi oscillations; however, as noted, the oscillation frequency does not increase when the frequency of the inducing field is detuned from resonance: we have coined this effect Rabi “freeze”.

To investigate whether the observed phenomenon is due to an experimental artifact, our first task was to support the assumption that under a DC magnetic field of ~ 26 G the $|2, -2\rangle$ and $|2, -1\rangle$ (or the $|2, 2\rangle$ and $|2, 1\rangle$) Zeeman sub-levels of ^{87}Rb can be classified as a two-level system, and we can ignore transitions to other levels for at least $500 \mu\text{s}$ (few Rabi cycles). To this end we induced $|2, -2\rangle \leftrightarrow |2, -1\rangle$ Rabi oscillations in a cloud of ultracold ^{87}Rb atoms under similar conditions and showed that there is no “freeze”, namely, the system behaves as expected, indicating that under DC magnetic field of ~ 26 G the $|2, 2\rangle$ and $|2, 1\rangle$ Zeeman sub-levels can be classified as a two-level system.

We also note that if the “freeze” was related to a significant coupling of the $|2, -1\rangle \leftrightarrow |2, 0\rangle$ transition (located ~ 100 kHz below the $|2, -2\rangle$ and $|2, -1\rangle$ transition), then there should have been a difference between red and blue detuning of the coupling radiation: red detuning of 20 kHz increases the coupling to the $|2, 0\rangle$ sub-level considerably, whereas blue detuning decreases that coupling. However, we do not observe any change of the “frozen” Rabi frequency with the detuning, either red or blue.

In Sec. 6.1 we numerically investigated the possibility that experimental imperfections in the form of field inhomogeneities are responsible for the observed effect. While we were able to reproduce the effect, there is still much work to be done to verify that the very special conditions required to reproduce the effect are indeed present in the experiment.

In parallel, in Sec. 6.2 we speculate that there may be a more fundamental reason for the effect and suggest a possible source of the Rabi “freeze”: collisions with the buffer gas atoms. One possible hypothesis is that the “freeze” happens only when the collisions take place at a frequency higher than the frequency of the coupling field. While at this time we have no theoretical basis for such a speculation, we base this hypothesis on the fact that when the coupling frequency is in the range of 6.8 GHz, no “freeze” is observed in the same cells. To test the hypothesis that the ratio between the collision rate and the radiation frequency is relevant, the experimental system should be modified so that this hypothesis can be examined quantitatively as a function of a continuous variable. Specifically, the DC coils should be modified to produce a DC magnetic field of up to ~ 300 G, and the RF loops need to be modified so that they will be able to transmit RF radiation up to ~ 200 MHz. That is well above the collision rate in a ^{87}Rb vapor cell with 7.5 Torr neon buffer gas (50 M collision/sec). We would then be able to record Rabi oscillations with higher and higher coupling frequency and see if at some frequency of the coupling radiation the “freeze” disappears, and how this occurs. Another possible hypothesis is that the value of $|m_F|$ of the two levels is somehow relevant. For example, the tests done

at 6.8 GHz, and which produced no “freeze”, had the same $|m_F|$ for both states. It would thus be interesting to check the transition $|2, 2\rangle \leftrightarrow |1, 1\rangle$.

To conclude, we have observed an unexpected effect that may be due to experimental imperfections or to fundamental physics. I have collected a considerable amount of data related to this phenomenon, but unfortunately, the limited time of the M.Sc. project did not enable me to reach a final conclusion. My colleagues and I are in the process of testing both avenues.

Appendices

Appendix A

Rabi oscillations in ^{87}Rb vapor cells induced by a 6.8 GHz coupling field

The experimental system described in Ch. 4 was used to induce Rabi oscillations between other sub-levels of ^{87}Rb atoms, such as $|1, 0\rangle \leftrightarrow |2, 0\rangle$, where the resonance frequency is in the microwave (MW) domain of ~ 6.8 GHz. Regarding the system used for these experiments (for clarity we call this “MW system”), which were conducted several years ago, we wish to note that the vapor cells, probe laser, and magnetic field coils were the same or very similar to those used to investigate the Rabi freeze, while the experiments were conducted using the Rabi “in-the-dark” method (see Sec. 4.4.1). The main differences between these experiments are that a MW patch antenna on a printed circuit board ($5\text{ cm} \times 5\text{ cm} \times 3\text{ mm}$) is located 5 cm above the vapor cell and that the RF loops (Fig. 4.5) were not installed; rather, a coil parallel to the z axis was used to transmit RF radiation when required.

In the first experiment we wish to review, a coupling field at ~ 6.8 GHz induces $|2, 0\rangle \leftrightarrow |1, 0\rangle$ Rabi oscillations [41]. The experiment uses a ^{87}Rb vapor cell with 7.5 Torr neon buffer gas, the probe laser is tuned to the $5^2\text{S}_{1/2}|F = 2\rangle \leftrightarrow 5^2\text{P}_{3/2}|F' = 3\rangle$ transition, a set of compensation coils is tuned to cancel earth’s magnetic field to below 50 mG, and a flat 10×10 mm copper MW antenna is located 5 mm above the cell.

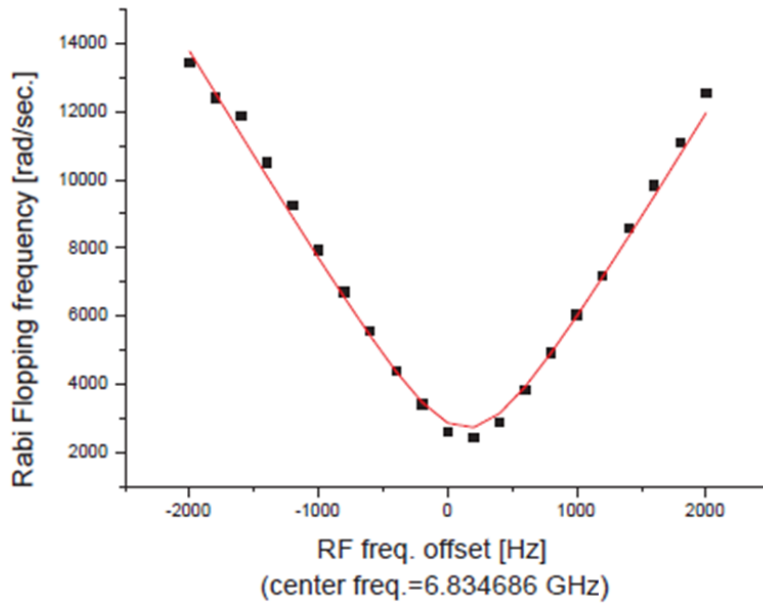


Figure A.1: Generalized Rabi frequency versus the detuning. Rabi oscillations are conducted between $|1, 0\rangle$ and $|2, 0\rangle$ Zeeman sub-levels, driven by an external MW field. The two states are coupled by a single-photon transition. The total external DC magnetic field is set to less than 0.05 G by the compensation coils. The red line is a fit to a function of the form of Eq. 2.1.15. This experiment was conducted with the same experimental system and using the same ^{87}Rb vapor cell with 7.5 Torr neon buffer gas as used in our work. These data were measured by Dr. Amir Waxman (see [41]).

The experiment is conducted as follows: the probe laser is turned on and optically pumps the population for $100\ \mu\text{s}$, which drives all of the population to the $F = 1$ hyperfine state; a MW pulse is applied for a time t , driving $|1, 0\rangle \leftrightarrow |2, 0\rangle$ Rabi

oscillations; the probe beam is turned on again and we measure p_2 , the population in $F = 2$, as described in Sec. 4.2.2. This process is repeated for different times t to provide a plot of p_2 versus t . Since the probe beam was not tuned to the magic frequency, there may be some error in the population measurement, but the Rabi oscillations are clearly visible and their frequency can be extracted easily.

The generalized Rabi frequency for each set of measurements with different detuning values of the MW field is extracted by fitting each of the data sets to an oscillating function of the form of Eq. 5.1.1. The generalized Rabi frequencies versus the detuning are shown in Fig. A.1. Contrary to the “freeze” phenomenon in Rabi oscillations between the $|2, -2\rangle \leftrightarrow |2, -1\rangle$ Zeeman sub-levels, the Rabi oscillations between the $|1, 0\rangle \leftrightarrow |2, 0\rangle$ Zeeman sub-levels are well described by the theory of Eq. 2.1.15.

Other two-level systems that have been studied are the “clock” [$|1, 0\rangle \leftrightarrow |2, 0\rangle$, see Fig. A.2 (a)] and the “qubit” [$|1, -1\rangle \leftrightarrow |2, 1\rangle$, see Fig. A.2 (b)] transitions [51]. Both are two-photon Raman transitions. The experimental setup for such systems consists of the probe laser tuned to the $5^2S_{1/2}|F = 2\rangle \leftrightarrow 5^2P_{3/2}|F' = 3\rangle$ transition, Helmholtz compensation coils that cancel earth’s magnetic field, a DC z coil, a flat 10×10 mm copper MW antenna printed on a 50×50 mm PCB located 5 mm above the cell, and an RF coil producing an RF magnetic field along the cell’s axis.

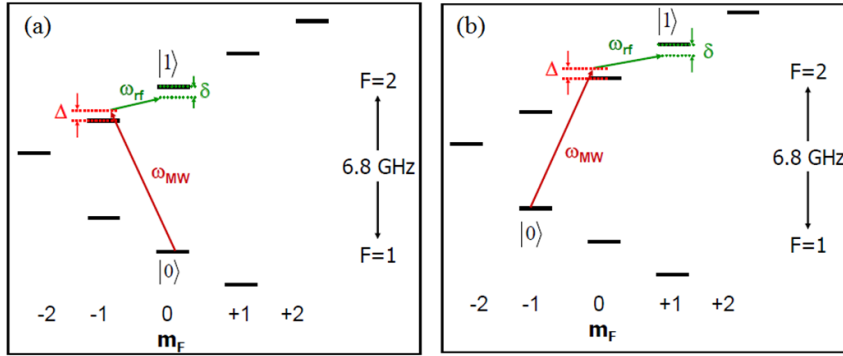


Figure A.2: Two-photon transition diagram. Level structure diagrams for two-photon transitions between sub-levels of the ground state of ^{87}Rb (see Fig. A.3). The transition is induced by two fields: the MW field and the RF field. Δ represents the detuning of the MW frequency from an intermediate transition, and δ represents the detuning of the sum of the frequencies, MW and RF, from the total transition frequency of the two-photon transition. (a) The clock transition. The intermediate transition is $|1, 0\rangle \leftrightarrow |2, -1\rangle$ and the total transition is $|1, 0\rangle \leftrightarrow |2, 0\rangle$. (b) The qubit transition. The intermediate transition is $|1, -1\rangle \leftrightarrow |2, 0\rangle$ and the total transition is $|1, -1\rangle \leftrightarrow |2, 1\rangle$. This figure is taken from Dr. Gal Aviv’s thesis [51].

The clock transition [Fig. A.2 (a)] is realized in the ^{87}Rb vapor cell with 7.5 Torr neon buffer gas. The Rabi oscillations are induced by two coherent fields: a MW field detuned by Δ from the $|1, 0\rangle \leftrightarrow |2, -1\rangle$ transition, and an RF field with a frequency equal to the $|1, 0\rangle \leftrightarrow |2, 0\rangle$ transition frequency minus the MW frequency and minus the detuning δ . Thus, the $|1, 0\rangle \leftrightarrow |2, 0\rangle$ two-photon transition proceeds via the intermediate level $|2, -1\rangle$. The DC magnetic field is 0.5 G in the z direction and it generates a 350 kHz frequency difference between neighboring Zeeman sub-levels. Similarly, the two-photon qubit transition from $|1, -1\rangle$ to $|2, 1\rangle$ proceeds via the intermediate level $|2, 0\rangle$. In this case, the DC magnetic field is 3.23 G in the z direction, which generates a 2.24 MHz frequency difference between neighboring Zeeman sub-levels.

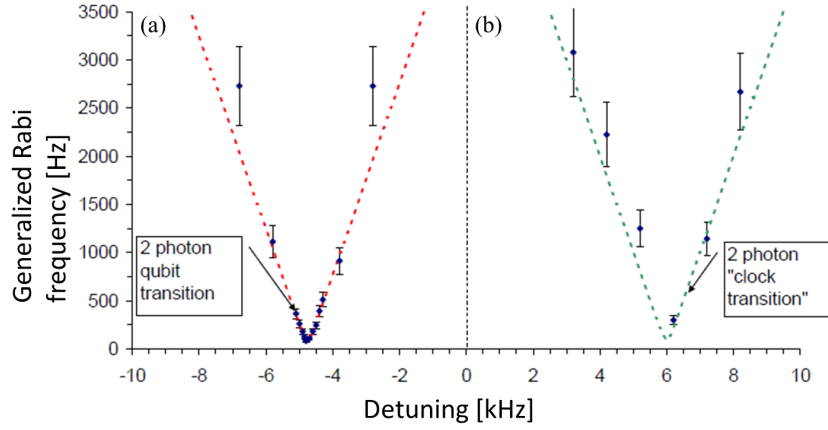


Figure A.3: Generalized Rabi frequency mapping for two-photon transitions versus detuning δ (see Fig. A.2). The dashed lines are fits to the measured generalized Rabi frequency using the form of Eq. 2.1.15. (a) The qubit transition [see Fig. A.2 (b)] is performed using a ^{87}Rb vapor cell with 75 Torr neon buffer gas. A magnetic field of 3.23 G generates a separation of 2.24 MHz between the Zeeman sub-levels. The MW and the RF fields are tuned so that the intermediate detuning is $\Delta = 134$ kHz. (b) Analogous to (a) but for the clock transition [see Fig. Fig. A.2 (a)] with $\Delta = 100$ kHz. A DC magnetic field of 0.5 G generates a separation of 350 kHz between the Zeeman sub-levels. These Rabi oscillations experiments were conducted with the same experimental system and using the same ^{87}Rb vapor cells as those in our work. These data were measured by Dr. Gal Aviv (see [51]).

These two-photon experiments are conducted in a manner similar to those described above for the $|1, 0\rangle \leftrightarrow |2, 0\rangle$ single-photon transition except that here we use coherent MW and RF fields (with frequencies as shown in Fig. A.2). The results are summarized in Fig. A.3 and are again well described by the theory of Eq. 2.1.15

Appendix B

Rabi oscillations in the $|2, 2\rangle \leftrightarrow |2, 1\rangle$ transition in ultracold atoms

In addition to experiments using room-temperature gas cells, other experiments conducted in our research group use ultracold ^{87}Rb atoms (typically at temperatures in the μK range). Such an extremely low temperature makes such a system useful for high-precision measurements. Hence, ultracold ^{87}Rb atoms can be utilized for measurements of coherent transitions with a long lifetime, high coherence, and low noise levels.

Such a system enables conducting Rabi oscillations between the Zeeman sub-levels of ^{87}Rb without buffer gas, with the same external field that we apply to our vapor cells. We are interested in exploiting this advantage, since room-temperature vapor cells without buffer gas have a relaxation time of around $50\ \mu\text{s}$, which is about half of the maximal Rabi oscillation period that we can produce in our system.

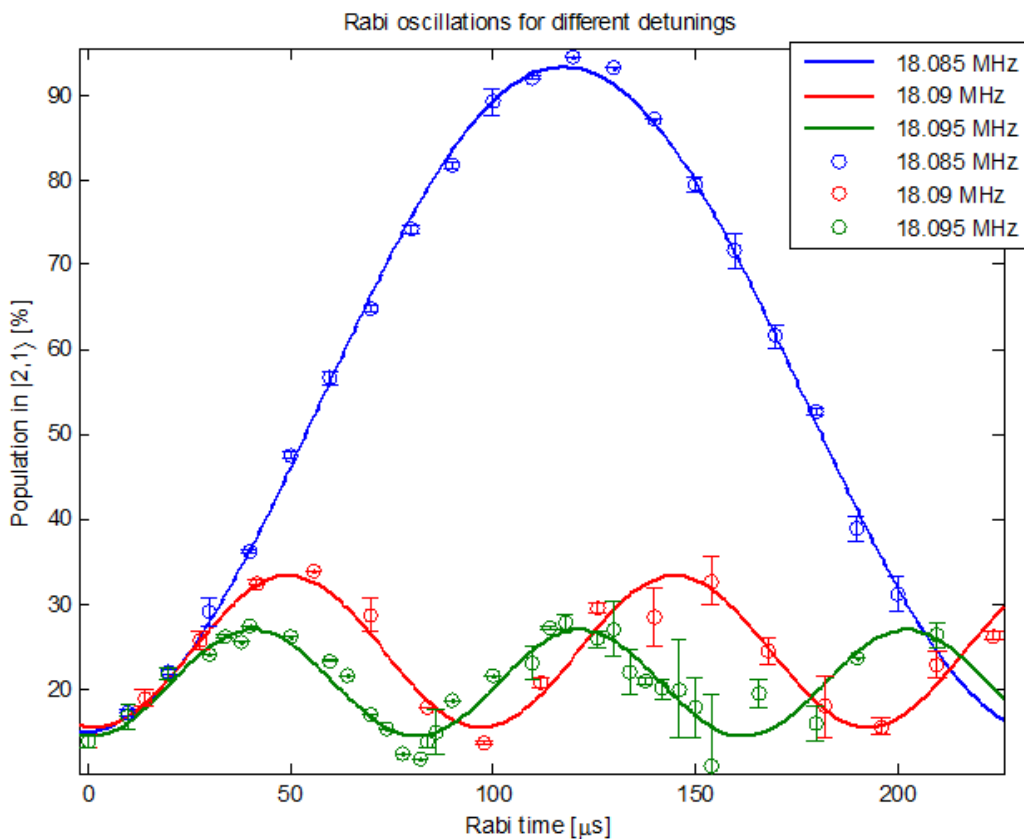


Figure B.1: Rabi oscillations for freely-falling ultracold ^{87}Rb atoms. The ultracold ^{87}Rb atoms were optically pumped to the $|2, 2\rangle$ Zeeman sub-level of the ground state, magnetically trapped, evaporatively cooled to quantum degeneracy, and then released from the trap. A DC magnetic field of $\sim 26\ \text{G}$ and RF radiation at $\sim 18\ \text{MHz}$ induces $|2, 2\rangle \leftrightarrow |2, 1\rangle$ Rabi oscillations for a time t , followed by a measurement of the $|2, 1\rangle$ population normalized to that of the $|2, 2\rangle$ state (see text). The results are plotted vs. time (open circles). In the figure we present plots for three RF frequencies: 18.085 MHz, 18.090 MHz, and 18.095 MHz. A sine function (solid lines) was fitted to each of measurements series to estimate the generalized Rabi frequency.

Rabi oscillations were induced between the $|2, 2\rangle$ and $|2, 1\rangle$ Zeeman sub-levels of ultracold freely-falling ^{87}Rb atoms. Here are the details of this experiment:

using the setup described in [52], an RF field induces transitions from the $|2, 2\rangle$ Zeeman sub-level to the $|2, 1\rangle$ Zeeman sub-level of a Bose-Einstein condensate (BEC) of $\sim 10^4$ atoms. In order for the $|2, 1\rangle$ and $|2, 2\rangle$ Zeeman sub-levels to form a pure two-level system, we apply a 26 G homogeneous magnetic field such that $\Delta E_{|2,2\rangle \leftrightarrow |2,1\rangle} \approx 18$ MHz and the transition to the $|2, 0\rangle$ Zeeman sub-level is pushed out of resonance by ~ 100 kHz via the non-linear Zeeman effect (Eq. 2.4.10). (The atoms are initially trapped at a distance of $z = 100 \mu\text{m}$ from the atom chip surface [53].) Then the ultracold ^{87}Rb atoms were released and a 18 MHz Rabi pulse was applied for a time T_R . A magnetic gradient, generated by a short current pulse in a copper wire below the chip surface, is applied to spatially separate the atoms according to their Zeeman sub-levels via the Stern-Gerlach effect. Finally, to measure the population transfer, the atoms were imaged using absorption imaging and the resulting number of atoms in each atomic cloud was counted, corresponding to each Zeeman sub-level. The homogeneous magnetic field is kept on during the free-fall to preserve the quantization axis.

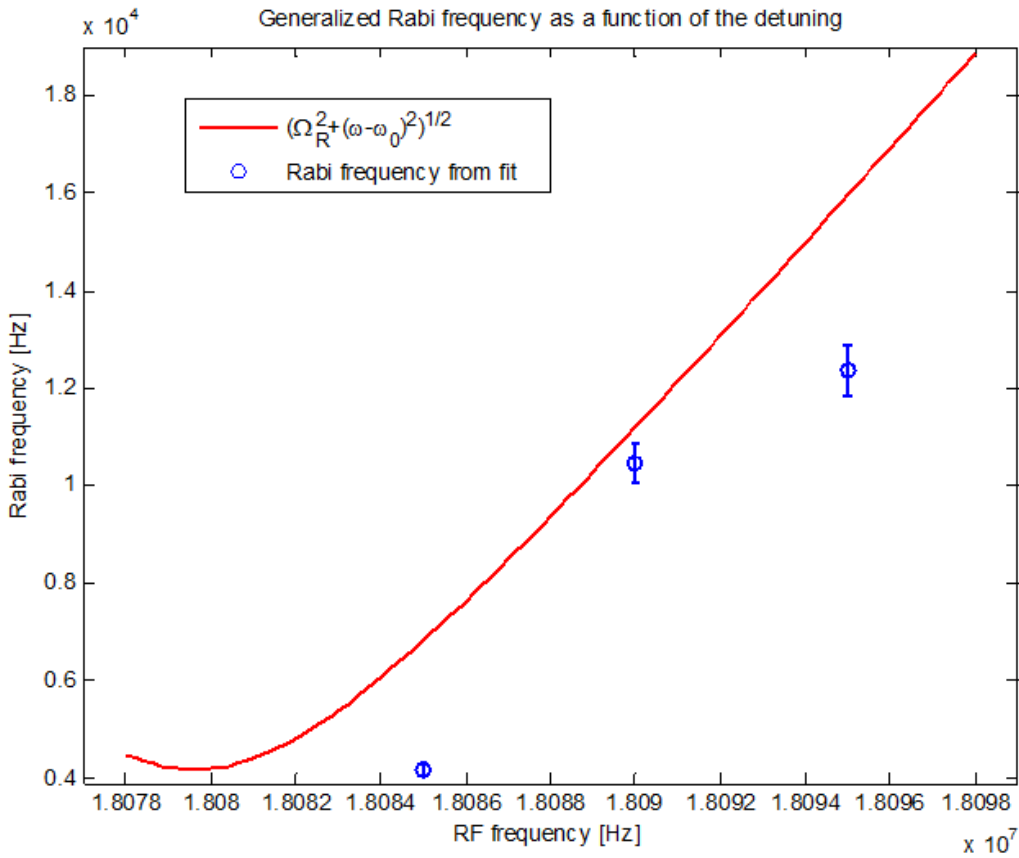


Figure B.2: Generalized Rabi frequency of $|2, 2\rangle \leftrightarrow |2, 1\rangle$ oscillations (open circles) induced in a cloud of ultracold ^{87}Rb atoms (Fig. B.1) as a function of the RF frequency. The generalized Rabi frequency is estimated as described in the caption of Fig. B.1. Also plotted (solid line) is the theoretical prediction. Clearly, the generalized Rabi frequency increases as the RF frequency is detuned further from resonance. There is no “freeze.”

The data for the $|2, 2\rangle \leftrightarrow |2, 1\rangle$ Rabi oscillations in ultracold ^{87}Rb atoms with three different detuning values are fitted to a sine function (shown in Fig. B.1). The oscillation frequencies versus detuning are plotted in Fig. B.2 with the calculated generalized Rabi frequency (Eq. 2.1.15). The qualitative trend of these data and the corresponding calculations clearly show that there is no Rabi “freeze” for ultracold ^{87}Rb atoms.

Appendix C

Manufacturing the rubidium vapor cells

The commercial availability of custom vapor cells is very limited, with a long supply time and uncertain quality. On the other hand, our research requires a variety of alkali vapor cells that can be produced promptly when they are needed. To bridge this gap, we developed and installed a vapor-cell filling station.

Our vapor cell filling system (see Fig. C.1) consists of a vacuum pump (Varian Turbo V70LP); a rotatable metal-glass connector with a flexible bellow; two buffer gas inlets for mixing two gases; a pirani gauge (Varian Agilent ConvecTorra) or capsule dial gauge (Edwards CG16K) that measures pressures above 1×10^{-3} Torr and an ion gauge (Bayard-Alpert) that measures pressures in the range of 1×10^{-4} to 1×10^{-9} Torr. A custom glass manifold is built for each vapor-cell filling procedure. The glass manifold is made of a glass tube connected to a rubidium ampoule with a breakable seal. Two cells are attached to each manifold. For paraffin-coated cells, two copper needles with a drop of paraffin at the tip and an magnetic stainless steel end were inserted into the manifold via additional tubes that are attached to the manifold opposite the vapor cells (Fig. C.2). The needles can be dragged in and out of the cell by a magnet located outside the manifold. Below is an itemized description of the vapor cell production process.

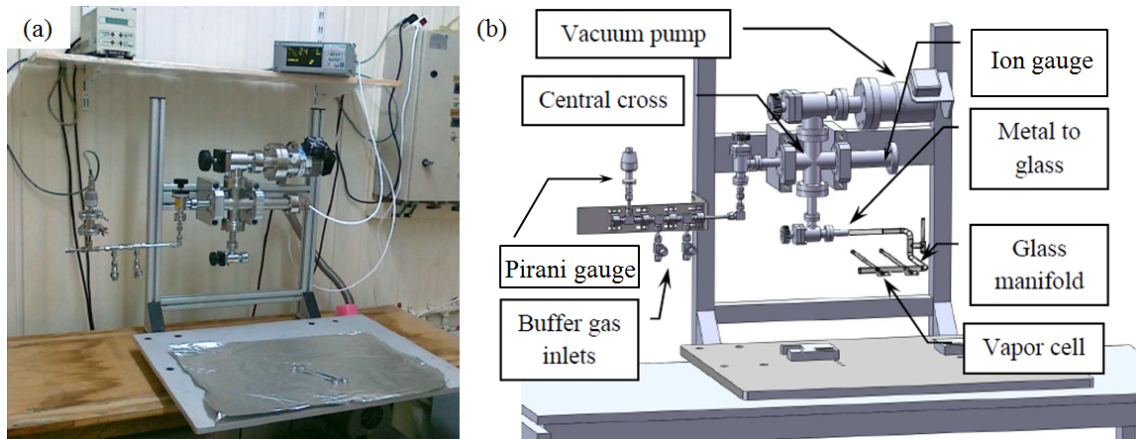


Figure C.1: Vapor-cell filling system. (a) the vapor cell filling system in its final stage of construction. (b) schematic. The central cross is connected to the vacuum pump (top), to the glass manifold that contains the cells (bottom), to the buffer gas inlets (left), to a Pirani vacuum gauge or a capsule gauge (left, for pressure of $760 - 10^{-3}$ Torr) and an ion gauge (right, for pressures of $10^{-4} - 10^{-11}$ Torr).

- Cell dimensions: the cells are cylindrical; the length is between 30 and 60 mm and the diameter is typically 25 mm. The vapor cell windows are 2.5 mm thick.
- Cell preparation: the first step is to attach a 1.5×8 mm side arm filling stem to a 25 mm diameter glass tube. Then windows are attached at both ends of the 25 mm tube to make the cell. This is done by mounting the 25 mm tube vertically on a motorized rotating stage and using a fine (around 0.8 mm diameter nozzle) flame torch.
- Glass manifold assembly: the cells are attached via the filling stem to a 12 mm diameter glass tube. A rubidium ampoule is also attached to the tube. For a paraffin-coated cell, an additional tube is attached opposite to the vapor cell's stem so paraffin loaded needles can be inserted into the cell.

- Leak detection: each manifold is tested by a helium leak detector.
- Cleaning process: The glass manifold is cleaned with 30% HCl followed by rinsing six times with distilled water.
- Preliminary paraffin coating: two copper needles with a magnetic end are used for evaporating paraffin on the inside wall of the cell (Fig. C.2). The needles' tips are loaded by dipping the tips in liquefied paraffin. After loading the needles with paraffin the needles are inserted into the back tubes and sealed inside the glass manifold.
- Attaching the glass manifold to the vacuum system: the glass manifold is attached to the vacuum system via the glass-to-metal connector [as shown in Fig. C.1 (b)] together with an internal stainless steel hammer. The cells are baked under vacuum to remove possible contamination (typically for 36 hours at 200°C).
- Paraffin coating: the paraffin coating is done by induction heating [54]. The copper needles are pushed towards the cells using a magnet located outside of the glass tube. A high-frequency AC magnetic field induced by coils located around the glass tube [see Fig. C.2 (a)] generates heat that evaporates the paraffin. The process is stopped after a visible amount of paraffin accumulates on the cell wall.
- Rubidium filling: the breakable seal is broken from the inside the glass manifold by the stainless steel hammer pushed towards the breakable seal using an external magnet. The rubidium is melted by a fan heater. A droplet of rubidium is gently poured into each cell.

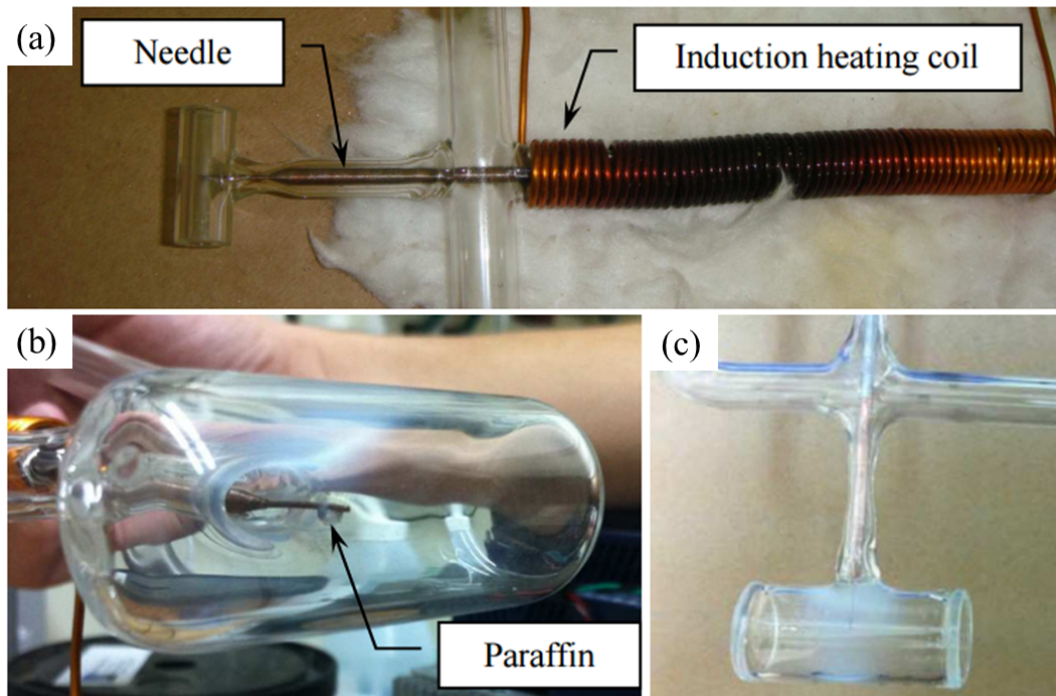


Figure C.2: Paraffin evaporation method. (a) the induction heating coil wrapped around the glass tube with the needle inside. The tip of the needle is inside the vapor cell. (This picture was taken during heating tests.) (b) drop of molten paraffin hanging from the tip of the needle inside the vapor cell, just before it evaporates. (c) vapor cell after paraffin evaporation (the coating is not uniform, but it does cover all the inner walls of the cell).

- Buffer gas filling: the gas tanks are connected to the vacuum system via needle valves (see Fig. C.1). Before filling, the ion gauge is turned off and the valve that leads to the vacuum pump is closed. The gas tank regulator is opened until the pressure reading on the Pirani (or the capsule) gauge reach the desired pressure of the buffer gas.
- Cell detaching: The cells are detached from the glass manifold by using a torch to melt the glass cells' stems carefully so rubidium will not burst into the cell. Rubidium that bursts into the cell might accumulate on the windows; for paraffin-coated cells, it would destroy the paraffin coating.
- Cell curing: heating the cells for few days at around 50°C will improve the cells' performance [higher signal-to-noise ratio (SNR) of the spectroscopy].

Appendix D

The Rabi oscillations fit parameters

In Sec. 5.1 we described the method we use to fit a function of the form of Eq. 5.1.1, (rewritten below) to the measured data of the Rabi oscillations. In this appendix we detail as an example all the fit parameters for one of the experiments, namely, Rabi “on-the-fly” with a 75 Torr neon buffer gas vapor cell.

$$f(t) = y_0 + ae^{-bt} + ce^{-dt}\sin(\tilde{\Omega}t + \phi). \quad [\text{D.0.1}]$$

Detuning [kHz]	y_0	a	b [sec ⁻¹]	c
-25	0.43 $\pm \times 10^{-5}$	5.7×10^{-3} $\pm 3.65 \times 10^{-5}$	1.71×10^3 ± 34	4.21×10^{-3} $\pm 10^{-5}$
-20	0.43 $\pm 5 \times 10^{-5}$	6.6×10^{-3} $\pm 2.5 \times 10^{-5}$	2.3×10^3 ± 37	6.4×10^{-3} $\pm 6.6 \times 10^{-5}$
-15	0.42 $\pm 3 \times 10^{-4}$	1.1×10^{-2} $\pm 2.8 \times 10^{-4}$	1.2×10^3 ± 59	1.1×10^{-2} $\pm 1.4 \times 10^{-4}$
-10	0.42 $\pm 3.5 \times 10^{-4}$	1.1×10^{-2} $\pm 2.9 \times 10^{-4}$	1.3×10^3 ± 71	1.5×10^{-2} $\pm 1.8 \times 10^{-4}$
-5	0.42 $\pm 3.0 \times 10^{-4}$	1.2×10^{-2} $\pm 2.3 \times 10^{-4}$	1.6×10^3 ± 91	1.7×10^{-2} $\pm 3.3 \times 10^{-4}$
0	0.42 $\pm 3.0 \times 10^{-4}$	1.1×10^{-2} $\pm 2.4 \times 10^{-4}$	1.3×10^3 ± 62	1.4×10^{-2} $\pm 1.4 \times 10^{-4}$
5	0.42 $\pm 4.0 \times 10^{-4}$	1.2×10^{-2} $\pm 3.5 \times 10^{-4}$	1.0×10^3 ± 54	1.3×10^{-2} $\pm 1.2 \times 10^{-4}$
10	0.42 $\pm 2.5 \times 10^{-4}$	9.3×10^{-3} $\pm 2.0 \times 10^{-4}$	1.3×10^3 ± 62	1.1×10^{-2} $\pm 1.2 \times 10^{-4}$
15	0.43 $\pm 5.0 \times 10^{-5}$	6.2×10^{-3} $\pm 2.7 \times 10^{-5}$	2.1×10^3 ± 39	7.0×10^{-3} $\pm 7.7 \times 10^{-5}$
20	0.43 $\pm 1.0 \times 10^{-4}$	6.9×10^{-3} $\pm 1.1 \times 10^{-4}$	1.2×10^3 ± 40	4.1×10^{-3} $\pm 7.4 \times 10^{-5}$
25	0.44 $\pm 1.0 \times 10^{-4}$	4.7×10^{-3} $\pm 5.3 \times 10^{-5}$	1.5×10^3 ± 41	1.9×10^{-3} $\pm 7.1 \times 10^{-5}$

Table D.1: Fit parameters (y_0 , a , b , and c) for Rabi “on-the-fly” in a 75 Torr Ne vapor cell. The measured resonance frequency is 18.37 MHz. For the rest of the parameters see Tab. D.2.

Detuning [kHz]	d [sec ⁻¹]	$2\pi \times \tilde{\Omega}$ [kHz]	ϕ [kHz]	R ²
-25	6.58×10^3 ± 78	6.05×10^4 ± 90	-7.3 $\pm 4.5 \times 10^{-2}$	0.9961
-20	6.0×10^3 ± 55	6.1×10^4 ± 60	-7.5 $\pm 1.2 \times 10^{-2}$	0.9962
-15	5.6×10^3 ± 64	6.0×10^4 ± 65	-7.4 $\pm 1.5 \times 10^{-2}$	0.9916
-10	5.6×10^3 ± 61	6.0×10^4 ± 65	-7.4 $\pm 1.4 \times 10^{-2}$	0.9907
-5	5.9×10^3 ± 93	6.1×10^4 ± 85	-8.8 $\pm 1.6 \times 10^{-2}$	0.9818
0	5.4×10^3 ± 50	6.0×10^4 ± 50	-7.5 $\pm 1.2 \times 10^{-2}$	0.9931
5	5.2×10^3 ± 45	6.0×10^4 ± 50	-7.5 $\pm 1.1 \times 10^{-2}$	0.9942
10	5.4×10^3 ± 56	6.0×10^4 ± 60	-7.5 $\pm 1.3 \times 10^{-2}$	0.9922
15	6.6×10^3 $\pm 1.0 \times 10^2$	6.0×10^4 $\pm 1.1 \times 10^2$	-7.2 $\pm 2.2 \times 10^{-2}$	0.9942
20	6.6×10^3 $\pm 1.0 \times 10^2$	6.0×10^4 $\pm 1.1 \times 10^2$	-7.2 $\pm 2.2 \times 10^{-2}$	0.9942
25	7.7×10^3 $\pm 2.3 \times 10^2$	6.1×10^4 $\pm 2.6 \times 10^2$	-7.3 $\pm 4.6 \times 10^{-2}$	0.9935

Table D.2: Continued from Tab. D.1: fit parameters (d , $\tilde{\Omega}$, ϕ , and R²) for Rabi “on-the-fly” in a 75 Torr Ne vapor cell. The measured resonance frequency is 18.37 MHz.

References

- [1] A. Kastler, “Optical methods for studying hertzian resonances,” *Science*, vol. 158, no. 3798, pp. 214–221, 1967.
- [2] W. Franzen, “Spin relaxation of optically aligned rubidium vapor,” *Phys. Rev.*, vol. 115, no. 4, p. 850, 1959.
- [3] M. Bouchiat and J. Brossel, “Relaxation of optically pumped rb atoms on paraffin-coated walls,” *Phys. Rev.*, vol. 147, no. 1, p. 41, 1966.
- [4] H. G. Dehmelt, “Slow spin relaxation of optically polarized sodium atoms,” *Phys. Rev.*, vol. 105, pp. 1487–1489, Mar 1957.
- [5] W. E. Bell and A. L. Bloom, “Optical detection of magnetic resonance in alkali metal vapor,” *Phys. Rev.*, vol. 107, no. 6, p. 1559, 1957.
- [6] M. Arditi and T. Carver, “The principles of the double resonance method applied to gas cell frequency standards,” *Proc. IEEE.*, vol. 51, pp. 190–202, Jan 1963.
- [7] M. Arditi and T. Carver, “Atomic clock using microwave pulse-coherent techniques,” *IEEE. T. Instrum. Meas.*, vol. IM-13, pp. 146–152, June 1964.
- [8] R. N. Hall, G. E. Fenner, J. D. Kingsley, T. J. Soltys, and R. O. Carlson, “Coherent light emission from gas junctions,” *Phys. Rev. Lett.*, vol. 9, pp. 366–368, Nov 1962.
- [9] M. T. Graf, D. F. Kimball, S. M. Rochester, K. Kerner, C. Wong, D. Budker, E. B. Alexandrov, M. V. Balabas, and V. V. Yashchuk, “Relaxation of atomic polarization in paraffin-coated cesium vapor cells,” *Phys. Rev. A*, vol. 72, p. 023401, Aug 2005.
- [10] M. V. Balabas, T. Karaulanov, M. P. Ledbetter, and D. Budker, “Polarized alkali-metal vapor with minute-long transverse spin-relaxation time,” *Phys. Rev. Lett.*, vol. 105, p. 070801, Aug 2010.
- [11] B. Julsgaard, A. Kozhekin, and E. S. Polzik, “Experimental long-lived entanglement of two macroscopic objects,” *Nature*, vol. 413, no. 6854, pp. 400–403, 2001.
- [12] D. Budker and M. Romalis, “Optical magnetometry,” *Nat. Phys.*, vol. 3, no. 4, pp. 227–234, 2007.
- [13] I. Kominis, T. Kornack, J. Allred, and M. Romalis, “A subfemtotesla multi-channel atomic magnetometer,” *Nature*, vol. 422, no. 6932, pp. 596–599, 2003.
- [14] G. Walker, A. S. Arnold, and S. Franke-Arnold, “Trans-spectral orbital angular momentum transfer via four-wave mixing in rb vapor,” *Phys. Rev. Lett.*, vol. 108, p. 243601, Jun 2012.
- [15] M. Shuker, O. Firstenberg, R. Pugatch, A. Ron, and N. Davidson, “Storing images in warm atomic vapor,” *Phys. Rev. Lett.*, vol. 100, p. 223601, Jun 2008.
- [16] D. Phillips, A. Fleischhauer, A. Mair, R. Walsworth, and M. D. Lukin, “Storage of light in atomic vapor,” *Phys. Rev. Lett.*, vol. 86, no. 5, p. 783, 2001.

- [17] C. Carr, R. Ritter, C. G. Wade, C. S. Adams, and K. J. Weatherill, “Nonequilibrium phase transition in a dilute rydberg ensemble,” *Phys. Rev. Lett.*, vol. 111, p. 113901, Sep 2013.
- [18] R. Jiménez-Martínez, W. C. Griffith, Y.-J. Wang, S. Knappe, J. Kitching, K. Smith, and M. D. Prouty, “Sensitivity comparison of mx and frequency-modulated bell–bloom cs magnetometers in a microfabricated cell,” *IEEE. T. Instrum. Meas.*, vol. 59, no. 2, pp. 372–378, 2010.
- [19] S. Knappe, V. Shah, P. D. Schwindt, L. Hollberg, J. Kitching, L.-A. Liew, and J. Moreland, “A microfabricated atomic clock,” *Appl. Phys. Lett.*, vol. 85, no. 9, pp. 1460–1462, 2004.
- [20] I. I. Rabi, “Space quantization in a gyrating magnetic field,” *Phys. Rev.*, vol. 51, no. 8, p. 652, 1937.
- [21] D. Vion, A. Aassime, A. Cottet, P. Joyez, H. Pothier, C. Urbina, D. Esteve, and M. H. Devoret, “Manipulating the quantum state of an electrical circuit,” *Science*, vol. 296, no. 5569, pp. 886–889, 2002.
- [22] J. M. Martinis, S. Nam, J. Aumentado, and C. Urbina, “Rabi oscillations in a large josephson-junction qubit,” *Phys. Rev. Lett.*, vol. 89, p. 117901, Aug 2002.
- [23] H. Kamada, H. Gotoh, J. Temmyo, T. Takagahara, and H. Ando, “Exciton rabi oscillation in a single quantum dot,” *Phys. Rev. Lett.*, vol. 87, p. 246401, Nov 2001.
- [24] A. Schülzgen, R. Binder, M. E. Donovan, M. Lindberg, K. Wundke, H. M. Gibbs, G. Khitrova, and N. Peyghambarian, “Direct observation of excitonic rabi oscillations in semiconductors,” *Phys. Rev. Lett.*, vol. 82, pp. 2346–2349, Mar 1999.
- [25] F. Jelezko, T. Gaebel, I. Popa, A. Gruber, and J. Wrachtrup, “Observation of coherent oscillations in a single electron spin,” *Phys. Rev. Lett.*, vol. 92, p. 076401, Feb 2004.
- [26] A. Daniel, R. Agou, O. Amit, D. Groswasser, Y. Japha, and R. Folman, “Damping of local rabi oscillations in the presence of thermal motion,” *Phys. Rev. A.*, vol. 87, no. 6, p. 063402, 2013.
- [27] M. Givon, Y. Margalit, A. Waxman, T. David, D. Groswasser, Y. Japha, and R. Folman, “Magic frequencies in atom-light interaction for precision probing of the density matrix,” *Phys. Rev. Lett.*, vol. 111, p. 053004, Aug 2013.
- [28] M. O. Scully and M. S. Zubairy, *Quantum optics*. Cambridge university press, 1997.
- [29] J. J. Saqrui, *Modern Quantum Mechanics*, ch. 3, pp. 180–185. Addison Wesley, 1994.
- [30] D. Cohen, *Lecture Notes in Quantum Mechanics*. 2006. arXiv quant-ph/0605180.
- [31] D. A. Steck, *Rubidium 87 D Line Data*. 2001. <http://steck.us/alkalidata>.
- [32] F. Bloch, “Nuclear induction,” *Phys. Rev.*, vol. 70, no. 7-8, p. 460, 1946.

- [33] R. P. Feynman, F. L. Vernon Jr, and R. W. Hellwarth, “Geometrical representation of the schrödinger equation for solving maser problems,” *J. Appl. Phys.*, vol. 28, no. 1, pp. 49–52, 1957.
- [34] H. Gibbs, “Importance of nuclear-spin effects in extracting alkali spin-exchange cross sections from zeeman optical-pumping signals,” *Phys. Rev.*, vol. 139, pp. A1374–A1391, Aug 1965.
- [35] M. V. Balabas, K. Jensen, W. Wasilewski, H. Krauter, L. S. Madsen, J. H. Müller, T. Fernholz, and E. S. Polzik, “High quality anti-relaxation coating material for alkali atom vapor cells,” *Opt. Express.*, vol. 18, pp. 5825–5830, Mar 2010.
- [36] I. Novikova, A. B. Matsko, and G. R. Welch, “Influence of a buffer gas on nonlinear magneto-optical polarization rotation,” *J. Opt. Soc. Am. B.*, vol. 22, pp. 44–56, Jan 2005.
- [37] S. Seltzer and M. Romalis, “High-temperature alkali vapor cells with antirelaxation surface coatings,” *J. Appl. Phys.*, vol. 106, no. 11, p. 114905, 2009.
- [38] W. Happer, “Optical pumping,” *Rev. Mod. Phys.*, vol. 44, pp. 169–249, Apr 1972.
- [39] N. Bhaskar, “Potential for improving the rubidium frequency standard with a novel optical pumping scheme using diode lasers,” *IEEE. T. Ultrason. Ferr.*, vol. 42, pp. 15–20, Jan 1995.
- [40] M. Givon, *A Magic Frequency in Light-Matter Interaction of a Two-State System with Multiple Degeneracy*. PhD thesis, Ben-Gurion University of the Negev, Be'er-Sheva 84105, Israel, 2014. http://www.bgu.ac.il/atomchip/Theses/Menachem_Givon%20_PhD_2015.pdf.
- [41] A. Waxman, “Coherent manipulations of the rubidium atom ground state,” Master’s thesis, Department of Physics, Ben-Gurion University of the Negev, Be'er-Sheva 84105, Israel, 2007. http://www.bgu.ac.il/atomchip/Theses/Amir_Waxman_MSc_2007.pdf.
- [42] J. T. Verdeyen, *Laser Electronics.*, ch. 6, pp. 144–148. Prentice-Hall, Inc., Englewood Cliffs, New Jersey, 1995.
- [43] L. Ricci, M. Weidemller, T. Esslinger, A. Hemmerich, C. Zimmermann, V. Vuletic, W. Knig, and T. Hnsch, “A compact grating-stabilized diode laser system for atomic physics,” *Opt. Commun.*, vol. 117, no. 56, pp. 541 – 549, 1995.
- [44] A. Daniel, “Coherence time of rabi oscillations of cold atoms,” Master’s thesis, Department of Physics, Ben-Gurion University of the Negev, Be'er-Sheva 84105, Israel, 2012. http://www.bgu.ac.il/atomchip/Theses/Anat_Daniel_MSc_2012.pdf.
- [45] Y. Yoshikawa, T. Umeki, T. Mukae, Y. Torii, and T. Kuga, “Frequency stabilization of a laser diode with use of light-induced birefringence in an atomic vapor,” *Appl. Optics.*, vol. 42, no. 33, pp. 6645–6649, 2003.
- [46] E. A. Donley, T. P. Heavner, F. Levi, M. O. Tataw, and S. R. Jefferts, “Double-pass acousto-optic modulator system,” *Rev. Sci. Instrum.*, vol. 76, no. 6, 2005.

- [47] J. Eddie H. Young and S.-K. Yao, “Design considerations for acousto-optic devices,” *Proc. IEEE.*, vol. 69, pp. 54–64, Jan 1981.
- [48] Y. Margalit, “Measuring hyperfine population of hot alkali vapor using a magic frequency,” Master’s thesis, Department of Physics, Ben-Gurion University of the Negev, Be’er-Sheva 84105, Israel, 2014. http://www.bgu.ac.il/atomchip/Theses/Yair_Margalit_MSc_2014.pdf.
- [49] E. Jones, T. Oliphant, P. Peterson, *et al.*, “SciPy: Open source scientific tools for Python,” 2001–. [Online; accessed 2016-01-05].
- [50] M. Erhard and H. Helm, “Buffer-gas effects on dark resonances: Theory and experiment,” *Phys. Rev. A*, vol. 63, p. 043813, Mar 2001.
- [51] G. Aviv, “Two-photon coherent manipulation of an atomic two-state system,” Master’s thesis, Department of Physics, Ben-Gurion University of the Negev, Be’er-Sheva 84105, Israel, 2009. http://www.bgu.ac.il/atomchip/Theses/Gal_Aviv_MSc_2009.pdf.
- [52] S. Machluf, Y. Yapha, and R. Folman, “Coherent sterngerlach momentum splitting on an atom chip,” *Nat. Commun.*, vol. 4, no. 2424, 2013.
- [53] R. Folman, P. Krger, J. Schmiedmayer, J. Denschlag, and C. Henkel, “Microscopic atom optics: From wires to an atom chip,” vol. 48 of *Adv. Atom. Mol. Opt. Phy.*, pp. 263 – 356, Academic Press, 2002.
- [54] D. Phillips, A. Boca, and R. Walsworth, “Evaporative coating of rb maser cells,” *notes*, 1999.